Metal-Oxide Nanomaterials Synthesis and Applications in Flexible and Wearable Sensors

Yeosang Yoon,[†] Phuoc Loc Truong,[†] Daeho Lee,* and Seung Hwan Ko*

Cite This: *ACS Nanosci. Au* 2022, 2, 64−92

Read Online

ACCESS | Metrics & More | Article Recommendations

ABSTRACT: Metal-oxide nanomaterials (MONs) have gained considerable interest in the construction of flexible/wearable sensors due to their tunable band gap, low cost, large specific area, and ease of manufacturing. Furthermore, MONs are in high demand for applications, such as gas leakage alarms, environmental protection, health tracking, and smart devices integrated with another system. In this Review, we introduce a comprehensive investigation of factors to boost the sensitivity of MON-based sensors in environmental indicators and health monitoring. Finally, the challenges and perspectives of MON-based flexible/wearable sensors are considered.
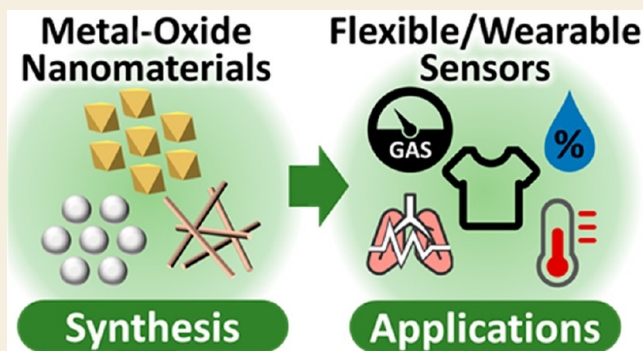
1. INTRODUCTION

Recently, flexible electronics including flexible sensors,[1−4] power sources,[5] and conductors[6,7] have been studied eagerly due to significant advantages in terms of reduced weight, flexibility, and durability to sustain multideformation (i.e., stretching, twisting, bending, and compression) compared with their rigid counterparts.[8−10] During this vigorous development, flexible/wearable sensory systems have also been studied with various sensing materials including carbon materials,[2,11−13] biomolecules,[14,15] conductive polymers,[2,16,17] and inorganic nanomaterials[1,18,19] to improve their sensitivity, functionality, and stability via diverse strategies.

Among these materials, metal-oxide nanomaterials (MONs) are promising candidates in diverse areas of chemistry, materials science, physics, and biotechnology.[20] The unique electronic structure determines the conductor, semiconductor, and insulator properties of nanomaterials. Transition metal ions typically possess unfilled d-shells, allowing for reactive electronic transitions, wide band gaps, superior electrical characteristics, and high dielectric constants.[21] As a result, MONs have exceptional and adjustable optoelectronic, optical, electrical, thermal, magnetic, catalytic, mechanical, and photochemical properties. Furthermore, MONs have a wide range of applications: sensors, fuel cells, batteries, actuators, supercapacitors, optical devices, pyroelectrics, piezoelectrics, ferroelectrics, and random access memory due to their exceptional shape and size, which manifest distinctive physicochemical properties. Potential applications also exist due to the high density of surface sites and nanostructures.[22]

Especially, for sensing materials, MONs, mainly copper(II) oxide (CuO), copper(I) oxide (Cu_2O), tin(II) oxide (SnO), tin(IV) oxide (SnO_2), zinc oxide (ZnO), nickel oxide (NiO), indium oxide (In_2O_3), and tungsten oxide (WO_3), are promising candidates that manifest high sensitivity, fast response/recovery (res/rec) time, excellent reproducibility and stability, and cost-effectiveness with simple fabrication processes.[23−29] Conventional MON-based sensors are generally fabricated on rigid substrates due to their high manufacturing temperature, which increases energy consumption and manufacturing cost as well as imposes limitations in expanding applications.[30−32] However, numerous studies on building MON-based sensors on flexible and stretchable substrates have been reported as a result of rapid advances in fabrication techniques in the past decade. As substrates for MON-based flexible sensors, polyimide (PI), polyethylene naphthalene (PEN), poly(ether sulfone) (PES), polyether ether ketone (PEEK), polycarbonate, polydimethylsiloxane (PDMS), and polyethylene terephthalate (PET) are preferred.
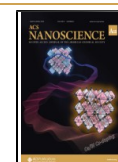
The thermal and chemical resistance, flexibility, and transparency of materials should be addressed for pragmatic sensing applications.[33] Conductive features are essential to the operation of electrical devices, enabling the connection between various components.[34]

We present an overview of MON-based flexible/wearable sensors in this Review. First, we go through some of the most prevalent sensing materials. Then we discuss the diverse manufacturing technologies for fabricating flexible/wearable sensors. The applications of flexible/wearable sensors in the field of environmental indicators (e.g., gas, chemical, pH, and humidity sensors) and health monitoring (e.g., biomaterial, respiration, temperature, and mechanical sensors) are introduced to gain a comprehensive understanding of sensing efficiency via the design strategies and advanced characterization techniques. Finally, we discuss the challenges that flexible/wearable sensors are currently facing as well as their potential development in the coming years.

2. MONs AS SENSING MATERIALS

Various MONs in Figure 1 have been intensively employed in diverse applications, such as gas and chemical sensors,[35−43]
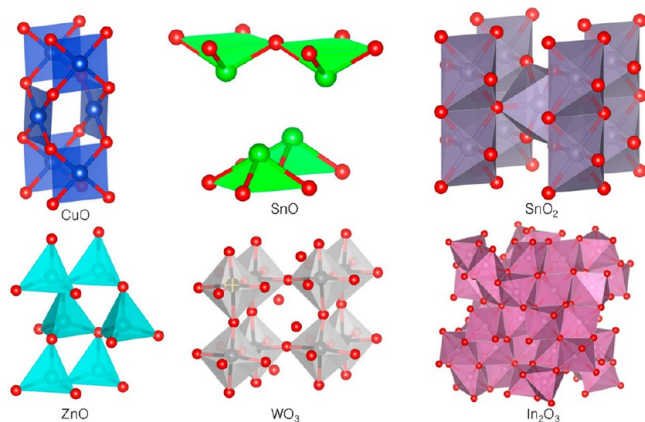

Figure 1. Crystal structures of MONs.

ultraviolet (UV) sensors,[44−50] biosensors,[51−57] humidity sensors,[58−65] multifunction sensors,[66] solar cells,[67−70] batteries,[71−73] photocatalysts,[74−76] and thin-film transistors.[77−80]

Copper oxides exist in two different states. CuO, also called cupric oxide with a narrow band gap energy of 1.2 eV, is a p-type semiconductor that is chemically stable, cost effective, and black in color.[81] Cu_2O, also called cuprous oxide, is another type of copper oxide with a reddish color and band gap energy of 2−2.17 eV.[82] Additionally, CuO with a $C2/c$ space group (a = 4.683 Å, b = 3.421 Å, and c = 5.129 Å) is attributed to a monoclinic crystal structure where each Cu species is bound to four oxygen atoms in a rectangular parallelogram.[83] CuO is dominant for gas sensors, while Cu_2O has received less attention in gas sensing applications than CuO.[84,85] The key quality of p-type MONs, which are less conductive at elevated temperatures versus n-type MONs, is that they tend to replace lattice oxygen in the air. It is beneficial to maintain the metal-oxide stoichiometry for sensor sustainability. For instance, the shelf life of the carbon monoxide (CO) gas sensor is likely to be maintained and has extended long-term stability. However, the mobility of charge carriers is the most significant disadvantage and can impact the sensitivity, response, and recovery time. These drawbacks are likely to be mitigated by

modifying the film morphology, electrode design, and doping materials.[35,36,86,87]

Thermal oxidation is a popular method for producing CuO-based sensors due to its superior quality, simplicity, and low cost, but it is time-consuming. Other strategies for fabricating CuO-based gas sensors have been reported to overcome this limitation, including hydrothermal,[28] solvothermal,[35] and thermal evaporation.[36,86,87] Diverse nanostructures, including nanoparticles (NPs),[35] nanowires (NWs),[87] nanoplatelets,[36] nanocubes (NCs), nanorods (NRs), nanoflowers (NFs), and nanotubes (NTs),[86] have been exploited for CuO-based sensors that typically detect various reducing and oxidizing gases.

The bulk and surface-sensitive materials of the MON-based sensor can be distinguished. SnO_2 is classified as a surface-sensitive material, despite the presence of bulk defects that affect conductivity. Variation in the electrical conductivity of sensors is caused by a dispersing conduction band and charge carrier concentration due to high charge mobility. Moreover, stannous oxide, a p-type SnO semiconductor with a $P4/nmm$ space group symmetry ($a = b = 3.8029$ Å, $c = 4.8382$ Å), is attributed to a tetragonal structure that has a direct band gap of 2.5−3.0 eV.[88] An n-type SnO_2, also called stannic oxide or cassiterite with $P4_2/mnm$ space group symmetry ($a = b = 3.8029$ Å), is ascribed to a rutile structure with a wide band gap energy (3.6 eV).[89] Since SnO is more unstable above 270 °C, SnO gas sensors are typically made of thick porous SnO_2 films with a large specific surface area. The electrons trapped by adsorbed species and band bending generate changes in conductivity when the material is heated. Due to high selectivity, fast response, low price, chemical stability, and large excitation binding energy, diverse SnO_2 nanostructures have been developed for gas sensing and health monitoring via hydrothermal,[90−93] inkjet printing,[94] electrospinning,[95,96] pulsed laser deposition,[97] electrodeposition,[98] and hot press.[99]

ZnO is an n-type semiconductor that possesses qualities such as cost-effectiveness, chemical stability, reproducibility, and nontoxic property. ZnO with a $P6_3mc$ space group ($a = 3.25$ Å and $c = 5.12$ Å) is attributed to a hexagonal wurtzite structure[100] for which each Zn is tetrahedrally bound to four O species that possess intrinsic defects like Zn interstitials and oxygen vacancies[101] with a large band gap and high excitation binding energy. Due to the sizable electronegative difference (O = 3.44 and Zn = 1.65), Zn and O have strong ionic bonds. Polar surfaces possess distinct physicochemical properties versus nonpolar surfaces based on the rearrangement of negatively or positively charged surfaces.[100] The O-polar surface exhibits a relatively electronic structure, while Zn-polar surfaces are more dynamic than nonpolar and O-polar surfaces due to the creation of energetic OH^- ions.[102] These properties are essential in the growth of ZnO nanomaterials, including crystallization, defects, and polarization. ZnO is also employed in diverse applications, including sensors, photocatalysis, solar cells, and three-dimensional (3D) surface-enhanced Raman spectroscopy platform applications. ZnO, which can detect UV light[9,45,97,100−106] and various gases, such as H_2,[24,107−109] H_2S,[25,110] O_2,[24] exhaled breath,[111] and volatile organic compounds (VOCs),[105] has been synthesized by various strategies, including thermal oxidation,[24,106] wet-chemical processes,[25,111] laser-assisted flow deposition,[45] nonhydrolytic aminolysis,[102] hydrothermal methods,[103,104,107,110] sol−gel methods,[105] electrospinning,[108] solvent casting,[109] and pulsed laser deposition.[112]

In_2O_3 is an n-type semiconductor with two types of crystalline structures: cubic (bixbyite) and rhombohedral (corundum). Furthermore, the band gap energy in both phases is 3 eV. In_2O_3 with an $Ia3$ nonsymmetric space group ($a = 1.011$ nm) is attributed to a cubic structure, while the $R3c$ space group ($a = 5.487$ Å, $b = 5.487$ Å, and $c = 5.781$ Å) is designated as a rhombohedral structure. Nonsymmetric cubic In_2O_3, with high conductivity, is commonly utilized in microelectronics.[113] Phase compositions, preparation conditions, and the indium electronic state of materials all influence the features of In_2O_3-based gas sensors. Several synthesis methods for developing gas, chemical, and healthcare sensors from In_2O_3 nanostructures have been exploited, including electrospinning,[114,115] sputtering,[116,117] sol−gel,[37] hydrothermal,[118] facile solution-based processing,[26] and thermal annealing.[37]

Tungsten oxide (WO_3) is an n-type semiconductor with a broad band gap energy (2.6−3.25 eV). WO_3 has diverse crystal structures, including monoclinic, hexagonal, cubic, and orthorhombic phases. WO_3 with a $P2_1/c$ space group ($a = 7.30$ Å, $b = 7.53$ Å, and $c = 7.69$ Å) is designated as a monoclinic structure commonly explored for gas sensing. This is further composed of a WO_6 octahedral bound to corner-sharing of oxygen atoms.[119]

Sputtering, hydrothermal, sol−gel, wet-chemical, thermal oxidation, and electrospinning methods are utilized to fabricate WO_3 nanostructures with variable phases, sizes, porosity, and thickness.[27,120−124] The preparation process and postannealing treatment have a significant impact on the performance characteristics of WO_3-based sensors.[125,126]

3. CRUCIAL PARAMETERS FOR SENSORS

Parameters such as sensitivity, selectivity, res/rec time, and limit of detection (LOD) are pivotal to assess the sensing efficiency of sensors. Sensor parameters can be optimized by various technological approaches.

3.1. Sensitivity

The signal due to detector and target analyte interaction is recognized during detection time. Sensitivity can be defined depending on sensor types as follows.

Chemo-resistive sensors:[93]

$$S = \frac{R_g}{R_a} \quad \text{for oxidizing gases}$$

$$S = \frac{R_a}{R_g} \quad \text{for reducing gases}$$

Or[127,128]

$$S\% = \frac{(R_g - R_a)}{R_g} \times 100\%$$

$$S\% \frac{(R_a - R_g)}{R_a} \times 100\%$$

where R_g and R_a are resistance changes in gas and air, respectively.

Electric-resistive sensors:[96]

$$S = \frac{I_g}{I_a}$$

where I_g and I_a are the sensor current in gas and air, respectively.

Capacitive-type sensor:[129]

$$S\% = \frac{(C_{fin} - R_{ini})}{C_{ini} \times (T_{fin} - T_{ini})} \times 100\%$$

where C_{ini} and C_{fin} are the capacitance at the initial (T_{ini}) and the final (T_{fin}) temperatures, respectively.

The enhancement of sensitivity is described in detail throughout sections 2 and 3. Morphologies and microstructures play a pivotal role in enhancing sensitivity. MONs can be functionalized by doping and hybridization strategies. The presence of metallic dopants may reduce the activation energy of gas analytes by lowering operation temperature.[130] Doping and hybridization with covalent and noncovalent interactions also enable tuning of morphologies, crystallites, and size, generating very active surface sites and significantly boosting the sensing efficiency.[96,99,127,128,131] Additionally, the sensitivity can be considerably enhanced by the working conditions (light irradiation,[128,132] analyte type[127] and concentration,[109,131] humidity,[94,131] and temperature[109,132]) and fabrication (synthesis,[133] substrate,[109] dopant loading,[128,131,132] and thickness[134]).

3.2. Selectivity

The selectivity of sensors can be understood as the capability of sensors to detect a target analyte in the mixture of analytes. Achieving a high selectivity is still a big challenge for MON-based sensors. The capability of detecting a single analyte distinctively among various analytes is commonly accomplished through temperature modulation[1] or sensor arrays.[20,135] Also, functionalized MONs with dopants and hybrid access a robust enhancement of sensor selectivity.

3.3. Stability

Stability is a vital key in the enlargement of sensors in the market and can be considered in two aspects. First, the active stability terms include the reproducibility of sensor features at least two years in the operating conditions. The second aspect of stability is the capacity to maintain sensitivity and selectivity. Korotcenkov and Cho specified that chemical mechanical impacts and environment such as humidity and temperature oscillation at an ambient atmosphere, and interference effect may contribute to instability.[136] Almost no unified strategy improves the stability of MONs. Post treatments, such as annealing, calcination methods, and reduced operating temperature of sensitive materials, enhance the stability. The stability can also be improved by metal doping and MON hybridization.[20]

Improved engineering approaches, including drift compensation, selecting a correct analyte in the sensing system, adding filters, and temperature stabilization, also help solve stability issues.[136]

3.4. Functional Characterization Techniques

Diverse characterization methodologies have been exceptionally utilized to generate high-resolution photographs of materials' nanostructure, along with the directly sensing process. For instance, X-ray diffraction (XRD) analysis is a valuable technique for examining the link between the crystal phase-sensing potential. Researchers can tune synthesis procedures on the surface of MONs using high-resolution transmission electron microscopy (HRTEM) and scanning tunneling microscopy (STM). In addition, analytical instru-
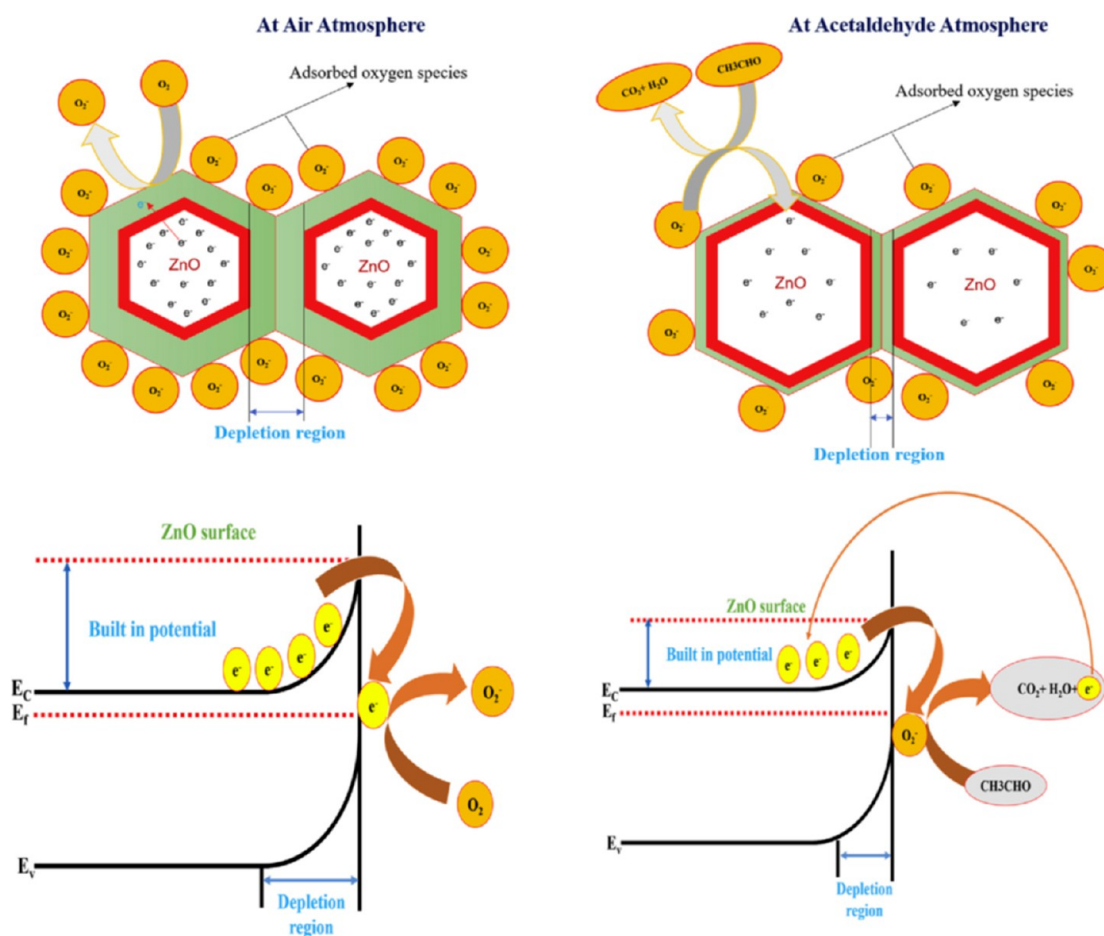
Figure 2. Schematic of the sensing mechanism of ZnO NRs toward CH_3CHO gas. Reprinted from ref 105, with permission from Elsevier.

ments, including a Fourier transform infrared (FTIR) spectrometer, photoluminescence (PL) spectrometer, and Raman spectrometer, deliver multiscale information in the sensing process, enabling a deeper insight into the mechanism and sensing process. Furthermore, time-resolved spectroscopies, such as time-resolved mid-IR and PL, two-photon photoemission, transient absorption spectroscopy, and positron annihilation lifetime spectroscopy are conducted to quantify the diffusion/transfer state of photoexcited carriers.[137−139]

The XRD pattern reveals the structure-sensing activity relations based on structural information such as shape, size, and crystallinity.[44] This technique is promising to figure out phase transformations, orientations, and the impact of hybridization or doping on morphology and crystallinity. A cutting-edge technique, In situ XRD researches crystallization behavior by manipulating exterior conditions, enables a direct remark of phase composition and crystallization progression.[140] Nanoscale structure, interface, and grain size are routinely detected with transmission electron microscopy (TEM). In various works, TEM study has been used to demonstrate the microstructural evolution and morphology modification of MONs during preparation methods such as hydrothermal treatment,[28] wet chemical synthesis,[141] single-step thermal decomposition,[142] and sputtering.[143] Electron energy-loss spectroscopy (EELS) can suggest that charges transfer from the MONs surface to chemisorbed O_2 elements due to the lack of the vacancy loss characteristic.[144,145] In order

to provide more complete results, EELS-equipped TEM is powerful and can reveal chemical configurations, lattice and crystal structure, oxidation state, and band gap.[146] Due to the unaltered surface of MONs in ultrahigh vacuum, in situ STM research may offer a deeper knowledge of surface processing on sensitive materials during adsorption and reaction processes. Integration with atomic force microscopy (AFM) or tip-enhanced Raman spectroscopy (TERS) technology clarifies sensing reaction mechanisms that offer the design and development of innovative materials for optoelectronic applications.[147,148] X-ray photoelectron spectroscopy (XPS) is influential in providing chemical states and compositions of elements. However, XPS does not exhibit the sensing process during a reaction between chemisorbed O_2 species and target analytes. Near ambient pressure XPS (NAP-XPS) is a perfect alternating to investigate sensing mechanisms in diverse surfaces under the appearance of vapors and gases. The intermediates of radical O_2 species, as well as the stoichiometry of MONs, also are recognized.[20]

4. MON-BASED FLEXIBLE/WEARABLE SENSORS

4.1. Gas Sensors

MON-based gas sensors usually detect gases through their resistance change caused by the interaction of exposed target gas and chemisorbed oxygen ions on the surface of the metal oxide. When the metal oxides are present in the ordinary atmosphere, oxygen molecules are absorbed on the surface and extract electrons consequently from the conduction band in
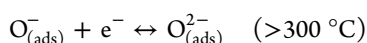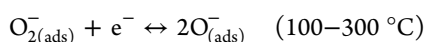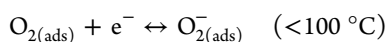
Table 1. Sensing Efficiency of Diverse Materials

materials	method	substrate	target	temperature (°C)	LOD	response	res/rec (s)	ref
Pd NPs/ZnO NRs	sputtering	PI	H_2 (1000 ppm)	RT	0.2 ppm	91^c	18.8/NA	134
Pd-SnO$_2$ NPs	inkjet printing	PI	CO (50 ppm), dry air	250	NA	2.1^a	NA	94
			CO (50 ppm), wet air			1.5^a		
			NO$_2$ (5 ppm), dry air			3.4^b		
			NO$_2$ (5 ppm), wet air			2.5^b		
SnO$_2$/SnS$_2$ NTs	in situ sulfuration	PET	NH$_3$ (100 ppm)	RT	NA	2.48^e	21/110	96
SnO$_2$ NTs	electrospinning				NA	1.25^e	NA	
PVDF/SnO$_2$ NPs/rGO	hot press	PVDF	H$_2$ (1000 ppm)	RT	500 ppb	71.4^c	52/242	99
ZnO NWs	hydrothermal growth	carbon microfiber	O$_2$ (600 ppm)		2 ppm	13^b	10/12	24
			H$_2$ (500 ppm)		4 ppm	11.2^a	8/12	
ZnO film	solution casting	chitosan/PVP (CHP)	H$_2$ (2%)	150	NA	46^c	NA	109
				180		69^c	NA	
			H$_2$ (0.5%)	150		24^c	1080/210	
		SiO$_2$	H$_2$ (0.5%)	150		10^c	NA	
			H$_2$ (2%)	150		24^c	NA	
Cr-ZnO NPs	hydrothermal growth	Glass	NH$_3$ (50 ppm), UV	RT	NA	9^c	270/300	128
Ce-ZnO NPs	hydrothermal growth	PET	NH$_3$ (0.1−1 ppm), 97.5% RH	RT	NA	32.66^c	155/NA	131
rGO/ZnO NRs	spin-cast	PDMS	NO$_2$ (3000 ppb)	RT	40 ppb	55.4^d	16/65	127
In$_2$O$_3$/rGO	DLW	PI	NO$_2$ (1 ppm)	RT	NA	31.6^d	252/798	133
Pt NPs/In$_2$O$_3$ film	spray-coating	PI	EtOH	RT	5.14 ppb	90 (S/N)	1/2	37
Ni-WO$_3$ NFs	hydrothermal growth	ceramic tube	CH$_3$COCH$_3$ (100 ppm), white light	RT	2 ppm	38^c	150/65	132
Au-CeO$_2$ NPs	hydrothermal growth	ceramic	H$_2$S (50 ppm)	100	94 ppb	976^c	66/166	130
Pd-CeO$_2$ NPs			SO$_2$F$_2$	250	1.0 ppb	153^c	63/773	
CeO$_2$ NPs/g-C$_3$N$_4$	screen-printing	PET	humidity	RT	6573	959.5 pF/% RH (0−97% RH)	12/NA	172
CeO$_2$ NPs	hydrothermal growth				NA	NA	33/NA	
PANI/CeO$_2$ NPs	in-situ self-assembly	PI	NH$_3$ (50 ppm)	RT	16 ppb	262.7^c	NA/840	198
PANI					NA	NA	65.8^c	NA/900	
La-AlO$_3$ film	sol−gel process	PI	temperature	30−200	NA	$2.7%°/C$	NA	129
Al$_2$O$_3$ film					NA	$1.9%/°C$	NA	
TiO$_2$ NPs/2D-TiC	thermal decomposition	PET	EtOH (10−60 ppm)	RT	10 ppb	380^f	2.0/NA	142
2D-TiC					NA	155^f	3.2/NA	
PANI/Rh-SnO$_2$ NTs	in situ polymerization	PET	NH$_3$ (100 ppm)	RT	500 ppb	13.6^b	NA	95

^{a}(R_a/R_g). ^{b}(R_g/R_a). ^{c}($[R_a − R_g]/R_a$%). ^{d}($[R_g − R_a]/R_g$%). ^{e}(I_g/I_a). ^{f}(KP^m).

the formation of the negatively charged ion. In this process, the metal oxide increases or decreases the conductivity depending on whether the metal oxide is n-type or p-type. In the case of n-type, the conductivity decreases because electron carriers are captured by oxygen. On the contrary, p-type metal oxides increase the conductivity as hole carriers are generated.

The ion form of oxygen includes O_2^-, O, and O^{2-}, of which the dominant form depends on operating temperature, because reduction processes of the oxygen ions occur in stages below 100 °C, between 100 and 300 °C, and above 300 °C as shown by the following equations.

$$O_{2(ads)} + e^- \leftrightarrow O_{2(ads)}^- \quad (<100\ °C)$$

$$O_{2(ads)}^- + e^- \leftrightarrow 2O_{(ads)}^- \quad (100−300\ °C)$$

$$O_{(ads)}^- + e^- \leftrightarrow O_{(ads)}^{2-} \quad (>300\ °C)$$

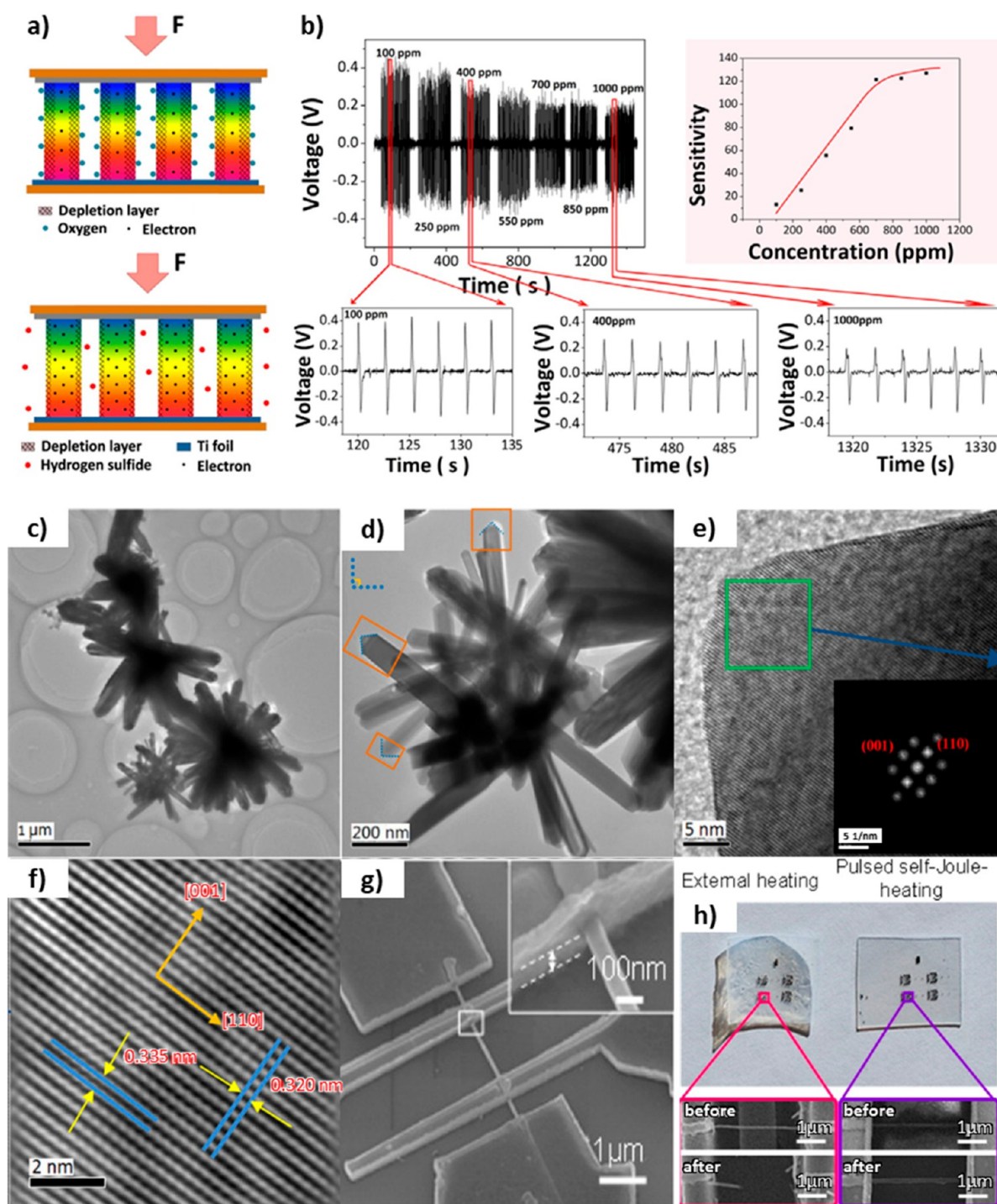Furthermore, the chemical reaction between chemisorbed oxygen ions and the target gas also affects the number of charge carriers of the metal oxides. Correspondingly, the changed conductivity of MON allows the detection of the target gases. In the case of the exposure of the reducing gas, including H$_2$S, NH$_3$, CO, H$_2$, acetaldehyde (CH$_3$CHO), and ethanol (EtOH), oxygen ions reacting with the reducing gas, as shown in following equations, reinject electrons to the conduction band. In other words, the surface of metal oxides is reduced by the reducing gas.

$$2H_2S_{(gas)} + O_{2(ads)}^- \leftrightarrow 2H_2O_{(gas)} + 2SO_{2(gas)} + 3e^-$$

$$4NH_{3(ads)} + 3O_{2(ads)}^- \rightarrow 2N_{2(gas)} + 6H_2O + 3e^-$$

$$2CO_{(gas)} + O_{2(ads)}^- \rightarrow 2CO_{2(gas)} + e^-$$

$$2H_{2(gas)} + O_{2(ads)}^- \rightarrow 2H_2O_{(gas)} + 2e^-$$
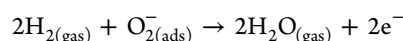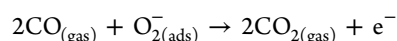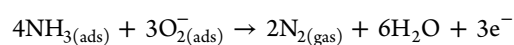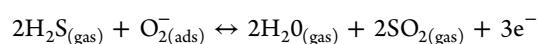
Figure 3. (a) Schematic of piezoelectric output and depletion layer at atmosphere and H_2S environment. (b) Output voltage data and sensitivity of a piezoelectric-based ZnO NR gas sensor depending on the diverse concentrations of H_2S gas. Copyright IOP Publishing Ltd. Reproduced from ref 25 with permission. (c) Lower and (d) higher magnification TEM photos of 3D hierarchical SnO_2. (e) HRTEM photo of a single SnO_2 nanorod. (f) Focused HRTEM photo taken from the rectangular region in (e). Adapted with permission from ref 93. Copyright 2015 Elsevier. (g) SEM photo and (h) photos of a SnO_2 NWs-based sensor under external heating (left) and self-Joule-heating (right) conditions. Reproduced from ref 97. Copyright 2016 American Chemical Society.

$$C_2H_5OH_{(ads)} + 3O^-_{2(ads)} \rightarrow 2CO_{2(gas)} + 3H_2O + 3e^-$$

$$2CH_3CHO_{(ads)} + 5O^-_{2(ads)} \rightarrow 4CO_{2(gas)} + 4H_2O + 5e^-$$
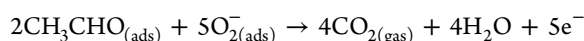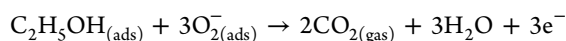
Consequently, the reinjection of electrons induces a change in the conductivity of the metal oxides by the decrease of hole carriers or the increase of electron carriers and permits precise sensing of target gases. Figure 2 shows a schematic of the sensing mechanism of ZnO NRs toward CH_3CHO gas for an instance.[105]

In contrast, when the metal oxides are exposed to an oxidizing gas such as NO_2, NO, and O_2, the adsorbed oxygen ions extract more electrons to react with the target gases and

the extraction changes the conductivity of the metal oxide sensor as shown in the following equations.[110]

$$NO_{2(gas)} + e^- \leftrightarrow NO_{2(ads)}^-$$

$$NO_{2(ads)}^- + O_{2(ads)}^- + 2e^- \leftrightarrow NO_{(gas)} + 2O_{(ads)}^{2-}$$

$$NO_{(gas)} + O_{2(ads)}^- + e^- \leftrightarrow NO_{2(ads)}^- + O_{(ads)}^-$$

$$H_2S_{(gas)} + 3O_{(ads)}^- \leftrightarrow H_2O_{(gas)} + SO_{2(gas)} + 3e^-$$
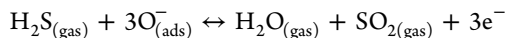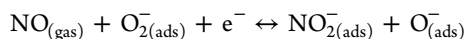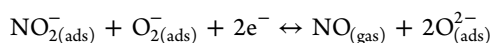
Generally, the sensing efficacy of gas sensors is improved at high temperatures of 100−400 °C due to the encouraged redox reaction of oxygen ions, thereby dramatically inducing the increase of energy consumption, cost, and overall size of the devices. Moreover, operation at high temperatures, which can cause microstructure transformation of the sensing MON resulting in low sensing efficacy, is harmful to flammable and explosive gas sensing applications and flexible substrates. For instance, a ZnO NR-based sensor exhibited an improved response to formaldehyde (HCHO) at 400 °C, which can damage flexible substrates (PET, PI, PDMS, PEN). To overcome these drawbacks, gas sensing applications have been considered to operate at room temperatures. Fortunately, due to the high reactivity of nanomaterials resulting from the high surface-to-volume ratio, single species MON-based flexible gas sensors can operate at low temperatures. However, there was still a limitation of the sensor's performance at low temperatures. To overcome the limitation, several researchers approached the improvement of sensor performance at low temperature via metal-doping and hybridization methods described in section 5, "Strategies to Enhance Sensing Efficiency".

4.1.1. Single Species MON-Based Flexible Gas Sensor.
ZnO, SnO$_2$, In$_2$O$_3$, WO$_2$, TiO$_2$, Fe$_2$O$_3$, MoO$_3$, VO$_2$, CuO, Co$_3$O$_4$, and NiO are common materials used for MON-based flexible gas sensors. Among those materials, ZnO is the most widely used material due to its wide band gap (3.3 eV), high conductivity, biocompatibility, good stability, and high sensitivity for both reducing and oxidizing gases. Several reports have focused on ZnO-nanomaterial-based flexible gas sensors for H$_2$, H$_2$S, O$_2$, NH$_3$, NO$_2$, CO, CH$_3$CHO, and EtOH in the recent decade.

Zheng et al. fabricated light-controlled transparent and flexible EtOH gas sensors based on a thin ZnO NP layer on an indium tin oxide (ITO)-PET substrate.[149] They adjusted the sensor's sensitivity by generating a high density of free carrier and oxygen ions under controlled UV irradiation. The sensor even operates well at a curvature angle of 90°. The ZnO NP-based gas sensor is also fabricated on a biodegradable and flexible CHP substrate.[109] The ZnO nanoparticle layer on a CHP substrate displays an excellent sensitivity value of 69% at 180 °C. At an operation temperature of 150 °C (Table 1), the sensitivity of the ZnO sensor on the CHP substrate is 24% and 46% to 0.5% and 2% H$_2$, better than that of the ZnO sensor on SiO$_2$ substrate of only 10% and 24%, respectively.

ZnO NRs grown on cotton fabric are preferred for wearable gas sensors due to the intrinsically flexible and stretchable properties and the high surface-to-volume ratio of textile structures.[24,105,150] Subbiah et al. demonstrated a wearable gas sensor sensing CH$_3$CHO, NH$_3$, and EtOH at room temperature (RT) by growing ZnO NRs on the surface of a carbon cellulosic fabric by sol−gel and sputter seed layer-coated sol−gel techniques.[105] The gas sensor modified by the sol−gel method showed more sensitive responses to gases than the sensor modified by the sputtered seed layer-coated sol−gel technique. The sensor also showed UV-blocking performance due to a 3.37 eV band gap of ZnO. Lim et al. grew ZnO NRs on fabrics at RT using a scalable solution process and fabricated wearable H$_2$ gas sensors.[150] Also, the H$_2$ sensing performance of the ZnO seed layer, ZnO NRs, and ZnO NRs with Pt catalyst was compared.

One-dimensional (1D) shaped nanomaterials such as NRs and NWs have preferred shapes for sensing materials due to their high aspect and surface-to-volume ratios. Therefore, several studies about flexible/wearable gas sensors based on ZnO 1D nanomaterials have been reported.[24,25,104,107,150] Kwon et al. fabricated a flexible ZnO NR UV/gas dual-sensor through Ag NP templates. ZnO NRs were grown on Ag NP templates. It showed a better sensing performance than the ZnO NP seed layered template and a different sensing performance depending on the size of the Ag NPs because Ag NPs affect the surface depletion region.[104]

ZnO-based flexible/wearable gas sensors usually employ the conductometric method. However, some sensors employed a self-powered voltammetric sensing system using the piezo-electric characteristic of ZnO.[25,131] Xue et al. demonstrated a self-powered active gas sensor based on the fact that absorption gas molecules could modify the density of the surface charge carrier, which largely influences the output of a piezoelectric nanogenerator as shown in Figure 3a.[25] The sensor was fabricated using vertically grown ZnO NW arrays between the Al and Ti layers on polyimide substrates. The sensor showed a lower output voltage toward the higher concentration of H$_2$S and water vapor, as shown in Figure 3b.

In$_2$O$_3$ is also the preferred semiconducting metal oxide material for its wide band gap (3.6 eV) and optical transparency. Therefore, In$_2$O$_3$-nanomaterial-based flexible gas sensors for NO$_2$ and EtOH have been reported. Seetha et al. synthesized In$_2$O$_3$ nanocubes at a low temperature by a modified hydrothermal route and fabricated an EtOH sensor showing fast response and recovery times.[151] The nanocubes obtained flexibility by constituting a composite with poly(vinyl alcohol). Wang et al. fabricated an In$_2$O$_3$ NW-based flexible transparent NO$_2$ sensor operating at RT.[152] To decrease the operating temperature of the sensor, visible light was illuminated on the sensor to reduce the activation energy. Furthermore, the ITO electrode and In$_2$O$_3$ NWs were employed for sensor transparency. The sensor showed highly selective responses for NO$_2$ compared with H$_2$S, NH$_3$, trimethylamine, CH$_3$COCH$_3$, benzene, EtOH, toluene, and xylene.

SnO$_2$ NPs were usually used to fabricate n-type MON-based gas sensors to detect n-butanol (n-BuOH) vapor,[93] CO,[94] NO$_2$,[94,97,153] and NH$_3$.[95] Wang et al. engineered 3D hierarchical SnO$_2$-based gas sensors via a one-step and facile hydrothermal pathway.[93] The hierarchical nanostructure produced a potentially efficient sensing efficiency with fast res/rec times and superior response to ppm n-BuOH. Gas diffusion and mass transport boosted by the 3D hierarchical nanostructure also boosted sensing performance, as shown in Figure 3c−f. Thermal control in spatial and time domains is preferred as a novel approach, reducing the operation energy to 10^2 pJ/s and enhancing the response to 100 ppb n-BuOH. The thermal management of a single SnO$_2$ NW-based flexible NO$_2$ sensor was reported.[97] A pulsed self-Joule-heating of SnO$_2$ NW enhanced sensitivity for NO$_2$ as well as highly

Figure 4. (a) Schematic of the pH-dependent equilibrium potential of the IrO$_x$ NPs film. (b) Measurement of pH level via an IrO$_x$ NPs film. Reprinted from ref 156, with permission from Elsevier. (c) Schematic of enzymatic oxidation of D-glucose via attached glucose oxidase on In$_2$O$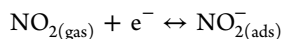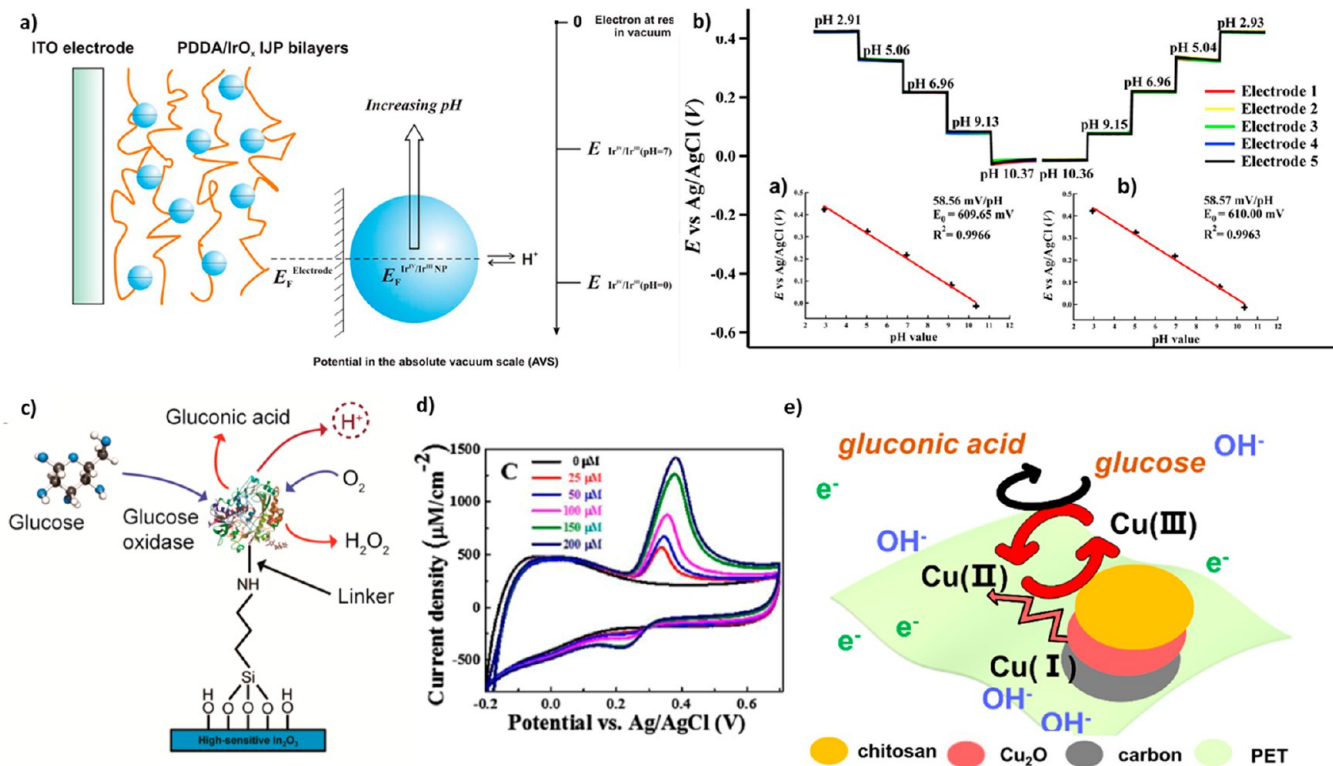_3$. Reproduced from ref 26. Copyright 2015 American Chemical Society. (d) CV response of Fe$_2$O$_3$ NPs directly grown on carbon cloth and with different uric acid concentrations. Reprinted from ref 166, with permission from Elsevier. (e) Schematic of the circumstance of Cu(II)−Cu(III) in electrocatalysis oxidation. Reproduced with permission from ref 141. Copyright 2021 American Chemical Society.

reduced energy consumption. The PEN substrate is destroyed by ordinary external heating at 523 K in Figure 3g,h. Conversely, the pulsed self-heating approach did not cause any damage to the substrate. Additionally, TiO$_2$ has been broadly investigated for gas sensing due to its wide band gap (3.1 eV), low cost, low energy consumption, and unique electrical properties. Indeed, there have been reports of TiO$_2$-nanomaterial-based sensors detecting EtOH[142,154] and NO$_2$.[155] Dubourg et al. annealed the screen-printed TiO$_2$ NPs on a flexible substrate via laser irradiation to fabricate a multifunctional sensor detecting UV and EtOH at RT.[154] The morphology of the TiO$_2$ film was adjusted by the laser irradiation process to enhance the sensor's electrical properties.

4.2. Electrochemical Sensors

The semiconducting properties of MONs make them applicable to electrochemical sensors as well. pH, glucose, dopamine, humidity, heavy metals, cortisol, and urea were measured in an electrochemical way using MON-based flexible sensors. pH sensors are among the simplest electrochemical sensors, commonly measuring surface potential, which is shifted by a redox reaction between metal-oxide molecules on the surface and the hydrogen ions in the solution.[29,156−163] Furthermore, researchers have measured pH levels by detecting the protonation of functionalizing groups on the surface[26,159] or the change of capacitance of the interdigitated impedance metric sensor.[28] In addition, biomaterials including glucose and dopamine were detected by attaching enzymes that induce catalysis to the modified surface of metal oxides. The three-electrode system is commonly employed to measure the electrochemical potential of the metal-oxide sensors

because of its accuracy, but two-electrode systems and extended gate field-effect transistors (EGFET) are also used to fabricate sensing arrays or simplify the sensor.

4.2.1. pH Level Sensors. WO$_3$ and IrO$_x$ were mainly exploited for flexible pH sensors based on MONs. In addition, ZnO, In$_2$O$_3$, indium−zinc oxide (IZO), ITO, and CuO were employed occasionally. The pH sensing mechanism of WO$_3$ can be understood as the formation of H$_x$WO$_3$, namely, tungsten oxide bronze, via the redox reaction of WO$_3$ according to the following equation.[29,157]

$$WO_3 + xe^- + xH^+ \leftrightarrow H_xWO_3$$
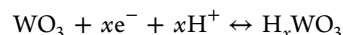
The redox reaction involves the double injection of protons (H$^+$) and electrons (e$^-$) for which the number is denoted as x. Moreover, the reaction mechanism was explained as utilizing a small polaron transition forming the W^{5+} site and Drude-like free electron scattering for amorphous films and crystalline films, respectively. According to both mechanisms, electron localization or delocalization into W atoms results in a shift in the peak potential. Therefore, the measured potential and the pH have a linear correlation according to Nernstain behavior.

A WO$_3$-NP-based pH sensor showing a sensitivity of −56.7 ± 1.3 mV/pH in a pH range of 9−5 was fabricated via electrodeposition of WO$_3$ NPs on metal electrodes on flexible substrates. The flexible sensor was also demonstrated as a conformable reference electrode on the curved surface of the solid electrolyte.[157] In addition, WO$_3$ NRs were directly grown on carbon fiber cloth to sense pH levels. The WO$_3$-NR-modified carbon fiber cloth sensor showed a sensitivity of
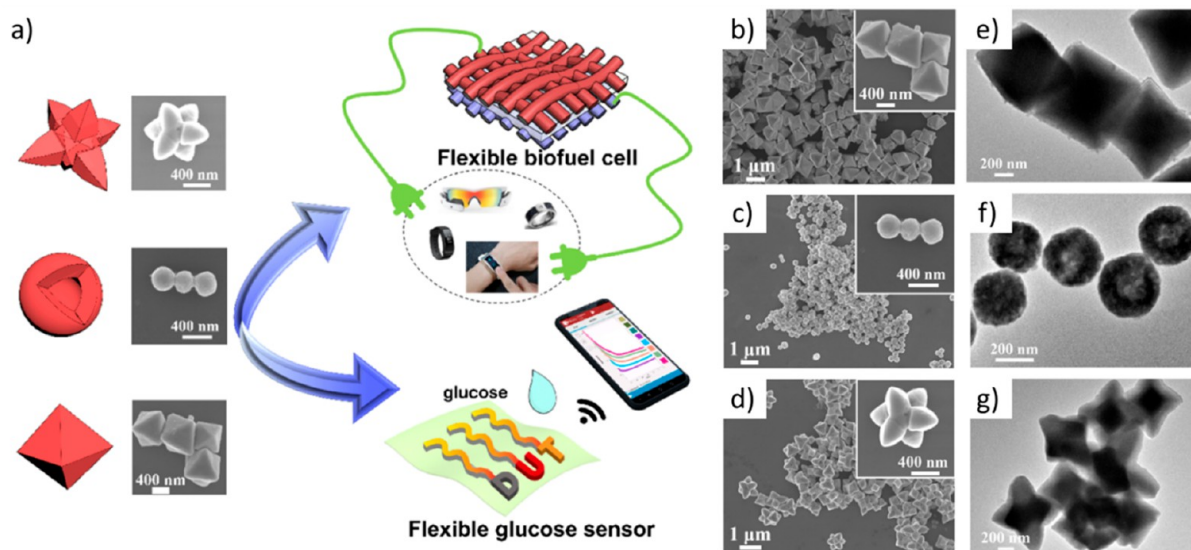
Figure 5. (a) Schematic of preparation of Cu_2O glucose sensor. (b−d) SEM and (e−g) TEM images of octahedral, cuboctahedral, and extended hexapod Cu_2O, respectively. Reproduced from ref 141. Copyright 2021 American Chemical Society.
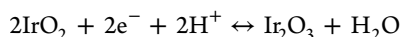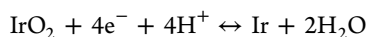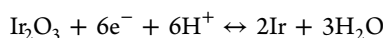
41.38 mV/pH and a response time of 150 s over the pH range of 3−10.[29]

As mentioned, IrO_x was also frequently exploited as materials for flexible pH sensors owing to its high conductivity, fast response, good stability, biocompatibility, and wide responsive range.[156,158,160,161] The pH sensing mechanism of IrO_x is understood as a shift of potential from the redox conversion reaction involving Ir^{4+} and Ir^{3+} as shown by the following equations.

$$Ir_2O_3 + 6e^- + 6H^+ \leftrightarrow 2Ir + 3H_2O$$

$$IrO_2 + 4e^- + 4H^+ \leftrightarrow Ir + 2H_2O$$

$$2IrO_2 + 2e^- + 2H^+ \leftrightarrow Ir_2O_3 + H_2O$$

The pH level can be measured since the electrode's potential is equalized with the Fermi level of the IrO_x and NPs resulting from the redox reaction depending on the pH level, as shown in Figure 4a,b.

4.2.2. Biomaterial Sensors. Additionally, MON-based flexible sensors detecting biomaterials including glucose, dopamine, cortisol, hydrogen peroxide, and urea were frequently reported recently. These materials were commonly detected via catalysis, which can be categorized into two ways which are enzyme reactions[26,116,164] and enzyme-free electrocatalysis.[141,165−167] On the other hand, electrochemical sensors detected a shift of potential due to the chemical combination of biomaterials and attached functionalizing chemical groups including antibodies.[159,168]

In the method using enzymatic catalysis, the concentration of biomaterials in a solution is estimated by detecting byproducts, including hydrogen ions from the reaction. Recently, In_2O_3-nanomaterial-based flexible glucose sensors employing the enzymatic oxidation of D-glucose with glucose oxidase have been reported.[26,116] The concentration of D-glucose was estimated through the pH level determined by the concentration of hydrogen ions generated via enzymatic glucose oxidation in the following equations, as shown in Figure 4c.

$$D\text{-glucose} + O_2 \xrightarrow{\text{glucose oxidase}} \text{gluconic acid} + H_2O_2$$

$$H_2O_2 \rightarrow O_2 + 2H^+ + 2e^-$$
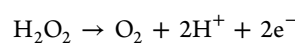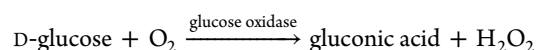
To immobilize glucose oxidase on the surface, an amine-terminated (3-aminopropyl) triethoxysilane and glutaraldehyde linker was assembled to the In_2O_3 surface hydroxyl group.[26]

Fe_2O_3 NPs were also exploited for urea biosensors based on NiO and GO to absorb more enzyme molecules and act as an immobilization carrier.[164] The sensor read the change of pH level of the microsurroundings of the sensing electrode affected byproducts from enzymatic catalysis as following equations.

$$NH_2CONH_2 + 3H_2O \xrightarrow{\text{urease}} 2NH_4^+ + HCO_3^- + OH^-$$
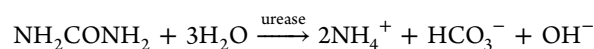
Modifying with Fe_2O_3 NPs on the GO layer enhanced the sensitivity of the sensor.

On the other hand, in the case of the enzyme-free method, electrocatalytic oxidations of biomaterials including glucose,[141,165] dopamine,[166,167] and hydrogen peroxide[169,170] are induced by nanomaterials including $NiP_{0.1}$-SnO_x,[165] CuO,[165] Cu_2O,[141] Pt,[169,170] and Fe_2O_3.[166] The circumstance between several oxidation states of metal atoms that occur through electrocatalysis affects the electrochemical sensor characteristics. Accordingly, the concentration of biomaterials was sensed by specific redox peaks in the CV curve, the open-circuit potential measurement, or the amperometric measurement. For example, Figure 4d exhibits specific peaks of Fe_2O_3 NPs resulting from the redox reaction of uric acid.

In the case of enzyme-free glucose sensors, metal compounds such as $NiP_{0.1}$-SnO_x, CuO, and Cu_2O have been used as the electrocatalyst for inducing glucose oxidation.[141,165] A shift of the electrochemical potential resulted from the reaction allowed sensitive detection of glucose molecules. For instance, the mechanism of electrocatalysis oxidation with Cu and Cu_2O is known as the following equations.[141,165]

$$Cu_2O + 2OH^- \rightarrow 2CuO + H_2O + 2e^- \text{ (Cu(I)}$$
$$\rightarrow \text{Cu(II))}$$
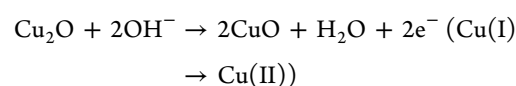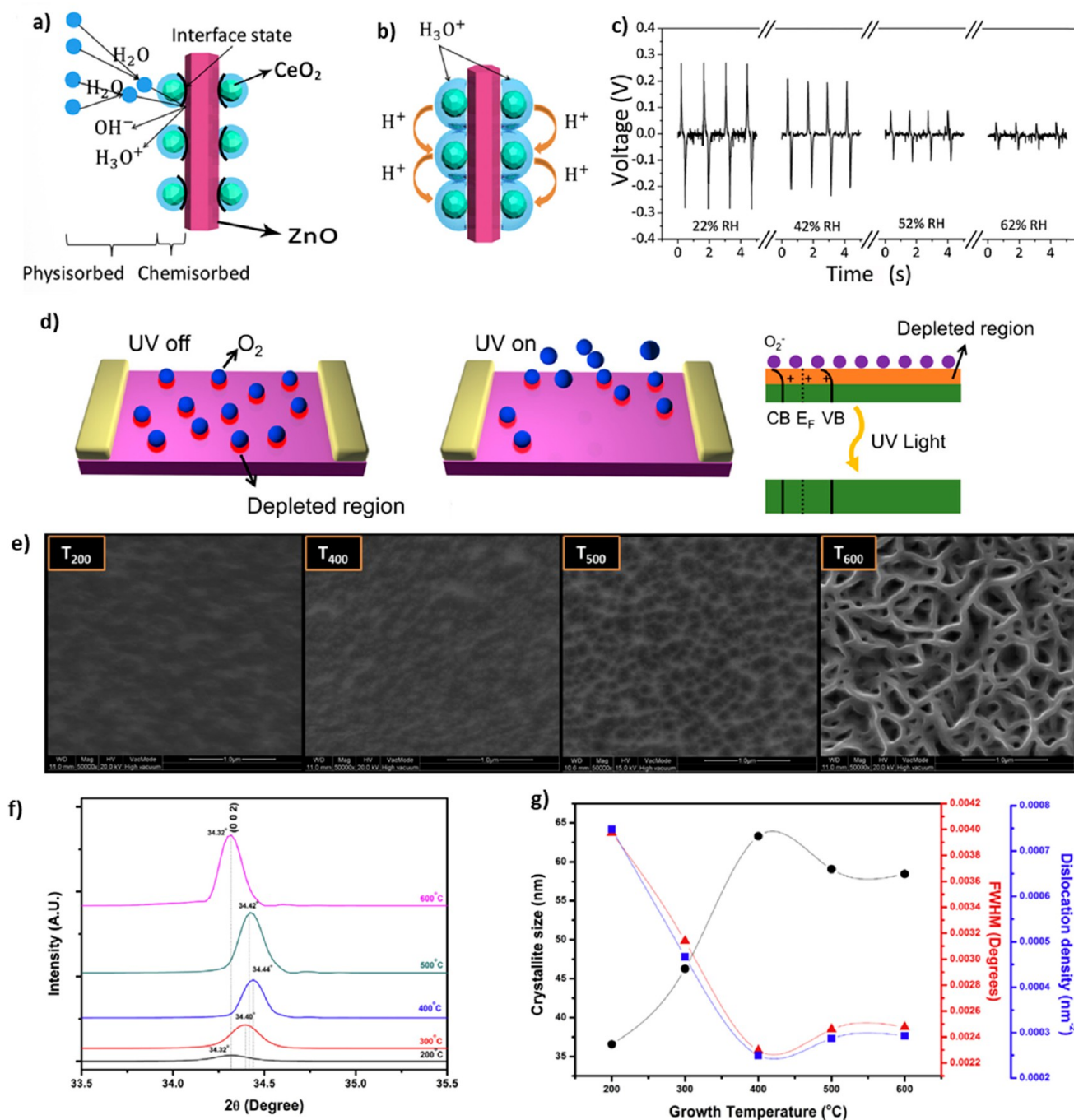
Figure 6. (a,b) Schematics of a CeO$_2$/ZnO NW at (a) low RH and (b) high RH. (c) Output voltage of piezoelectric MONs humidity sensor at different humidity levels. Reprinted from ref 173, with permission from Elsevier. (d) Schematic of UV sensing mechanism. Reproduced from ref 106. Copyright 2019 American Chemical Society. (e) FE-SEM photos, (f) XRD patterns, and (g) crystallite size, density, and fwhm of (002)-indexed diffraction peak of ZnO thin films. Adapted with permission from ref 44. Copyright 2018 Elsevier.

$$CuO + OH^- \rightarrow CuOOH + e^- \ (Cu(II) \rightarrow Cu(III))$$

$$2CuOOH + glucose \rightarrow 2CuO + gluconic\ acid + H_2O \ (Cu(III) \rightarrow Cu(II))$$

$$CuOOH + e^- + glucose \rightarrow CuO + OH^- + gluconloactone \ (Cu(III) \rightarrow Cu(II))$$
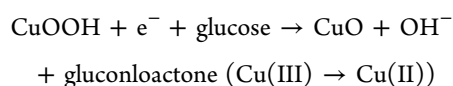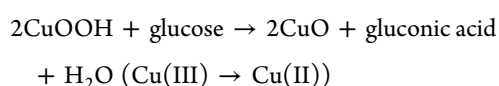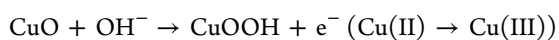
Owing to these oxidation reactions and circumstances of Cu(II)–Cu(III) (Figure 4e), Cu$_2$O- and CuO-based glucose

sensors showed broad oxidation peaks in their CV curves. The shape of Cu$_2$O NPs affects the characteristics in the CV curves due to their different facets. Jiang et al. studied Cu$_2$O-based wearable glucose sensors with various morphologies, such as octahedral, cuboctahedral, and extended hexapod nanostructures via a mild reduction synthesis, as displayed in Figure 5a. Figure 5b−g shows that only the cuboctahedral nanostructure has a specific hollow form with a smaller size while the other exhibited core-solid forms.[141] The average sensitivity of morphologies is in this order: extended hexapod < octahedral < cuboctahedral. Consequently, the cuboctahedral nanostruc-
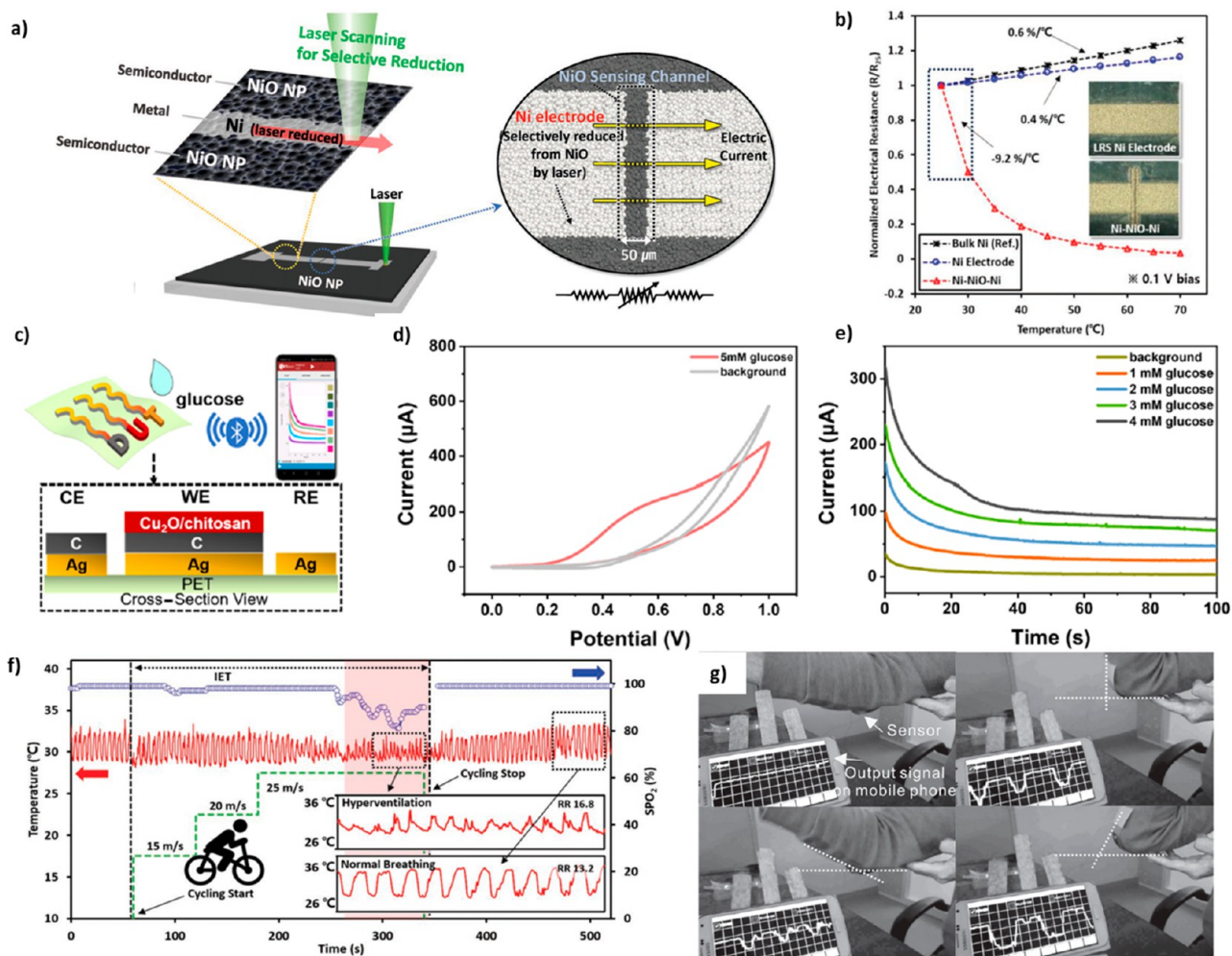
Figure 7. (a) Schematic of the selective NiO reduction technique based on laser process and the fabricated thermistor. (b) Temperature sensing properties of bulk Ni, reduced and sintered Ni NPs film, seamless NiO thermistor. Reprinted from ref 185 under the terms of the Creative Commons Attribution License. (c) Schematic of a real-time glucose monitoring system based on Cu_2O glucose sensor. (d) CV curves exhibiting oxidation peaks at 0.5−0.6 V and e) amperometric curves showing linear response in the range of 0−4 mM from the glucose monitoring system. Reproduced from ref 141. Copyright 2021 American Chemical Society. (f) Real-time monitoring of the respiration and progression of hyperventilation (red area) with the NiO NPs-based thermistor and the conventional SpO_2 monitoring device. Reprinted from ref 185 under the terms of the Creative Commons Attribution License. (g) Demonstration of the real-time wireless arm motion monitoring based on the ZnO/CNT/rGO/PET textile piezoelectric strain sensor. Reprinted with permission from ref 188. Copyright 2016 John Wiley and Sons.

ture (Figure 5c) has (110)- and (100)-exposed facet engineering that provides higher interactions with glucose and electron-accelerated transfer, respectively. As a result, the cuboctahedral Cu_2O-based sensor exhibits the highest selectivity and responsive signal.

4.2.3. Humidity Sensors. MONs including Ce/ZnO NPs,[131] ZnO NWs,[171] and CeO_2 NPs combined with graphitic carbon nitride (g-C_3N_4),[172] ZnO NRs modified with CeO_2 NPs,[173] ZnO NRs modified with SnO_2 NPs,[173] and CuO NPs[28,174] have been widely used for electrochemical sensors detecting humidity recently.

The piezoelectrical response of ZnO decreases in higher humidity; this characteristic was utilized to fabricate humidity sensors.[131,173] D. Zhu drastically enhanced this characteristic by decorating CeO_2 and SnO_2 NPs on the surface of vertically grown ZnO NWs.[173] The decorated ZnO NWs showed an almost doubled response compared to pure ZnO NWs. Basically, the mechanism of humidity sensors based on piezoelectric characteristics can be understood as a piezoelectric potential screening effect owing to the conductive

H_3O^+ ions resulting from adsorbed water molecules which increase at higher relative humidity. Furthermore, decorating CeO_2 and SnO_2 NPs led to not only the adsorption of a greater amount of water molecules, as shown in Figure 6a, resulting in enhancement of the screening effect, but also freely moving H^+ ions in the connected water layer in the highly humid environment, as shown in Figure 6b, further decreasing piezoelectric output. Consequently, the sensor showed a highly sensitive response, as shown in Figure 6c.

4.3. Photodetectors

Photodetectors are also common applications for metal oxides such as SnO_2,[153] ZnO,[104−106,150,175−182] TiO_2,[154] MoO_3,[181] Zn_2SNO_4,[183] and Cu_2O[180] for their semiconducting properties. The UV sensing mechanism can be understood as the photoelectric phenomenon or the photodesorption of oxygen molecules adsorbed on the surface of metal oxides.

For example, in the case of n-type semiconducting metal oxides including SnO_2, ZnO, TiO_2, Zn_2SNO_4, and MoO_3, conductivity is decreased due to the depletion region in the

dark because oxygen molecules trap free electrons to be ionized and chemisorbed on the surface. When light with a higher photon energy than the band gap of the metal oxide is illuminated, the electron−hole pairs are generated photo-electrically. Accordingly, generated hole carriers recombine and discharge negatively charged adsorbed oxygen ions on the surface and increase the free-carrier concentration by reducing the depletion region, as shown in Figure 6d.[106] In other words, the conductivity of the metal oxide increases via the photodesorption of oxygen, induced by the illumination of the light whose photon energy is higher than the band gap. The absorption and the desorption of the oxygen can be described by the following equations.

$$O_{2(g)} + e^- \rightarrow O_{2(ads)}^-$$

$$h\nu \rightarrow e^- + h^+$$

$$h^+ + O_{2(ads)}^- \rightarrow O_{2(g)}$$
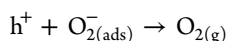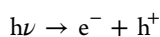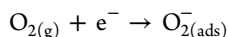
Nanomaterials are considered appropriate for these sensors due to their large surface-to-volume ratio since the trapping of electrons by oxygen occurs on the surface. Furthermore, several groups have studied the control of the shape of NPs to achieve larger surface areas[177,179] and the relationship between geometric characteristics and performance of sensors.[106,154] Shewale et al. explored the sensing performance of ZnO UV sensors fabricated at various growth temperatures.[44] As shown in Figure 6e, the T_{200} (ZnO film grown at 200 °C) surface comprises unevenly sized grains and appears fuzzy, likely resulting from inhibition of grain growth due to a lack of thermal energy. However, the surface grains enlarge adequately at 400 °C and begin to degenerate fairly above 400 °C, resulting in a porous network-like surface structure. It is obvious that the (002) diffraction peak irregularly shifts to a low 2θ above 400 °C (Figure 6f). As confirmed in Figure 6g, the crystallinity of ZnO film is directly proportional to a growth temperature of up to 400 °C due to the mobility boost of atoms on the film surface. The elevated temperatures cause the film surface to re-evaporate, leading to a decrease in film thickness.[112] The as-prepared ZnO-based sensor displayed the best UV response at 400 °C compared to other temperatures.

Two-dimensional (2D) semiconducting nanomaterials are desirable materials for flexible optoelectronics because their ultrathin nanosheet structure results in excellent flexibility and carrier mobility. However, most of them lack spectral selectivity in photodetection due to their narrow band gap, but orthorhombic structured molybdenum trioxide (α-MoO_3) has an exclusive wide band gap (~3.2 eV) which is appropriate to detect UV light. In fact, the flexible UV detector based on α-MoO_3 showed transparency, high UV spectral selectivity, a high responsivity of 18 mAW^{-1} under mechanical deforma-tions.[181]

4.4. Thermistors

Metal oxides, including NiO and doped Mn-spinel oxide, are widely employed to fabricate NTC thermistors because of their high thermal constant values (B-value). However, the high temperature (600−1200 °C) annealing process hindered progress to the fabrication of flexible metal oxides-based thermistors, but the low melting point of nanomaterials avail fabrication of metal oxides-based thermistors at relatively low temperature.

Huang et al. successfully fabricated a flexible thermistor array by inkjet-printing NiO NP ink on a polyimide substrate and annealing at 200 °C.[184] The fabricated thermistor showed high B-values (~4300 K) and good stability in the bending state. Furthermore, RT fabrication processes have been accom-plished by laser sintering techniques.[185] The wearable NTC thermistor was demonstrated with seamless monolithic integration of Ni and NiO by the selective NiO reduction technique based on laser process as shown in Figure 7a. The fabricated sensor showed excellent B-values (~8162 K), as shown in Figure 7b, yet it is fabricated at RT.

Laser sintering processes of spinel Mn−Co−Ni oxide NPs have been studied for the flexible NTC thermistor. Moreover, liquid-phase sintering of Mn−Co−Ni oxide NPs was demonstrated by optimized laser pulse irradiation at RT. Crystal growth from the solid−liquid interface in the photoreaction of NPs resulted in densification, planarization of the sintered film, and highly sensitive performance.[186] Moreover, the mechanical stability of the pulsed laser sintered Mn−Co−Ni oxide NP film was mechanically reinforced by fabrication of the Ag electrode embedded in the CMP structure.[187] The reinforced sensor showed a resistance change of only 0.6% during 10,000 bending cycles.

4.5. Mechanical Sensors

MONs are used as piezoresistive materials,[188,189] piezoelectric materials,[190] and fillers enhancing piezoelectric characteristics in flexible/wearable sensor fabrication, detecting diverse mechanical deformations including bending, stretching, and compression.[191] In particular, ZnO is the most common material used for mechanical sensors because of its magnificent piezoelectric and piezoresistive performance.

The microstructure of ZnO, which includes crystal morphology, crystal size, crystal orientation, aspect ratio, and crystalline density, strongly affects the piezoresistive properties. Therefore, the effect of the aspect ratio of the ZnO structure in the piezoresistive properties was investigated, and the optimized ZnO NW structure hydrothermally grown on the carbon hybrids on the PET textile was fabricated as a wearable bending sensor.[188] Moreover, the sensing performance and mechanical properties of ZnO NPs-based piezoresistive sensors can be enhanced by combining them with another nanoma-terial. The strain sensor composed of ZnO NPs/graphene nanoplatelets nanocomposite showed an extensive working range of up to 44% strain and perfect linearity (R^2 = 0.999) with high sensitivity.[189]

MON fillers such as NiO, CuO, ZnO, and $CoFe_2O_4$ enhance the piezoelectric effect of PVDF by increasing the β phase fraction. Dutta et al. studied a tactile e-skin nanocomposite mechanosensor consisting of PVDF and NiO NPs coated by SiO_2.[191] To achieve a large interference surface between NiO and PVDF and resolve low percolation threshold problems, prevention of agglomeration of the particles was necessary. For this reason, conductive NiO NPs were coated with a nonconductive SiO_2 nanolayer and dispersed well in the PVDF-based nanocomposite. The sensor was constructed as a nanogenerator, and its capacitance, impedance, and output voltage responded to compressive mechanical stimulation.

4.6. Wearable Sensor Applications

The highly advanced flexible electronics technique, that facilitates conformal attachment to human skin and enduring a deformation from human body motion, led to the emergence of wearable electronics. According to these trends, several

researchers have introduced MON-based sensors flexible enough to be utilized as wearables. Furthermore, some researchers demonstrated wearable systems including MON-based flexible sensors.

Fabricating sensors on wearable substrates such as fabrics and fiber is an interesting approach to obtain enough flexibility to undergo mechanical deformation of the human body. ZnO NRs are the approved materials to be grown on fabric or fiber structures. ZnO NRs have been grown on cotton fabrics,[150] Kevlar fiber,[179] PET textile,[188] and carbon fiber[168] through the hydrothermal growth method[150,168,188] and chemical vapor deposition[179] to be used as gas (H_2, EtOH, NO_2), UV, and piezoelectric strain sensors. In addition, ZnO NPs,[105] WO_3 NPs,[29] and α-Fe_2O_3 NPs[166] were also used to fabricate gas and UV, pH, and dopamine sensors on fabrics. Meanwhile, spinning methods including blow-spinning[66] and electrospinning are also good techniques to fabricate fabric-like structures consisting of nanofibers. Moreover, a colorimetric H_2 sensing fiber was fabricated by striping an electrospun nanofiber containing PdO@ZnO NPs.[108]

However, the demonstrations of practical wearable applications using MON-based sensors on fabric and fiber structures are relatively insufficient. Li et al. introduced an E-textile gas sensor by yarning a reduced graphene oxide (rGO)/ZnO nanosheet (NS) hybrid fiber on fabric.[192] The gas sensing textile was stitched on a shirt, and it detected NO_2 successfully. A wireless textile strain sensor was demonstrated based on ZnO NRs and a carbon-nanomaterials coated PET textile. The ZnO-NR-based piezoelectric strain sensor, attached to the elbow of a shirt, transmitted the body motion data to a smartphone via ROIC, MCU, and Bluetooth module.[188] Wang et al. demonstrated multimodal and monolithically integrated wearable sensor applications based on electrospun metals and metal oxides. A 3D-inorganic nanofiber network film (FN) including indium−gallium−zinc oxide (IGZO), CuO, ITO, and Cu was fabricated via blow-spinning. Blow-spun FN fulfilled various functions including switching, gas sensing, strain sensing, photodetection, thermistor, and pressure sensing due to the high adaptability in the material aspects of the fabrications process. The FN was also employed to fabricate a wearable strain sensing e-skin detecting finger motions and a multimodal wearable sensing device integrated into a band.

Contrary to textile-type MON-based sensors, film-type MON-based sensors have been actively studied to extend to wearable applications due to their simple structure and the availability of previous research allows easier approaches to stable and high performance devices. MON-based wearable sensor applications were commonly exploited for health-monitoring and detecting human physiological information, such as sweat,[116,141,158,168] skin dryness,[172] respiration,[131,172,185] body temperature,[129,185] and human motion,[188,191] that can estimate and monitor human conditions via MON-based flexible/wearable sensors.

Sweat analysis is widely exploited to obtain physiological information from biomarkers in the composition of sweat. There has been literature that obtained physiological information from human sweat using MON-based electrochemical sensors. Cortisol concentration in human sweat samples was measured by cortisol-antibody modified ZnO NRs, integrated with the flexible carbon fibers.[168] Furthermore, Jiang et al. developed a wireless real-time glucose monitoring system based on a wearable Cu_2O NP sensor.[141] The obtained

real-time concentration data was transmitted to a smartphone via Bluetooth communication. (Figure 7c−e) The real-time glucose monitoring technology was expected to be developed for generalized healthcare applications, including preliminary medical diagnosis, chronic self-management. Also, wearable In_2O_3 nanoribbon transistor biosensor was developed.[116] Chitosan, carbon nanotubes (CNTs), and glucose oxidase were coated on the source and gated electrode of an In_2O_3 FET to detect glucose in body fluids. Therefore, the wearable sensor recognized the concentration of glucose in artificial sweat on an artificial eyeball and hand. Also, the sensor recognized real sweat collected before and after glucose beverage intake. The pH level of human sweat is also a useful parameter that can detect human activities. Zhou et al. demonstrated wireless real-time pH analysis with a smartphone and wearable epidermal electrochemical sensing device based on IrO_x NWs during running.[158] The mounted device on the arm skin of the runner recorded the pH level every 5 min, and the pH decreased during running and slightly increased during rest.

Also, perspiration can be tracked through the difference in chemical and thermal properties of inhaling and exhaling breath. The detection of human physiologic information based on humidity was revealed via a flexible wearable humidity sensing system based on cerium oxide/graphitic carbon nitride nanocomposite.[172] The sensor attached to the human skin estimated different speeds of running states based on the measurement of the dryness of the skin. Also, long-time sitting monitoring was demonstrated through humidity detection via an attached sensor system on the cushion. Furthermore, a self-powered respiratory pattern sensing system based on a cycle and humidity sensor was developed and measured respiratory rate depending on the speed of the cycle. In addition, a self-powered wearable respiration monitoring system based on Ce-doped ZnO NPs flexible sensor detecting NH_3 was demonstrated.[131] The system included a Ce-doped ZnO-NP-based flexible triboelectric sensor, the sensor attached to the chest generates a voltage by the expansion and contraction of the chest during respiration, and NH_3 contained in the exhaled breath supplied through the tube connected to the mouth affects the generated voltage. Therefore, the speed and the intensity of the respiration and the concentration of NH_3 in the breath were measured. The respiratory pattern was also measured by detecting a slight temperature change of philtrum resulting from respiration via an attached epidermal physiological temperature sensor fabricated by laser sintering of NiO NPs.[185] The sensor measured the respiratory rate and intensity and respiratory symptoms of hyperventilation due to the metabolic need resulting from intense physical activity, as shown in Figure 7f. Park et al. also introduced La-doped Al_2O_3-based wearable temperature sensors for body temperature monitoring systems.[129] The capacitance of the La-doped Al_2O_3 nanofilm indicated temperature. Moreover, they established a wearable body temperature sensor device in the form of an armband, which could lead to a potential path for wearing bioelectronics.

Conventional mechanical sensors like strain gauges based on rigid metals were not suitable for health monitoring, including capturing the posture or motion of humans due to their limited range of strain and flexibility. However, flexible/wearable MON-based mechanical sensors suitable to monitor human motion were reported. Dutta et al. developed a tactile e-skin piezoelectric mechanosensor based on NiO@SiO_2 NPs and a
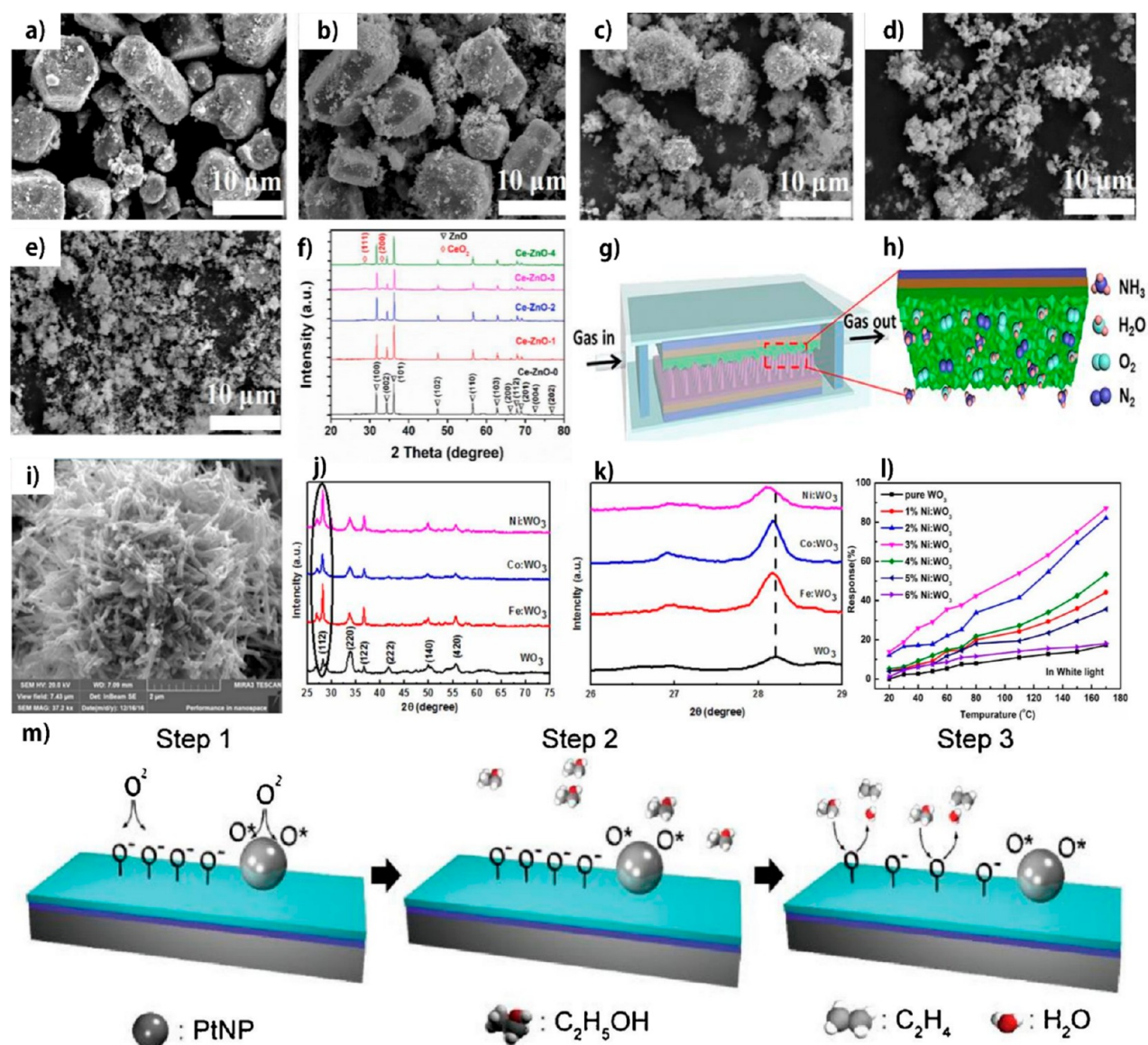
Figure 8. (a−e) SEM photos of Ce-ZnO at various Ce-loading amounts: (a) CeZn-0, (b) CeZn-1, (c) CeZn-2, (d) CeZn-3, and (e) CeZn-4. (f) XRD patterns of (a−e). (g) Diagram of the fabricated TSRS. (h) Focused view of the Ce-ZnO active layer. Adapted with permission from ref 131. Copyright 2019 Elsevier. (i) SEM photo of Ni-WO$_3$ NFs. (j) XRD patterns of WO$_3$ with various dopants. (k) Focused XRD patterns of j). (l) The 100 ppm acetone response of pristine WO$_3$ and Ni-WO$_3$ with various Ni-loading amounts. Adapted with permission from ref 132. Copyright 2021 IOPscience. (m) Sensing mechanism of ethanol detection of Pt nanoparticle/In$_2$O$_3$. Reprinted from ref 37, with permission from Elsevier.

PVDF composite.[191] The sensor was fabricated in typical piezoelectric energy harvester form and showed the output voltage and current depending on applied diverse mechanical stimulation such as pressure, stretching, and bending. Also, the capacitance and the impedance changed linearly according to the intensity of the static pressure. Measurements of voltage generation by bending motions of various fingers and mechanosensory array mapping distribution of the pressure were demonstrated. A wireless wearable textile strain sensor based on the piezoresistive characteristic of ZnO NWs was reported.[188] The resistance of a ZnO/CNT/rGO/PET textile embedded in PDMS was measured by a readout integrated circuit, converted to digital data by the MCU, and subsequently transmitted to mobile phones wirelessly via a Bluetooth module. The wireless monitoring of the arm bending motion was exhibited through the sensing system, as shown in Figure 7g.

Also, there was a multifunctional wearable application for human−machine interfaces (HMIs).[193] A sol−gel-on-polymer-processed IZO nanomembrane was exploited to achieve UV, temperature, and strain sensing ability and construct resistive random-access memory and FET for interfacing and switching circuits. Moreover, a serpentine pattern of a Au thin film electrode was employed to obtain stretchability. The IZO nanomembrane and Au electrode were encapsulated by the PI layer, and appropriate pattern designs were applied depending on the types of the sensors. The HMI not only recognized the motion of the arm and finger while attached on human skin, but also sensed humans touch via a temperature sensor while attached to a robot hand. Also, the HMI was able to deliver temperature via integrated microheaters.

5. STRATEGIES TO ENHANCE SENSING EFFICIENCY

To improve the sensing performance of MON-based flexible sensors, several materials and modifying strategies such as low-dimensional carbon materials (graphene, rGO, and CNT), 2D materials (TiC, g-C_3N_4), PANI, metal sulfides, heterogeneous metal-oxide structure, and surface modification with noble metals have been studied. Modified MONs are of great interest due to their adjustable optoelectronic, optical, electrical, thermal, magnetic, catalytic, mechanical, and photochemical properties while also promoting long-term stability. These strategies also have been applied at once in a single sensor (Table 1).

5.1. Metal Doping

Doping is a powerful way of manipulating metal-oxide features such as oxygen vacancies, electrical conductivity, band gap, lattice parameters, and magnetic properties. The sensing ability is mostly determined by various carrier defects, mainly oxygen vacancies. Doping species, also called dopants, can tune the crystal structure and escalate defects and reaction sites. Furthermore, dopants could reduce the activation energy between the target analytes and the sensing material, boosting the sensor's performance.[128]

Hu et al. employed different metals (Cu, Co, Ni, and Sn) as dopants in plasma-enhanced chemical vapor deposition (PECVD) to create metal-doped ZnO-NR-based HCHO sensors. The introduction of metal doping can reduce the working temperatures and improve the sensing efficiency due to the reduced activation energy; Co-, Ni-, and Sn-doped ZnO NRs result in the highest response at 300 °C at which PI substrates can be used. Among metal dopings, Sn-doped ZnO NRs synthesized by PECVD exhibit a maximum response of 90% with Sn at 0.5% compared to ZnO NRs synthesized by precipitation and hydrothermal methods due to extensive crystal defects.[194] The metal doping concentration can directly influence the morphology of the materials, leading to a high sensing efficiency.[131] As seen in Figure 8a, pure ZnO NRs display a typical wurtzite hexagonal shape. On the other hand, the morphology of the Ce-ZnO composite changes slowly to NPs with increasing Ce-doping concentrations, as seen in Figure 8b,c. Consequently, the shape transforms to flocculent structures with partial agglomeration when the Ce-doping concentration is further increased (Figure 8d,e). Metal-doped triboelectric nanogenerators have been extensively exploited for self-powered respiration monitoring due to their appealing characteristics, including superior biocompatibility, low price, wearing ease, and excellent response to respiration activities. Wang et al. engineered a triboelectric self-powered respiration sensor (TSRS) based on a Ce-ZnO composite on a PET substrate, as observed in Figure 8f–h.[131] Ce concentrations of 0, 0.001, 0.004, 0.007, and 0.01 M are indicated as CeZn-0, CeZn-1, CeZn-2, CeZn-3, and CeZn-4, respectively. Among these Ce concentrations, CeZn-2 exhibits the best selectivity and response value toward 20.13 ppm of NH_3. Furthermore, the sensor displays a stronger NH_3 response at low concentrations (0.1−1 ppm) than at large concentrations (1−10 ppm) when exposed to the same moisture as the breathing gas, demonstrating that TSRS can detect trace levels of the NH_3 biomarker in human breathing gases.[131] Another group developed a Cr-doped ZnO-based NH_3 sensor with different Cr-doping ratios. Cr-ZnO with a 3 mol % Cr-doping concentration acquires the highest response efficiency due to the generation of extensive chemisorbed surface sites. In

comparison, the surface becomes rougher at higher doping concentrations. It can be interpreted as that extra Cr dopants cause the agglomeration that cannot substitute Zn^{2+} ions in the wurtzite structure. Furthermore, Cr dopant boosts UV−vis absorption while decreasing the energy band gap.[128] Namgung et al. used Al-doped ZnO NRs to fabricate low-temperature gas sensors and employ a Ag NW layer to compensate for the decreased conductivity due to Al doping.[195] The fabricated sensor successfully sensed H_2 and NO_2.

Pi et al. investigated the sensing efficiency of WO_3-NF-based acetone (CH_3COCH_3) sensors with different dopants, such as Co, Fe, and Ni.[132] Via a hydrothermal method, metal-doped WO_3 NFs were fabricated and showed a porous structure as shown in Figure 8i. Figure 8j,k indicates the different dopants are successfully doped on the WO_3 surface, which exhibits a higher sensitivity to 100 ppm of CH_3COCH_3 than that of pure WO_3 under various light sources (UV, green, and white lights). The Ni-WO_3 composite displays the highest response under white light irradiation compared to other composites at the same intensity. Besides the effect of light irradiation, Figure 8l realizes the efficiency of Ni-doping concentrations at different working temperatures. At room temperature (RT), Ni-WO_3 NFs have a sensitivity of 27%, whereas pure WO_3 has almost no sensitivity without light irradiation. Park et al. produced lanthanum (La)-doped Al_2O_3 on PI substrate (Table 1) via a sol−gel method to develop capacitive-type flexible temperature sensors that operate at 1 V, 1 MHz achieving a good sensitivity across an extensive temperature range (30−200 °C) as well as excellent mechanical properties in cyclic bending tests with a 5 mm curvature radius.[129] They established a wearable body temperature sensor device in the form of an armband, which could lead to a potential path for wearing bioelectronics.

Employing a nanomaterial as a catalyst is a widely used method to improve the sensing performance of MON-based flexible gas sensors. Noble metals such as Pd,[196] Ag,[195] and Pt[37,150,197] are well-known as dissociation catalysts for gases including H_2,[150,196] NO_2,[197] and O_2.[37,195] These noble metal NP catalysts were exploited to detect NO_2,[195,197] H_2,[150,196] and EtOH.[37] Figure 8m shows the catalysis of Pt NPs in the EtOH sensing process of In_2O_3. Adsorbed oxygen molecules on the surface of In_2O_3 were dissociated to O^- species, and the O^- species reacted to EtOH molecules at exposure. At ambient temperature, the Pt NPs/In_2O_3-based sensor can detect 238 ppb of EtOH vapor. Furthermore, the response reaches 105 ± 15 as the density of Pt NPs changes from 8 to 163 μm^2 due to the increased charged oxygen ions and specific surface area. As the density of Pt NPs exceeds 163 μm^2, this response is unchanged.[37] Rashid et al. decorated Pd NPs on ZnO NRs using a sputtering method.[134] The loading time is directly proportional to the thickness of the Pd layer. The Pd-doped ZnO at 15 s loading time displays a high response of ∼91% at RT and is stable until 10^5 bending/relaxing cycles for 1000 ppm of H_2. The response time is also rapid, i.e., 18 s, with a LOD of 0.2 ppm, while the shorter loading time shows a lower response. Khan et al. produced Pd-doped SnO_2 NPs on PI substrates via the inkjet-printing method.[94] The chemo-resistance response for 50 ppm of CO in dry air is 2.1, while the response for NO_2 at 5 ppm is 3.4. The response to CO is practically halved in wet air. Yang et al. functionalized CeO_2 NPs with various noble dopants, namely Au, Ag, and Pd, via a mild thermal method. Ag- and Pd-CeO_2 NPs displayed random aggregation like CeO_2 NPs.[130] While functionalized CeO_2 NPs with Au NPs displayed a flake structure, the Au-
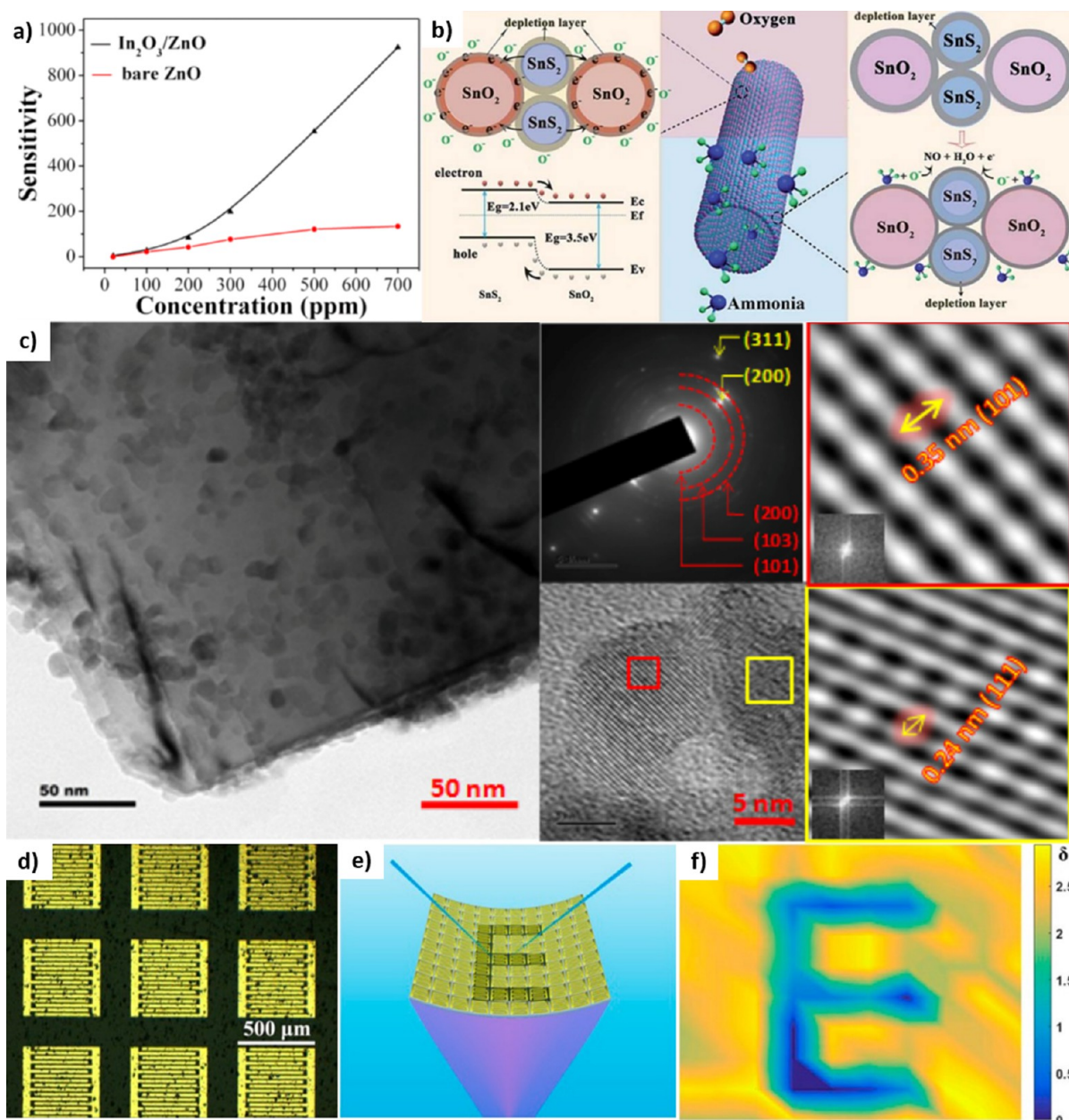
Figure 9. (a) Comparison of In_2O_3/ZnO heterostructure sensitivity and bare ZnO-based H_2S gas sensor. Reproduced from ref 202. Copyright 2014 American Chemical Society. (b) Schematic of the mechanism of SnO_2/SnS_2 heterojunction enhancing sensing performance. Reprinted from ref 96 under a Creative Commons Attribution 3.0 Unported License. (c) TEM, SAED, and focused TEM data of TiO_2@2D-TiC NSs hybrid. Reproduced from ref 142. Copyright 2019 American Chemical Society. (d) Optical image of the photodetector array based on the ZnO NP modified Zn_2SnO_4 NWs. (e) Schematic of the photodetector array sensing the letter "E" under compressive bending. (f) Resulting output image from the flexible photodetector array. Reproduced from ref 183. Copyright 2017 American Chemical Society.

CeO_2 NPs achieved the highest sensing efficiency to gases in the order SOF_2 < SO_2 < H_2S at 100 °C, versus Ag-CeO_2NPs, Pd-CeO_2 NPs, and pristine CeO_2NPs, while Pd-CeO_2 NPs showed the highest sensitivity to SO_2F_2 at 250 °C due to the largest surface area.

Also, localized surface plasmon resonance (LSPR) can improve the response. For instance, ZnO NRs were hydrothermally grown on a Ag NP template to cause LSPR. The interaction with the Ag NPs intensely scattered the incident light through the LSPR, and absorption intensity increased. As a result, the photoresponse of the sensor was improved.

5.2. Hybridization

Hybridization is preferred owing to the synergistic effects of MON properties with another material, especially superior chemical and mechanical features. Generally, both n-type and p-type MONs facilitate core−shell heterostructures that have shown promising results, possibly because excited electrons of n-type that transfer to p-type holes get moved in the reverse direction until equilibrium is reached at the Fermi level. As a result, the formation of hole depletion layers increases chemisorbed oxygen species as well as increases the oxidation reaction on the sensing surface, increasing the resistance of materials.[199] Comprehensive studies have been carried out in recent years, demonstrating that hybridization is superior to
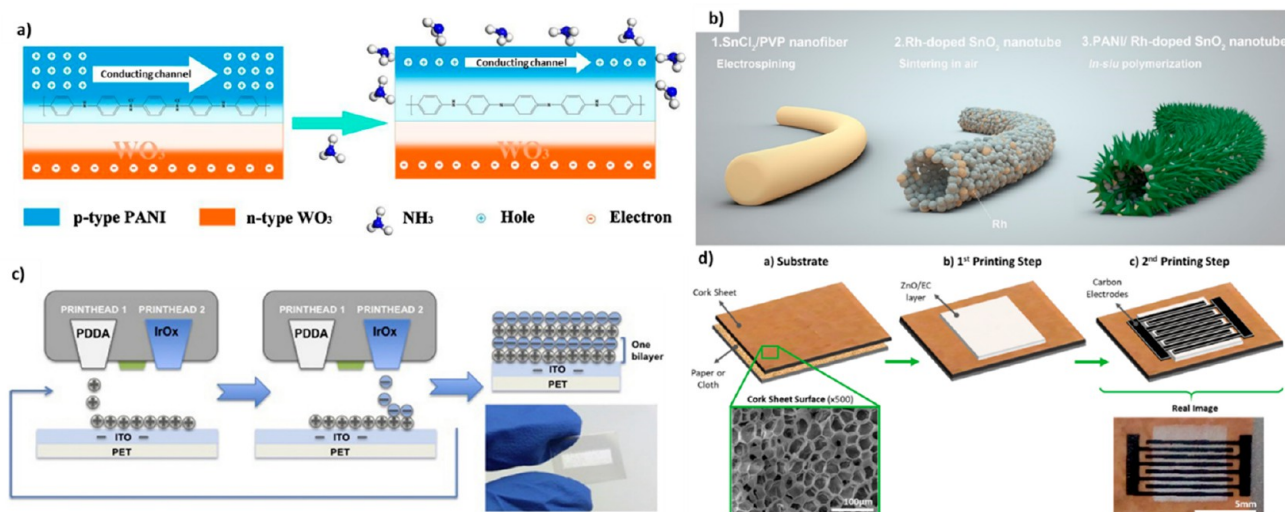
Figure 10. (a) Sensing mechanism of the NH_3 of PANI/WO_3 composite. Reprinted from ref 206, with permission from Elsevier. (b) Schematic of the preparation of PRS NT-based NH_3 sensor. Adapted with permission from ref 95. Copyright 2021 Elsevier. (c) Schematic of layer-by-layer inkjet-printing approach of negatively and positively charged particles for pH sensing. Adapted with permission from ref 156. Copyright 2018 Elsevier. (d) Preparation of ZnO/EC nanocomposite for UV sensing, Reprinted from ref 178 under a Creative Commons Attribution 4.0 International License.

conventional MONs in diverse sensing areas of gas sensors, humidity sensors, and biosensors. The main aim of the sensing facilitates the robust target response at optimal temperature.

5.2.1. Binary Hybridization with an Inorganic Material. Several studies have improved the performance of sensors through synergetic effects by combining different types of oxides. For an example of heterogeneous MONs of flexible gas sensors, Liu et al. introduced porous SnO_2/Zn_2SnO_4 nanospheres.[200] Zn_2SnO_4 is a desirable n-type semiconductor due to its high conductivity, electron mobility, and chemical stability, and Zn_2SnO_4 becomes more attractive when it combines with SnO_2 since SnO_2 assists electron−hole separation because of its higher conduction band position of Zn_2SnO_4. Thus, SnO_2 performs as a sink, enhancing the electrical conductivity of the SnO_2/Zn_2SnO_4 nanosphere and improving gas sensing performance. Also, ZnO nanothorns grown on the surface of NiO nanocones were introduced to improve the response and recovery time of the flexible gas sensor because abundant negative charge carriers in ZnO accelerate the adsorption and desorption of gas molecules.[201] The response/recovery speed and sensitivity of the NiO/ZnO-based NH_3 sensor showed less dependence on the humidity and temperature than those of pure NiO nanomaterials-based sensors. Moreover, In_2O_3/ZnO heterostructure nanoarray-based self-powered gas sensors that achieved high sensitivity and selectivity toward H_2S were reported.[202] Since the conversion of In_2O_3/ZnO to In_2S_3/ZnO, which occurred during the sensing process, strongly adjusted the free-carrier piezo-screening effect of ZnO rather than the gas adsorption, the sensor showed a higher sensitivity than pure ZnO-based sensor as shown in Figure 9a.

Metal sulfides were also exploited to construct heterogeneous structures of nanomaterials for flexible gas sensors and enhance the sensing performances. Li et al. demonstrated a SnO_2/SnS_2-NT-based adjustable NH_3 gas sensor at RT.[96] Since the conduction band of SnO_2 is higher than that of SnS_2, the SnO_2/SnS_2 heterojunction leads to the construction of the accumulation layer on the surface of SnO_2 and the thin depletion layer on the surface of SnS_2, as shown in Figure 9b.

The hybridized SnO_2/SnS_2 sensor promotes a superb response value of 2.48 to 100 ppm of NH_3 versus pristine SnO_2 NTs due to the synergetic effect of the two different materials. Furthermore, ZnS was employed to enhance the stability of the H_2S sensing ZnO. In fact, ZnO NWs are unsuitable materials for the H_2S sensor because ZnO reacts with H_2S and transforms to ZnS irreversibly, but Yang et al. demonstrated a ZnO/ZnS core−shell NW-based H_2S sensor by sulfurizing the surface of the ZnO NWs.[110]

MXenes, emerging 2D materials including $Ti_3C_2T_x$ and TiC, known as suitable materials to decrease the signal-to-noise ratio of the gas sensor, were also studied to improve MON-based flexible sensors. For instance, a wearable and flexible EtOH sensor based on TiO NPs grafted on 2D-TiC NSs operating on a PET substrate at RT was reported.[142] Schottky-type p−n junctions formed at the TiO_2/TiC interface improved the response, selectivity to EtOH gas, and signal-to-noise ratio of the sensor. The hybrid NS surface with the uniform organization of TiO_2 NPs (Figure 9c) generates an outstanding amount of chemisorbed O_2 sites, resulting in excellent response and selectivity to 10 ppb to 60 ppm of EtOH. In addition to the 2D structure, 3D structured MXenes were applied to the MON-based flexible gas sensor. 3D crumpled MXene, $Ti_3C_2T_x$, spheres decorated with ZnO NPs were developed via ultrasonic spray pyrolysis self-assembly and utilized as the NO_2 sensing material.[203] The crumpled structure of the MXene sphere possesses a larger specific surface area and more plentiful edges and defects than the 2D MXene sheet, resulting from the crumpled geometry and p−n heterojunction between MXene and ZnO. Moreover, these characteristics enhanced the responsive intensity, gas absorbing property, selectivity toward NO_2 gas, and res/rec times of the sensor.

Arrays of photodetectors also were developed as flexible image sensors. Li et al. fabricated drastically improved flexible UV photodetectors composed of ZnO NP decorated Zn_2SnO_4 NWs.[183] Due to the type II heterojunction between ZnO NPs and Zn_2SnO_4 NWs, electron−hole pairs were effectively separated and trapped holes in ZnO NPs resulted in a local
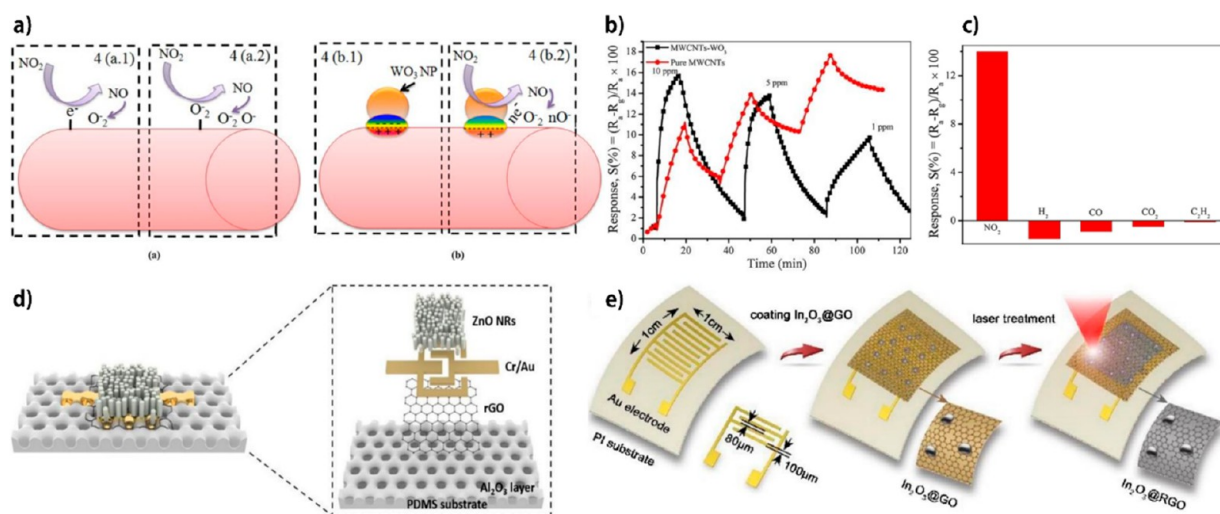
Figure 11. (a) NO$_2$ sensing mechanism of pure MWCNT and WO$_3$ NPs decorated MWCNT. (b,c) Comparison of pure MWCNT and WO$_3$ NPs decorated MWCNT in (b) response and recovery of the sensing signal and (c) selectivity. Reprinted from ref 211, with permission from Elsevier. (d) Schematic of an rGO/ZnO NRs gas sensor. Adapted with permission from ref 127. Copyright 2021 Elsevier. (e) Schematic illustration of the fabrication of flexible NO$_2$ sensors based on In$_2$O$_3$@rGO. Adapted with permission from ref 133. Copyright 2018 Elsevier.

positive gating effect to the n-type Zn$_2$SnO$_4$ NW channel, inducing augmentation of electron concentration in the NWs. The ZnO NP decoration improved the responsivity of the UV photodetector via this mechanism. Furthermore, UV image sensors were demonstrated by fabricating 10 × 10 arrays of the photodetectors to detect images under diverse bending states (Figure 9d−f).

5.2.2. Binary Hybridization with an Organic Material.
5.2.2.1. Hybridization with Polymer. PANI, a p-type semiconducting polymer, can be used as a detecting material of NH$_3$ sensors because =NH$^+$− and −NH$_2^+$− groups of PANI provide protons to NH$_3$ molecules.[204] However, its development has been hindered by its low reaction, delayed response, and recovery. PANI can be composited with n-type MONs such as SnO$_2$,[95,205] CeO$_2$,[198] WO$_3$,[206] SnO$_2$/Zn$_2$SnO$_4$,[200] and SeGe$_4$O$_9$[207] which highly enhances its sensing characteristic due to the p−n heterojunction formed at the interface between PANI and MONs. Figure 10a shows the NH$_3$ sensing mechanism via PANI and n-type MON heterostructures. When PANI is exposed to NH$_3$, NH$_3$ induces the transformation of PANI from the emeraldine salt form to the emeraldine base form and increases the resistance of PANI by capturing protons to NH$_3$. Therefore, the depletion region at the PANI side of the p−n heterojunction becomes larger. Accordingly, the conducting channel of PANI becomes narrow and its resistance increases. Liu et al. reported the hybridized heterostructure of PANI and Rh-SnO$_2$ hollow NTs (PRS) via electrospinning and in situ polymerization approaches, which exhibited a NH$_3$ sensor with a hollow tubular structure, as shown in Figure 10b.[95] The hybridization structure demonstrated the greatest sensitivity value of 13.6 to 100 ppm of NH$_3$ with outstanding selectivity and good reliability. Furthermore, this heterostructure can be monitored by the polymerization method. The introduction of metal oxides possibly tunes the hybridization morphology. Another group fabricated PANI-CeO$_2$ NP hybrid NH$_3$ gas sensors on PI substrates via a deposition method.[198] CeO$_2$ NPs could influence the morphology of the PANI shell by arranging the PANI chains. This hybridization-based sensor gained an increased res/rec time, superb reproducibility, and linear concentration response

as well as excellent selectivity and stability. On the other hand, it achieved an ultralow LOD (0.274 ppb) and exceptional flexibility without reducing sensitivity after 500 bending/extending cycles. By taking advantage of the piezoelectric and excellent mechanical properties of polyvinylidene fluoride (PVDF). A self-powered pH sensor is constructed on a hybrid composite-based piezoelectric nanogenerator (PNG) of ZnO NWs and PVDF.[208] Due to the homogeneous and disaggregated ZnO NWs in the film, this hybrid nanogenerator produces a maximum open-circuit voltage and short-circuit current corresponding to 6.9 V and 0.96 μA, respectively, under uniaxial compression. Also, it operated five green LEDs without the assistance of energy. An inkjet-printed IrO$_x$-based flexible pH sensor was demonstrated by layer-by-layer printing IrO$_x$ NPs and polydiallyldimethylammonium (PDDA) on the ITO/PET electrode, as shown in Figure 10c.[156] The PDDA/IrO$_x$ bilayer was printed in up to five layers since the negatively charged PDDA polymer functioned as an adhesive layer between the positively charged substrate and IrOx NPs as well as between positively charged IrO$_x$ NP layers. The inkjet-printed sensor showed a rapid, linear, and near-Nernstain pH response of 59 mV/pH. IrO$_x$-based pH sensing two-electrode system arrays have been fabricated via a sol−gel process over metal electrodes on PI substrates.[160,161]

The conductive H$_3$O$^+$ ions provided by water molecules adsorbed by CuO NPs also reduced the resistance of the PVA-PEO-CuO nanocomposite.[174] The porous structure of the composite also is speculated to enhance the humidity sensing performance. A sustainable, flexible UV sensor was also revealed based on MONs. Figueira et al. fabricated a sustainable, flexible UV sensor by printing ink containing ZnO NPs and ethylcellulose (EC) on cork substrates.[178] The fabrication process was entirely conducted by screen printing, as observed in Figure 10d.

5.2.2.2. Hybridization with Carbon Materials. Carbon nanomaterials are widely used as gas sensing materials. Moreover, enhancing the sensing performance by hybridizing with metal oxides has been reported frequently due to their high carrier mobility and outstanding mechanical properties. Also, MON-based flexible gas sensors modified with carbon
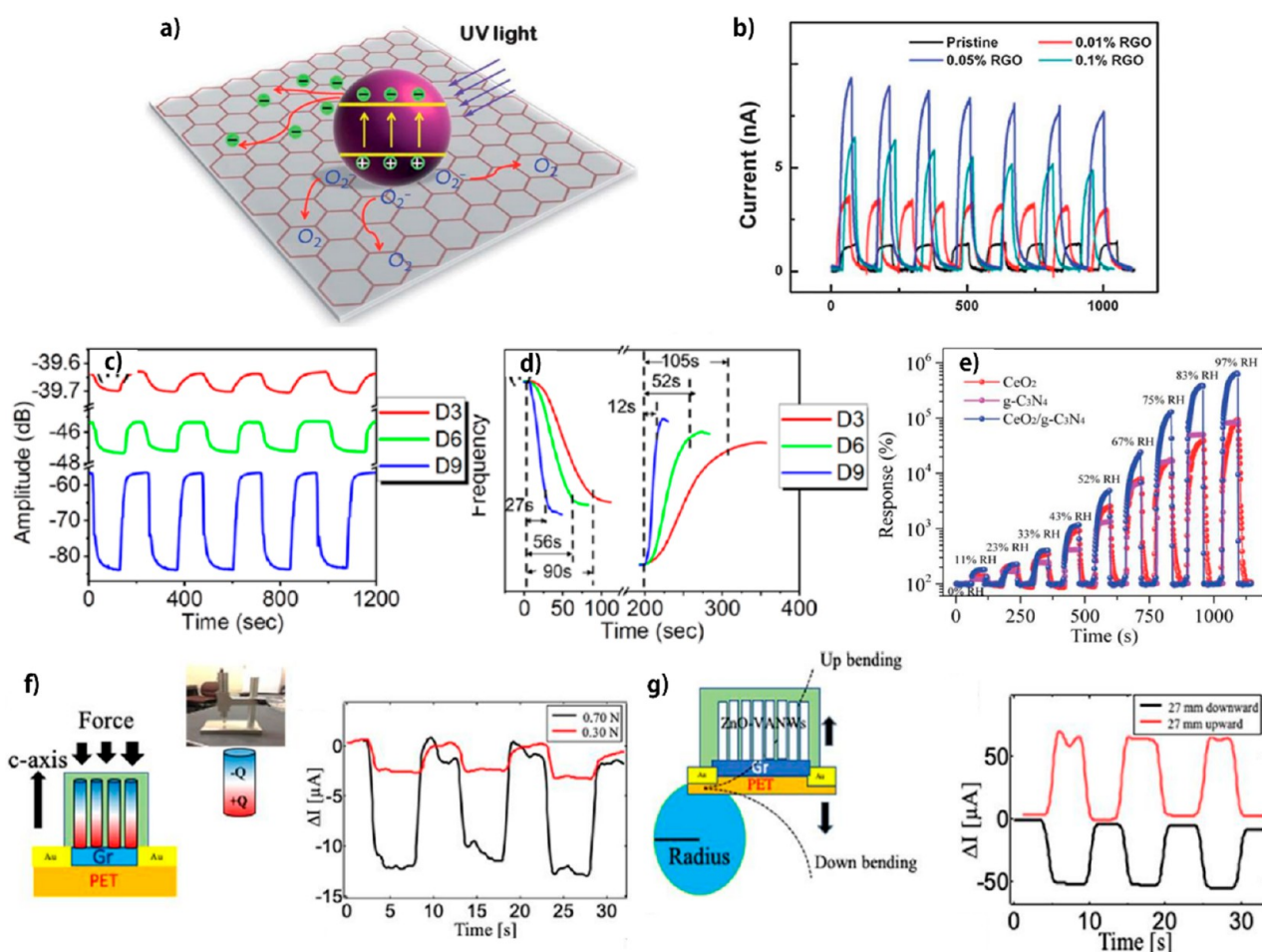
Figure 12. (a) Schematic of the charge separation/transfer in rGO/ZnO composite under UV illumination. (b) Responsive current comparison of the pristine ZnO NPs, rGO(0.01%)/ZnO NP composite, rGO(0.05%)/ZnO NP composite, and rGO(0.1%)/ZnO NP composite under repetitive UV irradiation. Reprinted with permission from ref 182. Copyright 2012 Royal Society of Chemistry. (c,d) Response characteristics of the SAWs with different electrodes (D3, D6, and D9 are clean surfaces without a sensing layer, ZnO NWs and low-concentration GQDs (0.1 mg/mL), and ZnO NWs and high-concentration GQDs (2 mg/mL), respectively) for switching from 30 to 70% RH. Reproduced from ref 171. Copyright 2020 American Chemical Society. (e) Responses of CeO_2, g-C_3N_4, and CeO_2/g-C_3N_4 composite with different humidities. Reprinted from ref 172. Copyright 2021 Royal Society of Chemistry. (f,g) Schematics and piezoelectric responses of the vertically grown ZnO NWs mechanical sensor under (f) compression and (g) bending. Reproduced from ref 190. Copyright 2020 American Chemical Society.

nanomaterials usually showed excellent selectivity to their target gas. Furthermore, the depletion layer of a p−n heterojunction resulting from a combination of MONs and carbon materials also induced a remarkable increase in sensor responses, as shown in Figure 11a. WO_3 NP modification improved the sensitivity, the selectivity to NO_2, and the CNT-based gas sensor recovery property, as shown in Figure 11b,c.[209−211] Among carbon nanomaterials, rGO is most frequently combined with MONs for detecting gases. Li et al. explained that the high selectivity of their rGO/mesoporous ZnO NS-based flexible NO_2 sensor is due to the high NO_2 absorption interaction on the surface of the sensing sites.[192] Additionally, rGO-based NO_2 gas sensors modified with ZnO NPs[197] and ZnO NRs[127] exhibited great selectivity and improved sensitivity at RT. The synergetics of rGO and ZnO NRs demonstrated ultrahigh sensitivity to NO_2 (40 ppb), fast res/rec time, and high reliability in humid conditions. Moon et al. fabricated a flexible/stretchable NO_2 sensor at RT of rGO as an electron transport player and vertically grown ZnO NRs as an active player on a 3D micropatterned PDMS substrate, as displayed in Figure 11d.[127] The synergetics of

rGO and ZnO NRs demonstrated ultrahigh sensitivity to NO_2 (40 ppb), fast res/rec time, and high reliability in humid conditions. You et al. reduced the rGO of an In_2O_3@graphene oxide (GO) film via DLW, as displayed in Figure 11e. Therefore, the photoreduction resulted in the removal of most of the oxygen-containing groups on the basal planes and edges of graphene.[133] As a result, a highly porous structure due to the elimination of oxygen groups, improving the sensing performance by the provision of diffusion path and active sites, was formed. Accordingly, the In_2O_3@rGO showed linear sensing characteristics and great selectivity to NO_2 gas at RT. Indeed, rGO and SnO_2 NPs were employed to enhance the sensitivity of the PVDF-based H_2 gas sensor.[99] Graphene was also used for MON-based flexible gas sensors. ZnO NRs grown on graphene exhibited a highly selective response toward CO gas and fast res/rec times at RT.[212]

The ZnO NPs/rGO nanocomposite film is also a certified material for flexible UV sensors due to the excellent electronic conductivity of rGO which hinder recombination of the electron−hole pair as shown in Figure 12a,b.[182] Wu et al. extended the humidity-sensitive electrochemical response of
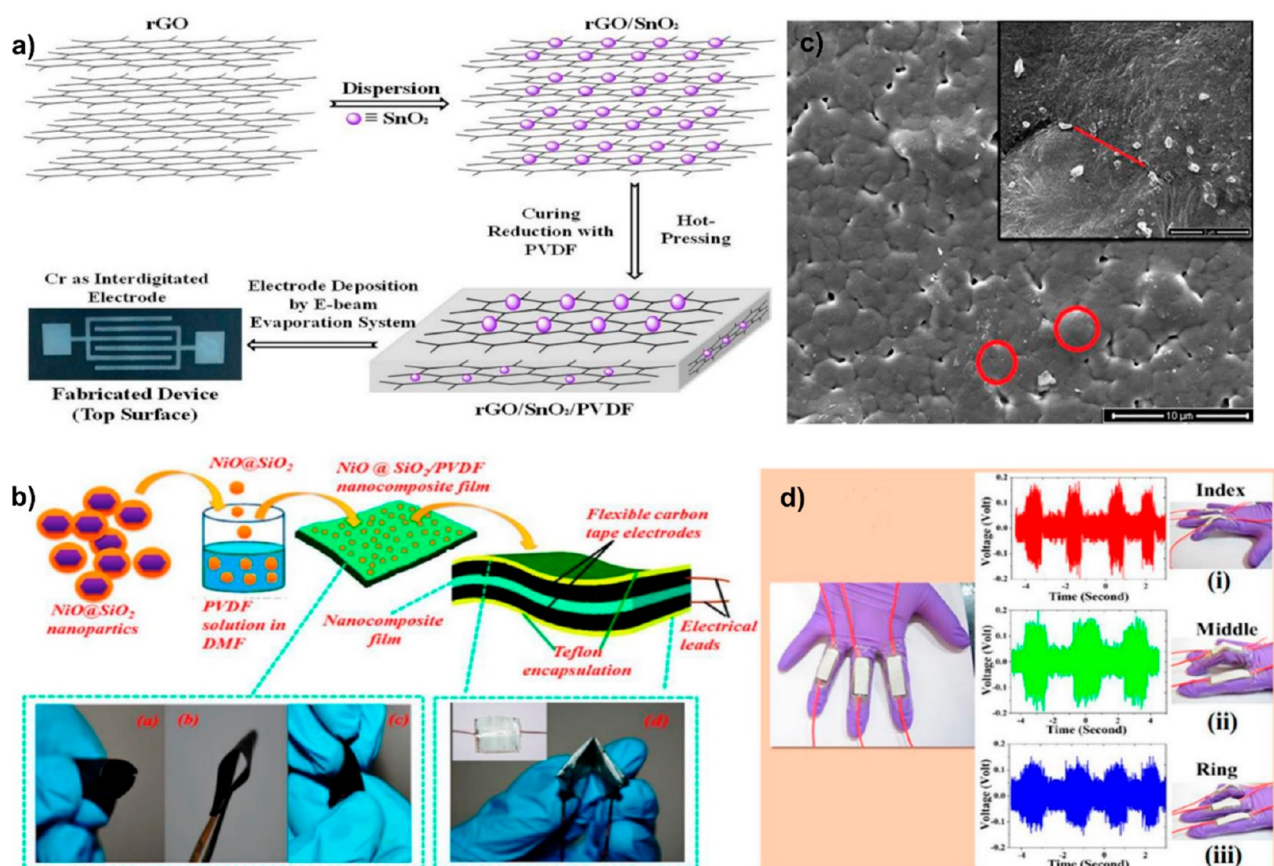
Figure 13. (a) Preparation of rGO/SnO$_2$/PVDF complex hybrid-based H$_2$ sensor. Adapted from ref 99 under a Creative Commons Attribution 4.0 International License. (b) Preparation of PNG NiO@SiO$_2$/PVDF-based mechanosensor. (c) FESEM images of PNG (15% NiO@SiO$_2$ NPs). (d) E-skin sensors attached on index, middle, and ring fingers (right hand). Voltage generated by a stretching−bending motion of (i) index, (ii) middle, and (iii) ring fingers. Reproduced from ref 191. Copyright 2018 American Chemical Society.

ZnO to the surface acoustic wave (SAW) humidity sensor with graphene quantum dots (GQDs) and ZnO NWs on ZnO/ultrathin flexible glass.[171] The humidity sensor showed a great sensitivity of 20.16 kHZ/% RH, stability, and repeatability due to the abundant hydrophilic functional groups of GQDs, the large surface-to-volume ratio of ZnO NWs, and the p−n heterojunction between graphene and ZnO (Figure 12c,d). Moreover, attributed to ultrathin structure, the sensor exhibited moderate bending performance, despite being composed of glass that is more advantageous than polymer in SAW devices due to its rigidity. The water molecule adsorbing ability of CeO$_2$ NPs also enhanced the humidity sensitivity of the CeO$_2$/g-C$_3$N$_4$ nanocomposite, as shown in Figure 12e.[172] Since the adsorbed water molecules constructed the intermediate dielectric layer between CeO$_2$ and g-C$_3$N$_4$, the capacitance of the composite increased with the increase in humidity.

A flexible enzyme-free electrocatalytic dopamine sensor based on hybridization of metal-oxide NPs and carbon materials was studied.[166,167] α-Fe$_2$O$_3$ NPs hydrothermally grown on carbon cloth showed superior electrochemical behavior because a large number of negatively charged −OH groups on Fe$_2$O$_3$ and a positively charged −NH$_2$ group of a dopamine molecule can construct hydrogen bonding that results in electron transfer.[166] In addition, graphene-anchored Cu$_2$O was fabricated as a flexible electrochemical dopamine sensor by recycling waste electronic cables. The sensor detected mercury electrochemically as well.[167] A piezoelectric

mechanical sensor was established by vertically growing ZnO NWs on the transferred graphene on PET.[190] The vertically aligned (0001) orientation single-crystalline ZnO NWs provide optimal piezoelectric behavior under mechanical deformation, resulting in high strain sensitivity and response speed. Figure 12f,g shows the schematics and piezoelectric responses of the vertically grown ZnO NW mechanical sensor under different mechanical deformations.

5.2.3. Complex Hybridization. Much effort has been put into studying the properties of MONs, polymers, and carbon materials in the field of sensors. Ternary hybridization is generated to inspire flexible, wearable, stretchable sensors with a superb response, rapid res/rec times, reduced energy dissipation, miniaturization, and possible integration with another modern technology device due to the synergistic effects. Moreover, diverse and flexible materials are capable of acting as a protective membrane. Punetha et al. pioneered a flexible H$_2$ sensor based on the hybridization of 0.9(PVDF)/0.1[(SnO$_2$)$_a$rGO$_{(1-a)}$] with various ratios via a hot press method, as observed in Figure 13a.[99] Crystallinity morphology has been observed in the enhancement of sensing efficiency. The hybrid-based sensor of 0.9(PVDF)/0.1-[(SnO$_2$)$_{0.75}$rGO$_{0.25}$] displays a superb sensitivity value of 49.2−71.4% for 100−1000 ppm of H$_2$ with an increasing response interval. Additionally, PdO-NP-decorated sensors are known for good sensing characteristics for CH$_3$COCH$_3$[213] and H$_2$.[108] The progression of effective human actions-based energy conversion and e-skin mechanosensing capability are
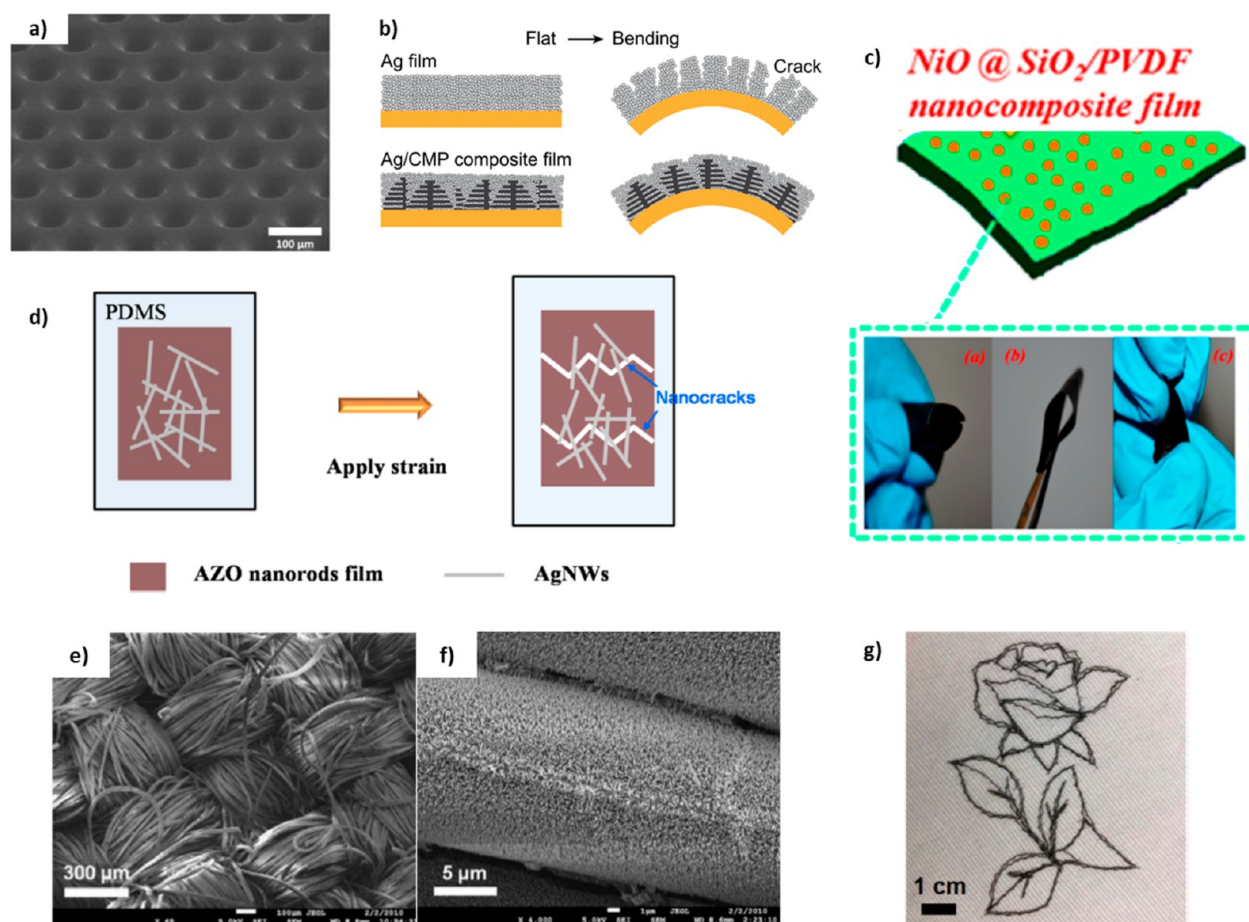
Figure 14. (a) FE-SEM image of 3D micropatterned PDMS substrate. Reprinted from ref 127. Copyright 2021, with permission from Elsevier. (b) Schematics of comparing the flexibility of the pure Ag electrode and the Ag electrode embedded in a CMP structure. Reprinted from ref 187, with the permission of AIP Publishing. (c) Schematic of MONs/polymer composite and photo of its mechanical deformation. Reproduced from ref 191. Copyright 2018 American Chemical Society. (d) Schematic of the electrical connection induced by Ag NW percolation under applied strain. Reproduced from ref 195. Copyright 2019 American Chemical Society. SEM images of (e) cotton fabric substrate and (f) ZnO-NR-coated cotton fabric substrate. Reprinted from ref 150. Copyright 2010, with permission from Elsevier. (g) Optical image of the woven pattern of rGO/ZnO carbon thread fiber onto the fabric. Reproduced from ref 192. Copyright 2019 American Chemical Society.

promising for self-powered miniaturized and wearable devices. Dutta et al. constituted a PNG mechanosensor based on a SiO_2-grafted NiO (NiO@SiO_2)/PVDF hybrid with various loading amounts of NiO@SiO_2 NPs as described in Figure 13b.[191] The separate and uniform distribution of NiO@SiO_2 NPs (Figure 13c) in a PVDF membrane boosts the piezoelectric and dielectric characteristics of the complex hybridization. The hybridized PNG mechanosensor with a loading amount of 15% NiO@SiO_2 NPs produced the highest electrical productivity generated by a slight finger touch in Figure 13d, capably running 85 LEDs simultaneously.

The MON electrochemical sensors detected the catalytic reduction of hydrogen peroxide (H_2O_2) caused by Pt and rGO. Pt is a well-known catalyst for the decomposition of H_2O_2 oxidation, but Leonardi et al. assumed rGO also behaves as a catalyst for H_2O_2 reduction.[169] They fabricated a Pt-TiO_2/rGO nanocomposite to detect H_2O_2. The composite demonstrated better sensitivity than the pure rGO, TiO_2/rGO nanocomposite, and Pt/rGO nanocomposite. Moreover, the Pt-MnO_2 nanostructure on freestanding rGO paper was developed to detect H_2O_2 secretion of living cells in real time.[170] The nonenzymatic Pt-MnO_2/rGO sensor showed a fast response, long-term stability, reproducibility, and endur-ance to physical deformation comparing with conventional enzymatic biosensors.

Dopamine also can be detected by an IZO-based EGFET modified with 4-carboxy phenylboronic acid without electrocatalytic activity. A dopamine molecule was positively charged and attracted more electrons from the FET channel since it was combined with the carboxyl ester group of the functionalizing group on the surface of the extended gate electrode. Therefore, the concentration of dopamine determines how much the transfer curve shifts.[159] A cortisol-antibody modified ZnO-NR-based cortisol sensor was developed as well. Since the immune complex consisted of the antibody and the cortisol hinders electron transfer between the redox probe and the ZnO electrode, a higher concentration of cortisol induced a further decrease of an electrochemical current response of the electrode.[168]

Usually, the range of wavelength of the target lights was in the UV range due to the wide band gaps of the metal oxides, but some metal oxides, including Cu_2O, have a smaller band gap (1.9−2.2 eV) and can be excited by UV−vis spectral light. A flexible photodetector with a broadband range (365−625 nm) was fabricated based on a Cu_2O/ZnO hybrid nanofilm.[180] The hybrid nanofilms consisting of an ITO/Cu_2O/ZnO/

SWCNT core−shell nanostructure were fabricated by subsequent deposition of ZnO, Cu$_2$O, and ITO layers on SWCNTs.

6. STRATEGIES TO ENHANCE FLEXIBILITY AND STRETCHABILITY

The achievement of flexibility and stretchability, which facilitate mechanical deformation such as bending, twisting, and stretching, is one of the most critical tasks in fabricating flexible/wearable sensors. Therefore, diverse strategies have been employed to acquire flexibility and stretchability in the fabrication of MON-based sensors. The thin-film structure is the basic strategy that most sensors adapt. Since the mechanical strain (S) is determined by the substrate thickness (d) and the bending radius (r) as $S = d/2r$, thinner film structures guarantee reduced mechanical strain in the bending environment. However, there is a limitation that a thin-film structure cannot tolerate strain greater than 1%, which is applied in significant bending and twisting situations.[214] In order to overcome the limitation, several strategies including the deposition of thin films on porous substrates,[127] embedding in mechanically stable materials or structures,[187,213] construction of nanocomposite with intrinsically flexible polymers,[151,191,198] fabrication in textiles and fibers,[29,105,150,165,166,168,179,188,192] and percolation with a network of 1D nanomaterials[95,108,180,183,195,211] are introduced to enhance the flexibility and stretchability of flexible/wearable MON-based sensors.

Moon et al. produced stretchability up to a strain of 20% to ZnO NRs grown on rGO by combining them with a 3D micropatterned porous PDMS substrate.[127] The micropatterned bumps and valleys, which are 6 μm scale on the substrate, as shown in Figure 14a, effectively absorbed mechanical stress applying to the sensor under multidirectional stretching. Also, a Ni/Au mesh heater of a PdO-Co$_3$O$_4$ NCs-based NO$_2$ gas sensor was embedded in the colorless polyimide substrate to obtain thermal and mechanical stability.[213] As a result, the Ni/Au mesh heater operated well for cyclic bending of 1700 cycles at 100 °C. Nakajima et al. developed a highly stable flexible thermistor based on spinel Mn−Co−Ni oxide films on a silver/carbon micro-pinecone (CMP) array composite electrode.[187] The highly stable flexibility of the silver electrode used in the thermistor was achieved by embedding it in the CMP structure, as shown in Figure 14b.

The fabrication of nanocomposites with MONs and polymers such as PVDF, PANI, and PVA has been widely used to provide flexibility to MONs, as shown in Figure 14c. Regardless of the flexibility of MONs, the surrounding polymers allow the composite to endure mechanical deformation without critical damage. When MONs were used as the primary sensing materials, the role of the polymers in nanocomposites was mainly to anchor MONs to prevent mechanical damage such as cracking on thin films. In that case, an adequate concentration of MONs to construct percolation networks of MONs which guarantee electrical connection was necessary.[151] In addition, MONs were also applied as kinds of additives to enhance the performance of electrically functional polymers, including PVDF and PANI.[191,198]

Percolation networks of 1D nanomaterials, including ZnO NRs/Ag NWs bilayers,[195] Zn$_2$SnO$_4$ NWs,[183] CNTs,[180,211] SnO2 hollow NTs,[95] and an electrospun polymer with ZnO NPs[108] were also attractive structures that can achieve the flexibility and stretchability of MON-based sensors due to their weblike structures.[95,108,180,183,195,211] For example, Namgung et al. fabricated ZnO NRs/Ag NW bilayers on PDMS substrates to detect NO$_2$.[195] Percolation networks of Ag NWs electrically connected the nanocracked ZnO NRs structures under the highly stretched condition as shown in Figure 14d and enhanced the stretchability up to 20% of strain.

Several studies have fabricated MON-based sensors in the form of textiles and fibers. These strategies are easily applied as wearable applications due to clothlike structures. Indeed, direct growth of nanomaterials including CuO NPs,[165] ZnO NPs,[105] ZnO NRs,[150,188] WO$_3$ NPs,[29] and Fe$_2$O$_3$ NPs[166] on already weaved fabrics such as cotton fabrics,[105,150,165] carbon cloth,[29,166] CNT coated PET textiles[188] is a common method to fabricate the sensors in the textile form as shown in Figure 14e,f. Compared with other fabrics, carbon cloth can be used as the conductive layer. Also, various groups have demonstrated MON-based sensors in the fiber structure. ZnO NRs were directly grown on diverse fibers, including Kevlar fiber,[179] conductive carbon yarn,[168] and elastic cotton thread[192] to be used as UV, cortisol, and gas sensors, respectively. These kinds of sensors can be woven into fabric with a desirable pattern, as shown in Figure 14g.

7. CONCLUSION

In this Review, we have discussed the recent progress of flexible/wearable MON-based sensors. Techniques related to sensors have been widely examined, from the diverse MON synthesis techniques to applications of MON-based sensors. Synthesis techniques and semiconducting and sensing characteristics of diverse MONs were introduced, including CuO, SnO$_2$, ZnO, In$_2$O$_3$, and WO$_3$, which were synthesized in diverse nanostructures such as NPs, NWs, nanoplatelets, NCs, NTs, and NFs. Moreover, synthetic strategies to enhance sensing efficiency were explored, including metal doping, noble metal decorating, and hybridization with inorganic materials and organic materials (CPs and carbon materials). In addition, we explained the concept of crucial sensor parameters, namely, sensitivity, selectivity, res/rec time, and LOD, and characterization techniques for sensors. In addition, strategies to improve flexibility and stretchability were also explored. Finally, we also described sensing and performance enhancing mechanisms and the overview of diverse kinds of flexible/wearable sensors such as gas, pH level, biomaterials, humidity, temperature, photo, mechanical, and health-monitoring sensors based on MONs.

Moreover, there are still challenges for flexible/wearable MON-based sensors. First, it is still difficult to clearly distinguish signals from multiple stimuli. Because of the highly active semiconducting behavior of MONs, they were able to be utilized as sensing materials responsive to various types of stimulations including gases, electrochemical redox reactions with various ions, and light. Still, it also meant that they could respond indiscriminately to undesirable stimulations. Notably, several studies argue the development of multifunctional flexible MONs sensors, but only a few proved successful response recognition depending on different stimulations. To overcome the limitation, several approaches including hybridizing with and doping of other materials have been tried, but convergence with other rapidly growing fields such as deep learning also could be a promising approach in the future.

Also, in the literature, there are few publications reporting thermistors and mechanical sensors based on MONs

compared with gas sensors, electrochemical sensors, and photodetectors, even though MON-based rigid thermistors and mechanical sensors have been studied widely. It might mean that MON-based flexible sensors are more suitable for detecting redox reactions and photoelectric phenomena, but further progress on MON-based thermistors and mechanical sensors would facilitate promising MONs applications.

Furthermore, MON-based flexible/wearable sensors also need to be expanded in terms of materials. In the case of conventional rigid MON-based sensors, a wider variety of metal oxides including bismuth oxide, niobium oxide, and zirconium oxide have been studied in-depth compared to flexible MON-based sensors. Therefore, utilizing such kinds of MONs might suggest another perspective for flexible/wearable MON-based sensors.

Wearable applications of MON-based sensors have been studied sufficiently in the last 3 years. However, most of them were primitive wearables and lacked textile-based sensors, which can be integrated into clothes, and ultrathin epidermal sensors, which can be conformally attached to the skin. Also, most of the demonstrated wearable systems demanded bulky and rigid modules and showed only simple usage of collected data. We hope that convergence with other advanced wearable electronic technologies would allow MON-based flexible sensors to compose advanced MON-based wearable systems.

Despite the limitations mentioned, MONs are still attractive and promising materials for future applications due to their potential for excellent semiconducting properties, high surface-to-volume ratio, synergetic effects with other materials, and achievement of flexibility and stretchability. Also, further advancement overcoming limitations of MON-based flexible/wearable sensors, as mentioned above, would lead MONs to be a more attractive candidate material for future electronics. Also, MON-based flexible/wearable sensors would participate in fascinating multidisciplinary research such as bioelectronics, VR/AR systems, wearable health-monitoring systems, and multifunctional sensory systems, if they converge with cutting edge studies in other fields such as data processing via deep learning, degradable electronics, soft robotics, and epidermal electronics.

■ AUTHOR INFORMATION

Corresponding Authors

Seung Hwan Ko − *Applied Nano and Thermal Science Lab, Department of Mechanical Engineering, Seoul National University, Gwanak-gu, Seoul 08826, Korea; Institute of Advanced Machinery and Design (SNU-IAMD), Seoul National University, Gwanak-gu, Seoul 08826, Korea; Institute of Engineering Research, Seoul National University, Gwanak-gu, Seoul 08826, Republic of Korea;* ⦿ orcid.org/0000-0002-7477-0820; Email: maxko@snu.ac.kr

Daeho Lee − *Laser and Thermal Engineering Lab, Department of Mechanical Engineering, Gachon University, Seongnam 13120, Korea;* ⦿ orcid.org/0000-0002-8119-9677; Email: dhl@gachon.ac.kr

Authors

Yeosang Yoon − *Applied Nano and Thermal Science Lab, Department of Mechanical Engineering, Seoul National University, Gwanak-gu, Seoul 08826, Korea*

Phuoc Loc Truong − *Laser and Thermal Engineering Lab, Department of Mechanical Engineering, Gachon University, Seongnam 13120, Korea*

Complete contact information is available at:
https://pubs.acs.org/10.1021/acsnanoscienceau.1c00029

Author Contributions

†Y.Y. and P.L.T. contributed equally to this work.

Notes

The authors declare no competing financial interest.

■ REFERENCES

(1) Wen, N.; Zhang, L.; Jiang, D.; Wu, Z.; Li, B.; Sun, C.; Guo, Z. Emerging flexible sensors based on nanomaterials: recent status and applications. *J. Mater. Chem. A* **2020**, *8* (48), 25499−25527.

(2) Kanoun, O.; Bouhamed, A.; Ramalingame, R.; Bautista-Quijano, J. R.; Rajendran, D.; Al-Hamry, A. Review on Conductive Polymer/CNTs Nanocomposites Based Flexible and Stretchable Strain and Pressure Sensors. *Sensors* **2021**, *21* (2), 341.

(3) Arman Kuzubasoglu, B.; Kursun Bahadir, S. Flexible temperature sensors: A review. *Sens. Actuators, A* **2020**, *315*, 112282.

(4) Gu, Y.; Zhang, T.; Chen, H.; Wang, F.; Pu, Y.; Gao, C.; Li, S. Mini Review on Flexible and Wearable Electronics for Monitoring Human Health Information. *Nanoscale Res. Lett.* **2019**, *14* (1), 263.

(5) Mahmood, A.; Hu, J.-Y.; Xiao, B.; Tang, A.; Wang, X.; Zhou, E. Recent progress in porphyrin-based materials for organic solar cells. *J. Mater. Chem. A* **2018**, *6* (35), 16769−16797.

(6) Wu, X.; Zhou, Z.; Wang, Y.; Li, J. Syntheses of Silver Nanowires Ink and Printable Flexible Transparent Conductive Film: A Review. *Coatings* **2020**, *10* (9), 865.

(7) Wu, N.; Wan, S.; Su, S.; Huang, H.; Dou, G.; Sun, L. Electrode materials for brain−machine interface: A review. *InfoMat* **2021**, 1−21.

(8) Gao, M.; Li, L.; Song, Y. Inkjet printing wearable electronic devices. *J. Mater. Chem. C* **2017**, *5* (12), 2971−2993.

(9) Chortos, A.; Liu, J.; Bao, Z. Pursuing prosthetic electronic skin. *Nat. Mater.* **2016**, *15* (9), 937−950.

(10) Sekitani, T.; Zschieschang, U.; Klauk, H.; Someya, T. Flexible organic transistors and circuits with extreme bending stability. *Nat. Mater.* **2010**, *9* (12), 1015−1022.

(11) Lahcen, A. A.; Rauf, S.; Beduk, T.; Durmus, C.; Aljedaibi, A.; Timur, S.; Alshareef, H. N.; Amine, A.; Wolfbeis, O. S.; Salama, K. N. Electrochemical sensors and biosensors using laser-derived graphene: A comprehensive review. *Biosens. Bioelectron.* **2020**, *168*, 112565.

(12) Xie, J.; Chen, Q.; Shen, H.; Li, G. Review—Wearable Graphene Devices for Sensing. *J. Electrochem. Soc.* **2020**, *167* (3), 037541.

(13) Yan, T.; Wu, Y.; Yi, W.; Pan, Z. Recent progress on fabrication of carbon nanotube-based flexible conductive networks for resistive-type strain sensors. *Sens. Actuators, A* **2021**, *327*, 112755.

(14) Ravi, S. K.; Paul, N.; Suresh, L.; Salim, A. T.; Wu, T.; Wu, Z.; Jones, M. R.; Tan, S. C. Bio-photocapacitive tactile sensors as a touch-to-audio braille reader and solar capacitor. *Mater. Horiz.* **2020**, *7* (3), 866−876.

(15) Paul, N.; Suresh, L.; Vaghasiya, J. V.; Yang, L.; Zhang, Y.; Nandakumar, D. K.; Jones, M. R.; Tan, S. C. Self-powered all weather sensory systems powered by Rhodobacter sphaeroides protein solar cells. *Biosens. Bioelectron.* **2020**, *165*, 112423.

(16) Sharma, S.; Sudhakara, P.; Omran, A. A. B.; Singh, J.; Ilyas, R. A. Recent Trends and Developments in Conducting Polymer Nanocomposites for Multifunctional Applications. *Polymers* **2021**, *13* (17), 2898.

(17) Naveen, M. H.; Gurudatt, N. G.; Shim, Y.-B. Applications of conducting polymer composites to electrochemical sensors: A review. *Appl. Mater. Today* **2017**, *9*, 419−433.

(18) Shrivas, K.; Ghosale, A.; Bajpai, P. K.; Kant, T.; Dewangan, K.; Shankar, R. Advances in flexible electronics and electrochemical sensors using conducting nanomaterials: A review. *Microchem. J.* **2020**, *156*, 104944.

(19) Park, J. W.; Kang, B. H.; Kim, H. J. A Review of Low-Temperature Solution-Processed Metal Oxide Thin-Film Transistors for Flexible Electronics. *Adv. Funct. Mater.* **2020**, *30* (20), 1904632.

(20) Vorokhta, M.; Khalakhan, I.; Vondráček, M.; Tomeček, D.; Vorokhta, M.; Marešová, E.; Nováková, J.; Vlček, J.; Fitl, P.; Novotný, M.; Hozák, P.; Lančok, J.; Vrňata, M.; Matolínová, I.; Matolín, V. Investigation of gas sensing mechanism of SnO2 based chemiresistor using near ambient pressure XPS. *Surf. Sci.* **2018**, *677*, 284−290.

(21) Mavrou, G.; Galata, S.; Tsipas, P.; Sotiropoulos, A.; Panayiotatos, Y.; Dimoulas, A.; Evangelou, E. K.; Seo, J. W.; Dieker, C. Electrical properties of La2O3 and HfO2/La2O3 gate dielectrics for germanium metal-oxide-semiconductor devices. *J. Appl. Phys.* **2008**, *103* (1), 014506.

(22) Ashik, U. P. M.; Kudo, S.; Hayashi, J.-i. An Overview of Metal Oxide Nanostructures. In *Synthesis of Inorganic Nanomaterials*; Mohan Bhagyaraj, S., Oluwafemi, O. S., Kalarikkal, N., Thomas, S., Eds.; Woodhead Publishing: 2018; Chapter 2, pp 19−57.

(23) Mosadegh Sedghi, S.; Mortazavi, Y.; Khodadadi, A. Low temperature CO and CH4 dual selective gas sensor using SnO2 quantum dots prepared by sonochemical method. *Sens. Actuators, B* **2010**, *145* (1), 7−12.

(24) Tonezzer, M.; Lacerda, R. G. Zinc oxide nanowires on carbon microfiber as flexible gas sensor. *Phys. E* **2012**, *44* (6), 1098−1102.

(25) Xue, X.; Nie, Y.; He, B.; Xing, L.; Zhang, Y.; Wang, Z. L. Surface free-carrier screening effect on the output of a ZnO nanowire nanogenerator and its potential as a self-powered active gas sensor. *Nanotechnology* **2013**, *24* (22), 225501.

(26) Rim, Y. S.; Bae, S.-H.; Chen, H.; Yang, J. L.; Kim, J.; Andrews, A. M.; Weiss, P. S.; Yang, Y.; Tseng, H.-R. Printable Ultrathin Metal Oxide Semiconductor-Based Conformal Biosensors. *ACS Nano* **2015**, *9* (12), 12174−12181.

(27) Choi, S.-J.; Lee, I.; Jang, B.-H.; Youn, D.-Y.; Ryu, W.-H.; Park, C. O.; Kim, I.-D. Selective Diagnosis of Diabetes Using Pt-Functionalized WO3 Hemitube Networks As a Sensing Layer of Acetone in Exhaled Breath. *Anal. Chem.* **2013**, *85* (3), 1792−1796.

(28) Manjakkal, L.; Sakthivel, B.; Gopalakrishnan, N.; Dahiya, R. Printed flexible electrochemical pH sensors based on CuO nanorods. *Sens. Actuators, B* **2018**, *263*, 50−58.

(29) Jamal, M.; Razeeb, K. M.; Shao, H.; Islam, J.; Akhter, I.; Furukawa, H.; Khosla, A. Development of Tungsten Oxide Nanoparticle Modified Carbon Fibre Cloth as Flexible pH Sensor. *Sci. Rep.* **2019**, *9* (1), 4659.

(30) Li, Z.; Huang, Y.; Zhang, S.; Chen, W.; Kuang, Z.; Ao, D.; Liu, W.; Fu, Y. A fast response & recovery H2S gas sensor based on α-Fe2O3 nanoparticles with ppb level detection limit. *J. Hazard. Mater.* **2015**, *300*, 167−174.

(31) Hu, J.; Sun, Y.; Xue, Y.; Zhang, M.; Li, P.; Lian, K.; Zhuiykov, S.; Zhang, W.; Chen, Y. Highly sensitive and ultra-fast gas sensor based on CeO2-loaded In2O3 hollow spheres for ppb-level hydrogen detection. *Sens. Actuators, B* **2018**, *257*, 124−135.

(32) Han, D.; Zhai, L.; Gu, F.; Wang, Z. Highly sensitive NO2 gas sensor of ppb-level detection based on In2O3 nanobricks at low temperature. *Sens. Actuators, B* **2018**, *262*, 655−663.

(33) Rim, Y. S.; Bae, S.-H.; Chen, H.; De Marco, N.; Yang, Y. Recent Progress in Materials and Devices toward Printable and Flexible Sensors. *Adv. Mater.* **2016**, *28* (22), 4415−4440.

(34) Chung, C.-H.; Song, T.-B.; Bob, B.; Zhu, R.; Yang, Y. Solution-processed flexible transparent conductors composed of silver nanowire networks embedded in indium tin oxide nanoparticle matrices. *Nano Res.* **2012**, *5* (11), 805−814.

(35) Hou, L.; Zhang, C.; Li, L.; Du, C.; Li, X.; Kang, X.-F.; Chen, W. CO gas sensors based on p-type CuO nanotubes and CuO nanocubes: Morphology and surface structure effects on the sensing performance. *Talanta* **2018**, *188*, 41−49.

(36) Oosthuizen, D. N.; Motaung, D. E.; Swart, H. C. Selective detection of CO at room temperature with CuO nanoplatelets sensor for indoor air quality monitoring manifested by crystallinity. *Appl. Surf. Sci.* **2019**, *466*, 545−553.

(37) Kim, S.-Y.; Kim, J.; Cheong, W. H.; Lee, I. J.; Lee, H.; Im, H.-G.; Kong, H.; Bae, B.-S.; Park, J.-U. Alcohol gas sensors capable of wireless detection using In2O3/Pt nanoparticles and Ag nanowires. *Sens. Actuators, B* **2018**, *259*, 825−832.

(38) Korotchenkov, G. S.; Dmitriev, S. V.; Brynzari, V. I. Processes development for low cost and low power consuming SnO2 thin film gas sensors (TFGS). *Sens. Actuators, B* **1999**, *54* (3), 202−209.

(39) Brunet, E.; Maier, T.; Mutinati, G. C.; Steinhauer, S.; Köck, A.; Gspan, C.; Grogger, W. Comparison of the gas sensing performance of SnO2 thin film and SnO2 nanowire sensors. *Sens. Actuators, B* **2012**, *165* (1), 110−118.

(40) Woo, H.-S.; Kwak, C.-H.; Chung, J.-H.; Lee, J.-H. Highly selective and sensitive xylene sensors using Ni-doped branched ZnO nanowire networks. *Sens. Actuators, B* **2015**, *216*, 358−366.

(41) Bing, Y.; Liu, C.; Qiao, L.; Zeng, Y.; Yu, S.; Liang, Z.; Liu, J.; Luo, J.; Zheng, W. Multistep synthesis of non-spherical SnO2@SnO2 yolk-shell cuboctahedra with nanoparticle-assembled porous structure for toluene detection. *Sens. Actuators, B* **2016**, *231*, 365−375.

(42) Kim, H. W.; Na, H. G.; Kwon, Y. J.; Kang, S. Y.; Choi, M. S.; Bang, J. H.; Wu, P.; Kim, S. S. Microwave-Assisted Synthesis of Graphene−SnO2 Nanocomposites and Their Applications in Gas Sensors. *ACS Appl. Mater. Interfaces* **2017**, *9* (37), 31667−31682.

(43) Xue, D.; Wang, P.; Zhang, Z.; Wang, Y. Enhanced methane sensing property of flower-like SnO2 doped by Pt nanoparticles: A combined experimental and first-principle study. *Sens. Actuators, B* **2019**, *296*, 126710.

(44) Shewale, P. S.; Lee, S. H.; Yu, Y. S. UV sensitive pulsed laser deposited ZnO thin films: Influence of growth temperature. *J. Alloys Compd.* **2018**, *744*, 849−858.

(45) Rodrigues, J.; Mata, D.; Pimentel, A.; Nunes, D.; Martins, R.; Fortunato, E.; Neves, A. J.; Monteiro, T.; Costa, F. M. One-step synthesis of ZnO decorated CNT buckypaper composites and their optical and electrical properties. *Mater. Sci. Eng., B* **2015**, *195*, 38−44.

(46) Lu, M.-L.; Weng, T.-M.; Chen, J.-Y.; Chen, Y.-F. Ultrahigh-gain single SnO2 nanowire photodetectors made with ferromagnetic nickel electrodes. *NPG Asia Mater.* **2012**, *4* (9), e26−e26.

(47) Sharma, P.; Sawyer, S. A high responsivity SnO2 hollow nanospheres based ultraviolet photodetector. *2016 Lester Eastman Conference (LEC)*, August 2−4 2016; 2016; pp 46−49.

(48) Yu, X.; Zhao, Z.; Zhang, J.; Guo, W.; Qiu, J.; Li, D.; Li, Z.; Mou, X.; Li, L.; Li, A.; Liu, H. Rutile Nanorod/Anatase Nanowire Junction Array as Both Sensor and Power Supplier for High-Performance, Self-Powered, Wireless UV Photodetector. *Small* **2016**, *12* (20), 2759−2767.

(49) Cook, B.; Liu, Q.; Butler, J.; Smith, K.; Shi, K.; Ewing, D.; Casper, M.; Stramel, A.; Elliot, A.; Wu, J. Heat-Assisted Inkjet Printing of Tungsten Oxide for High-Performance Ultraviolet Photodetectors. *ACS Appl. Mater. Interfaces* **2018**, *10* (1), 873−879.

(50) Scuderi, V.; Amiard, G.; Boninelli, S.; Scalese, S.; Miritello, M.; Sberna, P. M.; Impellizzeri, G.; Privitera, V. Photocatalytic activity of CuO and Cu2O nanowires. *Mater. Sci. Semicond. Process.* **2016**, *42*, 89−93.

(51) Wang, J. X.; Sun, X. W.; Wei, A.; Lei, Y.; Cai, X. P.; Li, C. M.; Dong, Z. L. Zinc oxide nanocomb biosensor for glucose detection. *Appl. Phys. Lett.* **2006**, *88* (23), 233106.

(52) Bhat, S. S.; Qurashi, A.; Khanday, F. A. ZnO nanostructures based biosensors for cancer and infectious disease applications: Perspectives, prospects and promises. *TrAC, Trends Anal. Chem.* **2017**, *86*, 1−13.

(53) Haider, A. J.; Jasim Mohammed, A.; Shaker, S. S.; Yahya, K. Z.; Haider, M. J. Sensing Characteristics of Nanostructured SnO2 Thin Films as Glucose Sensor. *Energy Procedia* **2017**, *119*, 473−481.

(54) Jang, H. D.; Kim, S. K.; Chang, H.; Roh, K.-M.; Choi, J.-W.; Huang, J. A glucose biosensor based on TiO2−Graphene composite. *Biosens. Bioelectron.* **2012**, *38* (1), 184−188.

(55) Qurashi, A.; Rather, J. A.; Yamazaki, T.; Sohail, M.; De Wael, K.; Merzougui, B.; Hakeem, A. S. Swift electrochemical detection of paraben an endocrine disruptor by In2O3 nanobricks. *Sens. Actuators, B* **2015**, *221*, 167−171.

(56) Deng, Z.; Gong, Y.; Luo, Y.; Tian, Y. WO3 nanostructures facilitate electron transfer of enzyme: Application to detection of H2O2 with high selectivity. *Biosens. Bioelectron.* **2009**, *24* (8), 2465−2469.

(57) Cargnello, M.; Delgado Jaén, J. J.; Hernández Garrido, J. C.; Bakhmutsky, K.; Montini, T.; Calvino Gámez, J. J.; Gorte, R. J.; Fornasiero, P. Exceptional activity for methane combustion over modular Pd@CeO2 subunits on functionalized Al2O3. *Science* **2012**, *337*, 713−717.

(58) Hsueh, H. T.; Hsueh, T. J.; Chang, S. J.; Hung, F. Y.; Tsai, T. Y.; Weng, W. Y.; Hsu, C. L.; Dai, B. T. CuO nanowire-based humidity sensors prepared on glass substrate. *Sens. Actuators, B* **2011**, *156*, 906−911.

(59) Karimov, K. S.; Saleem, M.; Karieva, Z. M.; Mateen, A.; Chani, M. T. S.; Zafar, Q. Humidity sensing properties of Cu 2O-PEPC nanocomposite films. *J. Semicond.* **2012**, *33*, 073001.

(60) Zou, Z.; Qiu, Y.; Xu, J.; Guo, P.; Luo, Y. High performance photoelectric responses of nanocrystalline WO3 film to humidity irradiated by UV light. *J. Mater. Sci.: Mater. Electron.* **2017**, *28*, 15618−15624.

(61) Dong, Y. F.; Li, L. Y.; Jiang, W. F.; Wang, H. Y.; Li, X. J. Capacitive humidity-sensing properties of electron-beam-evaporated nanophased WO3 film on silicon nanoporous pillar array. *Phys. E* **2009**, *41*, 711−714.

(62) Parthibavarman, M.; Hariharan, V.; Sekar, C. High-sensitivity humidity sensor based on SnO2 nanoparticles synthesized by microwave irradiation method. *Mater. Sci. Eng., C* **2011**, *31*, 840−844.

(63) Li, W.; Liu, J.; Ding, C.; Bai, G.; Xu, J.; Ren, Q.; Li, J. Fabrication of ordered SnO2 nanostructures with enhanced humidity sensing performance. *Sensors* **2017**, *17*, 2392.

(64) Ghanem, S.; Telia, A.; Boukaous, C.; Aida, M. S. Humidity sensor characteristics based on ZnO nanostructure grown by sol-gel method. *Int. J. Nanotechnol.* **2015**, *12*, 697−707.

(65) Zhu, D.; Hu, T.; Zhao, Y.; Zang, W.; Xing, L.; Xue, X. High-performance self-powered/active humidity sensing of Fe-doped ZnO nanoarray nanogenerator. *Sens. Actuators, B* **2015**, *213*, 382−389.

(66) Wang, B.; Thukral, A.; Xie, Z.; Liu, L.; Zhang, X.; Huang, W.; Yu, X.; Yu, C.; Marks, T. J.; Facchetti, A. Flexible and stretchable metal oxide nanofiber networks for multimodal and monolithically integrated wearable electronics. *Nat. Commun.* **2020**, *11*, 2405.

(67) Kim, J. H.; Seong, T. Y.; Chung, K. B.; Moon, C. S.; Noh, J. H.; Seok, H. J.; Kim, H. K. Transparent Sn-doped In2O3 electrodes with a nanoporous surface for enhancing the performance of perovskite solar cells. *J. Power Sources* **2019**, *418*, 152−161.

(68) Rodrigues, J.; Cerqueira, A. F. R.; Sousa, M. G.; Santos, N. F.; Pimentel, A.; Fortunato, E.; Da Cunha, A. F.; Monteiro, T.; Costa, F. M. Exploring the potential of laser assisted flow deposition grown ZnO for photovoltaic applications. *Mater. Chem. Phys.* **2016**, *177*, 322−329.

(69) Niemelä, J. P.; Macco, B.; Barraud, L.; Descoeudres, A.; Badel, N.; Despeisse, M.; Christmann, G.; Nicolay, S.; Ballif, C.; Kessels, W. M. M.; Creatore, M. Rear-emitter silicon heterojunction solar cells with atomic layer deposited ZnO:Al serving as an alternative transparent conducting oxide to In2O3:Sn. *Sol. Energy Mater. Sol. Cells* **2019**, *200*, 109953.

(70) Anandan, S.; Wen, X.; Yang, S. Room temperature growth of CuO nanorod arrays on copper and their application as a cathode in dye-sensitized solar cells. *Mater. Chem. Phys.* **2005**, *93*, 35−40.

(71) Son, S. Y.; Hong, S.-A.; Oh, S. Y.; Lee, Y.-C.; Lee, G.-W.; Kang, J. W.; Huh, Y. S.; Kim, I. T. Crab-Shell Biotemplated SnO 2 Composite Anodes for Lithium-Ion Batteries. *J. Nanosci. Nanotechnol.* **2018**, *18*, 6463−6468.

(72) Bijani, S.; Gabás, M.; Martínez, L.; Ramos-Barrado, J. R.; Morales, J.; Sánchez, L. Nanostructured Cu2O thin film electrodes

prepared by electrodeposition for rechargeable lithium batteries. *Thin Solid Films* **2007**, *515*, 5505−5511.

(73) Xu, Y. T.; Guo, Y.; Jiang, H.; Xie, X. B.; Zhao, B.; Zhu, P. L.; Fu, X. Z.; Sun, R.; Wong, C. P. Enhanced Performance of Lithium-Ion Batteries with Copper Oxide Microspheres @ Graphene Oxide Micro/Nanocomposite Electrodes. *Energy Technol.* **2015**, *3*, 488−495.

(74) Truong, P. L.; Kidanemariam, A.; Park, J. A critical innovation of photocatalytic degradation for toxic chemicals and pathogens in air. *J. Ind. Eng. Chem.* **2021**, *100*, 19−39.

(75) Liu, Y.; Jiao, Y.; Zhang, Z.; Qu, F.; Umar, A.; Wu, X. Hierarchical SnO2 nanostructures made of intermingled ultrathin nanosheets for environmental remediation, smart gas sensor, and supercapacitor applications. *ACS Appl. Mater. Interfaces* **2014**, *6*, 2174−2184.

(76) Guo, M. Y.; Fung, M. K.; Fang, F.; Chen, X. Y.; Ng, A. M. C.; Djurišić, A. B.; Chan, W. K. ZnO and TiO2 1D nanostructures for photocatalytic applications. *J. Alloys Compd.* **2011**, *509*, 1328−1332.

(77) Figueiredo, V.; Pinto, J. V.; Deuermeier, J.; Barros, R.; Alves, E.; Martins, R.; Fortunato, E. P-Type CuxO thin-film transistors produced by thermal oxidation. *J. Disp. Technol.* **2013**, *9*, 735−740.

(78) Fortunato, E.; Barros, R.; Barquinha, P.; Figueiredo, V.; Park, S. H. K.; Hwang, C. S.; Martins, R. Transparent p-type SnOx thin film transistors produced by reactive rf magnetron sputtering followed by low temperature annealing. *Appl. Phys. Lett.* **2010**, *97*, 052105.

(79) Fortunato, E. M. C.; Barquinha, P. M. C.; Pimentel, A. C. M. B. G.; Gonçalves, A. M. F.; Marques, A. J. S.; Pereira, L. M. N.; Martins, R. F. P. Fully transparent ZnO thin-film transistor produced at room temperature. *Adv. Mater.* **2005**, *17*, 590−594.

(80) Oh, B. Y.; Kim, Y. H.; Lee, H. J.; Kim, B. Y.; Park, H. G.; Han, J. W.; Heo, G. S.; Kim, T. W.; Kim, K. Y.; Seo, D. S. High-performance ZnO thin-film transistor fabricated by atomic layer deposition. *Semicond. Sci. Technol.* **2011**, *26*, 085007.

(81) Zhang, Q.; Zhang, K.; Xu, D.; Yang, G.; Huang, H.; Nie, F.; Liu, C.; Yang, S. CuO nanostructures: Synthesis, characterization, growth mechanisms, fundamental properties, and applications. *Prog. Mater. Sci.* **2014**, *60*, 208−337.

(82) Kriebel, C.; Banazadeh, M.; Freitag, B.; Winkel, G.; Knauf, N.; Braden, M.; Roden, B. Single crystal growth and characterization of superconducting PbSr(Y,Ca)CuO. *Phys. C* **1994**, *235−240*, 565−566.

(83) Döring, G.; Sternemann, C.; Kaprolat, A.; Mattila, A.; Hämäläinen, K.; Schülke, W. Shake-up valence excitations in CuO by resonant inelastic x-ray scattering. *Phys. Rev. B: Condens. Matter Mater. Phys.* **2004**, *70*, 085115.

(84) Kim, Y. S.; Hwang, I. S.; Kim, S. J.; Lee, C. Y.; Lee, J. H. CuO nanowire gas sensors for air quality control in automotive cabin. *Sens. Actuators, B* **2008**, *135*, 298−303.

(85) Wan, X.; Wang, J.; Zhu, L.; Tang, J. Gas sensing properties of Cu2O and its particle size and morphology-dependent gas-detection sensitivity. *J. Mater. Chem. A* **2014**, *2*, 13641−13647.

(86) Aslani, A.; Oroojpour, V. CO gas sensing of CuO nanostructures, synthesized by an assisted solvothermal wet chemical route. *Phys. B* **2011**, *406*, 144−149.

(87) Steinhauer, S.; Brunet, E.; Maier, T.; Mutinati, G. C.; Köck, A.; Freudenberg, O.; Gspan, C.; Grogger, W.; Neuhold, A.; Resel, R. Gas sensing properties of novel CuO nanowire devices. *Sens. Actuators, B* **2013**, *187*, 50−57.

(88) Batzill, M. Surface science studies of gas sensing materials: SnO2. *Sensors* **2006**, *6*, 1345−1366.

(89) Bolzan, A. A.; Fong, C.; Kennedy, B. J.; Howard, C. J. Structural Studies of Rutile-Type Metal Dioxides. *Acta Crystallogr., Sect. B: Struct. Sci.* **1997**, *53*, 373−380.

(90) Zhang, D.; Chang, H.; Liu, R. Humidity-Sensing Properties of One-Step Hydrothermally Synthesized Tin Dioxide-Decorated Graphene Nanocomposite on Polyimide Substrate. *J. Electron. Mater.* **2016**, *45* (8), 4275−4281.

(91) Sharma, A.; Arya, S. Economical and Efficient Electrochemical Sensing of Folic Acid using a Platinum Electrode Modified with Hydrothermally Synthesized Pd and Ag Co-Doped SnO2 Nanoparticles. *J. Electrochem. Soc.* **2019**, *166* (13), B1107−B1115.

(92) Nurzulaikha, R.; Lim, H. N.; Harrison, I.; Lim, S. S.; Pandikumar, A.; Huang, N. M.; Lim, S. P.; Thien, G. S. H.; Yusoff, N.; Ibrahim, I. Graphene/SnO2 nanocomposite-modified electrode for electrochemical detection of dopamine. *Sens. Bio-Sens. Res.* **2015**, *5*, 42−49.

(93) Wang, S.; Yang, J.; Zhang, H.; Wang, Y.; Gao, X.; Wang, L.; Zhu, Z. One-pot synthesis of 3D hierarchical SnO2 nanostructures and their application for gas sensor. *Sens. Actuators, B* **2015**, *207*, 83−89.

(94) Khan, S.; Briand, D. All-printed low-power metal oxide gas sensors on polymeric substrates. *Flex. Print. Electron.* **2019**, *4*, 015002.

(95) Liu, A.; Lv, S.; Zhao, L.; Liu, F.; Wang, J.; You, R.; Yang, Z.; He, J.; Jiang, L.; Wang, C.; Yan, X.; Sun, P.; Lu, G. Room temperature flexible NH3 sensor based on polyaniline coated Rh-doped SnO2 hollow nanotubes. *Sens. Actuators, B* **2021**, *330*, 129313.

(96) Li, R.; Jiang, K.; Chen, S.; Lou, Z.; Huang, T.; Chen, D.; Shen, G. SnO2/SnS2 nanotubes for flexible room-temperature NH3 gas sensors. *RSC Adv.* **2017**, *7*, 52503−52509.

(97) Meng, G.; Zhuge, F.; Nagashima, K.; Nakao, A.; Kanai, M.; He, Y.; Boudot, M.; Takahashi, T.; Uchida, K.; Yanagida, T. Nanoscale Thermal Management of Single SnO2 Nanowire: Pico-Joule Energy Consumed Molecule Sensor. *ACS Sens.* **2016**, *1*, 997−1002.

(98) Sharma, A.; Khosla, A.; Arya, S. Synthesis of SnO2 nanowires as a reusable and flexible electrode for electrochemical detection of riboflavin. *Microchem. J.* **2020**, *156*, 104858.

(99) Punetha, D.; Kar, M.; Pandey, S. K. A new type low-cost, flexible and wearable tertiary nanocomposite sensor for room temperature hydrogen gas sensing. *Sci. Rep.* **2020**, *10*, 2151.

(100) Preoteasa, E. A.; Georgescu, R.; Ciortea, C.; Fluerasu, D.; Harangus, L.; Iordan, A.; Severcan, F.; Boyar, H.; Preoteasa, E.; Piticu, I.; Pantelica, D.; Gheordunescu, V. I. Standardless PIXE analysis of thick biomineral structures. *Anal. Bioanal. Chem.* **2004**, *379*, 825−841.

(101) Özgür, Ü.; Alivov, Y. I.; Liu, C.; Teke, A.; Reshchikov, M. A.; Doğan, S.; Avrutin, V.; Cho, S. J.; Morkọ, H. A comprehensive review of ZnO materials and devices. *J. Appl. Phys.* **2005**, *98*, 041301.

(102) Chang, J.; Waclawik, E. R. Facet-controlled self-assembly of ZnO nanocrystals by non-hydrolytic aminolysis and their photo-degradation activities. *CrystEngComm* **2012**, *14*, 4041−4048.

(103) Park, T.; Lee, K. E.; Kim, N.; Oh, Y.; Yoo, J. K.; Um, M. K. Aspect ratio-controlled ZnO nanorods for highly sensitive wireless ultraviolet sensor applications. *J. Mater. Chem. C* **2017**, *5*, 12256−12263.

(104) Kwon, D. K.; Porte, Y.; Ko, K. Y.; Kim, H.; Myoung, J. M. High-Performance Flexible ZnO Nanorod UV/Gas Dual Sensors Using Ag Nanoparticle Templates. *ACS Appl. Mater. Interfaces* **2018**, *10*, 31505−31514.

(105) Subbiah, D. K.; Mani, G. K.; Babu, K. J.; Das, A.; Balaguru Rayappan, J. B. Nanostructured ZnO on cotton fabrics − A novel flexible gas sensor & UV filter. *J. Cleaner Prod.* **2018**, *194*, 372−382.

(106) Xu, Q.; Cheng, L.; Meng, L.; Wang, Z.; Bai, S.; Tian, X.; Jia, X.; Qin, Y. Flexible Self-Powered ZnO Film UV Sensor with a High Response. *ACS Appl. Mater. Interfaces* **2019**, *11*, 26127−26133.

(107) Ong, W. L.; Zhang, C.; Ho, G. W. Ammonia plasma modification towards a rapid and low temperature approach for tuning electrical conductivity of ZnO nanowires on flexible substrates. *Nanoscale* **2011**, *3*, 4206−4214.

(108) Hwang, S. H.; Kim, Y. K.; Jeong, S. M.; Choi, C.; Son, K. Y.; Lee, S. K.; Lim, S. K. Wearable colorimetric sensing fiber based on polyacrylonitrile with PdO@ZnO hybrids for the application of detecting H2 leakage. *Text. Res. J.* **2020**, *90*, 2198−2211.

(109) Kumar, R.; Rahman, H.; Ranwa, S.; Kumar, A.; Kumar, G. Development of cost effective metal oxide semiconductor based gas sensor over flexible chitosan/PVP blended polymeric substrate. *Carbohydr. Polym.* **2020**, *239*, 116213.

(110) Yang, D.; Cho, I.; Kim, D.; Lim, M. A.; Li, Z.; Ok, J. G.; Lee, M.; Park, I. Gas Sensor by Direct Growth and Functionalization of Metal Oxide/Metal Sulfide Core-Shell Nanowires on Flexible Substrates. *ACS Appl. Mater. Interfaces* **2019**, *11*, 24298−24307.

(111) Bhat, P.; Pradhan, U. U.; Naveen Kumar, S. K. Synthesis and characterization of ZnO nano discs using wet chemical method for sensing applications. *Mater. Today: Proc.* **2018**, *5*, 10763−10770.

(112) Shan, F. K.; Liu, G. X.; Shin, B. C.; Lee, W. J. Annealing effects of ZnO thin films deposited on Si(100) by using pulsed laser deposition. *J. Korean Phys. Soc.* **2009**, *54*, 916−920.

(113) Eranna, G. *Metal Oxide Nanostructures as Gas Sensing Devices*; CRC Press: 2012; p 1−336.

(114) Jun, L.; Chen, Q.; Fu, W.; Yang, Y.; Zhu, W.; Zhang, J. Electrospun Yb-Doped In(2)O(3) Nanofiber Field-Effect Transistors for Highly Sensitive Ethanol Sensors. *ACS Appl. Mater. Interfaces* **2020**, *12* (34), 38425−38434.

(115) Wan, K.; Wang, D.; Wang, F.; Li, H.; Xu, J.; Wang, X.; Yang, J. Hierarchical In2O3@SnO2 Core−Shell Nanofiber for High Efficiency Formaldehyde Detection. *ACS Appl. Mater. Interfaces* **2019**, *11* (48), 45214−45225.

(116) Liu, Q.; Liu, Y.; Wu, F.; Cao, X.; Li, Z.; Alharbi, M.; Abbas, A. N.; Amer, M. R.; Zhou, C. Highly Sensitive and Wearable In2O3 Nanoribbon Transistor Biosensors with Integrated On-Chip Gate for Glucose Monitoring in Body Fluids. *ACS Nano* **2018**, *12* (2), 1170−1178.

(117) Liu, Q.; Zhao, C.; Chen, M.; Liu, Y.; Zhao, Z.; Wu, F.; Li, Z.; Weiss, P. S.; Andrews, A. M.; Zhou, C. Flexible Multiplexed In(2)O(3) Nanoribbon Aptamer-Field-Effect Transistors for Biosensing. *iScience* **2020**, *23* (9), 101469.

(118) Lv, Y.-K.; Li, Y.-Y.; Zhou, R.-H.; Pan, Y.-P.; Yao, H.-C.; Li, Z.-J. N-Doped Graphene Quantum Dot-Decorated Three-Dimensional Ordered Macroporous In2O3 for NO2 Sensing at Low Temperatures. *ACS Appl. Mater. Interfaces* **2020**, *12* (30), 34245−34253.

(119) Pokhrel, S.; Birkenstock, J.; Dianat, A.; Zimmermann, J.; Schowalter, M.; Rosenauer, A.; Ciacchi, L. C.; Mädler, L. In situ high temperature X-ray diffraction, transmission electron microscopy and theoretical modeling for the formation of WO3 crystallites. *CrystEngComm* **2015**, *17*, 6985−6998.

(120) Pi, M.; Zheng, L.; Luo, H.; Duan, S.; Li, C.; Yang, J.; Zhang, D.; Chen, S. Improved acetone gas sensing performance based on optimization of a transition metal doped WO3 system at room temperature. *J. Phys. D: Appl. Phys.* **2021**, *54* (15), 155107.

(121) Jamali, M.; Shariatmadar Tehrani, F. Effect of synthesis route on the structural and morphological properties of WO3 nanostructures. *Mater. Sci. Semicond. Process.* **2020**, *107*, 104829.

(122) Behera, B.; Chandra, S. Synthesis of WO3 nanorods by thermal oxidation technique for NO2 gas sensing application. *Mater. Sci. Semicond. Process.* **2018**, *86*, 79−84.

(123) Singh, S.; Majumder, S. B. Synthesis, characterization and liquefied petroleum gas (LPG) sensing properties of WO3 nano-particles. *AIP Conf. Proc.* **2017**, *1953* (1), 090042.

(124) Veeralingam, S.; Badhulika, S. Strain engineered biocompat-ible h-WO3 nanofibers based highly selective and sensitive chemiresistive platform for detection of Catechol in blood sample. *Mater. Sci. Eng., C* **2020**, *108*, 110365.

(125) Kukkola, J.; Mäklin, J.; Halonen, N.; Kyllönen, T.; Tóth, G.; Szabó, M.; Shchukarev, A.; Mikkola, J.-P.; Jantunen, H.; Kordás, K. Gas sensors based on anodic tungsten oxide. *Sens. Actuators, B* **2011**, *153* (2), 293−300.

(126) Zhang, H.; Wang, Y.; Zhu, X.; Li, Y.; Cai, W. Bilayer Au nanoparticle-decorated WO3 porous thin films: On-chip fabrication and enhanced NO2 gas sensing performances with high selectivity. *Sens. Actuators, B* **2019**, *280*, 192−200.

(127) Moon, D. B.; Bag, A.; Lee, H. B.; Meeseepong, M.; Lee, D. H.; Lee, N. E. A stretchable, room-temperature operable, chemiresistive gas sensor using nanohybrids of reduced graphene oxide and zinc oxide nanorods. *Sens. Actuators, B* **2021**, *345*, 130373.

(128) Nakarungsee, P.; Srirattanapibul, S.; Issro, C.; Tang, I. M.; Thongmee, S. High performance Cr doped ZnO by UV for NH3 gas sensor. *Sens. Actuators, A* **2020**, *314*, 112230.

(129) Park, S. J.; Jeon, J. Y.; Kang, B. C.; Ha, T. J. Wearable temperature sensors based on lanthanum-doped aluminum-oxide

dielectrics operating at low-voltage and high-frequency for healthcare monitoring systems. *Ceram. Int.* **2021**, *47*, 4579−4586.

(130) Yang, A.; Li, W.; Chu, J.; Wang, D.; Yuan, H.; Zhu, J.; Wang, X.; Rong, M. Enhanced sensing of sulfur hexafluoride decomposition components based on noble-metal-functionalized cerium oxide. *Mater. Des.* **2020**, *187*, 108391.

(131) Wang, S.; Jiang, Y.; Tai, H.; Liu, B.; Duan, Z.; Yuan, Z.; Pan, H.; Xie, G.; Du, X.; Su, Y. An integrated flexible self-powered wearable respiration sensor. *Nano Energy* **2019**, *63*, 103829.

(132) Pi, M.; Zheng, L.; Luo, H.; Duan, S.; Li, C.; Yang, J.; Zhang, D.; Chen, S. Improved acetone gas sensing performance based on optimization of a transition metal doped WO$_3$ system at room temperature. *J. Phys. D: Appl. Phys.* **2021**, *54*, 155107.

(133) You, R.; Han, D. D.; Liu, F.; Zhang, Y. L.; Lu, G. Fabrication of flexible room-temperature NO2 sensors by direct laser writing of In2O3 and graphene oxide composites. *Sens. Actuators, B* **2018**, *277*, 114−120.

(134) Rashid, T. R.; Phan, D. T.; Chung, G. S. A flexible hydrogen sensor based on Pd nanoparticles decorated ZnO nanorods grown on polyimide tape. *Sens. Actuators, B* **2013**, *185*, 777−784.

(135) Tesfamichael, T.; Arita, M.; Bostrom, T.; Bell, J. Thin film deposition and characterization of pure and iron-doped electron-beam evaporated tungsten oxide for gas sensors. *Thin Solid Films* **2010**, *518*, 4791−4797.

(136) Korotcenkov, G.; Cho, B. K. Metal oxide composites in conductometric gas sensors: Achievements and challenges. *Sens. Actuators, B* **2017**, *244*, 182−210.

(137) Chong, X.; Kim, K. J.; Li, E.; Zhang, Y.; Ohodnicki, P. R.; Chang, C. H.; Wang, A. X. Near-infrared absorption gas sensing with metal-organic framework on optical fibers. *Sens. Actuators, B* **2016**, *232*, 43−51.

(138) Zhang, K. Y.; Yu, Q.; Wei, H.; Liu, S.; Zhao, Q.; Huang, W. Long-Lived Emissive Probes for Time-Resolved Photoluminescence Bioimaging and Biosensing. *Chem. Rev.* **2018**, *118*, 1770−1839.

(139) Shen, S.; Wang, X.; Chen, T.; Feng, Z.; Li, C. Transfer of photoinduced electrons in anatase-rutile TiO2 determined by time-resolved mid-infrared spectroscopy. *J. Phys. Chem. C* **2014**, *118*, 12661−12668.

(140) Koh, H. J.; Kim, S. J.; Maleski, K.; Cho, S. Y.; Kim, Y. J.; Ahn, C. W.; Gogotsi, Y.; Jung, H. T. Enhanced Selectivity of MXene Gas Sensors through Metal Ion Intercalation: In Situ X-ray Diffraction Study. *ACS Sens.* **2019**, *4*, 1365−1372.

(141) Jiang, Y.; Xia, T.; Shen, L.; Ma, J.; Ma, H.; Sun, T.; Lv, F.; Zhu, N. Facet-Dependent Cu2O Electrocatalysis for Wearable Enzyme-Free Smart Sensing. *ACS Catal.* **2021**, *11*, 2949−2955.

(142) Raghu, A. V.; Karuppanan, K. K.; Nampoothiri, J.; Pullithadathil, B. Wearable, Flexible Ethanol Gas Sensor Based on TiO2 Nanoparticles-Grafted 2D-Titanium Carbide Nanosheets. *ACS Appl. Nano Mater.* **2019**, *2*, 1152−1163.

(143) Liang, Y. C.; Chang, C. W. Improvement of ethanol gas-sensing responses of ZnO−WO3 composite nanorods through annealing induced local phase transformation. *Nanomaterials* **2019**, *9*, 669.

(144) Patsha, A.; Sahoo, P.; Amirthapandian, S.; Prasad, A. K.; Das, A.; Tyagi, A. K.; Cotta, M. A.; Dhara, S. Localized Charge Transfer Process and Surface Band Bending in Methane Sensing by GaN Nanowires. *J. Phys. Chem. C* **2015**, *119*, 21251−21260.

(145) Hart, J. L.; Lang, A. C.; Leff, A. C.; Longo, P.; Trevor, C.; Twesten, R. D.; Taheri, M. L. Direct Detection Electron Energy-Loss Spectroscopy: A Method to Push the Limits of Resolution and Sensitivity. *Sci. Rep.* **2017**, *7*, 8243.

(146) Jian, N.; Xue, P.; Diao, D. Thermally induced atomic and electronic structure evolution in nanostructured carbon film by in situ TEM/EELS analysis. *Appl. Surf. Sci.* **2019**, *498*, 143831.

(147) Mizsei, J.; Lantto, V. In situ STM and AFM characterization of Pd nanoparticle activated SnO 2 sensor surface. *Proc. IEEE Sens.* **2004**, *2*, 673−676.

(148) Pettinger, B.; Picardi, G.; Schuster, R.; Ertl, G. Surface-enhanced and STM-tip-enhanced Raman spectroscopy at metal surfaces. *Single Mol.* **2002**, *3*, 285−294.

(149) Zheng, Z. Q.; Yao, J. D.; Wang, B.; Yang, G. W. Light-controlling, flexible and transparent ethanol gas sensor based on ZnO nanoparticles for wearable devices. *Sci. Rep.* **2015**, *5*, 11070.

(150) Lim, Z. H.; Chia, Z. X.; Kevin, M.; Wong, A. S. W.; Ho, G. W. A facile approach towards ZnO nanorods conductive textile for room temperature multifunctional sensors. *Sens. Actuators, B* **2010**, *151* (1), 121−126.

(151) Seetha, M.; Meena, P.; Mangalaraj, D.; Masuda, Y.; Senthil, K. Synthesis of indium oxide cubic crystals by modified hydrothermal route for application in room temperature flexible ethanol sensors. *Mater. Chem. Phys.* **2012**, *133* (1), 47−54.

(152) Wang, X.-X.; Li, H.-Y.; Guo, X. Flexible and transparent sensors for ultra-low NO2 detection at room temperature under visible light illumination. *J. Mater. Chem. A* **2020**, *8* (29), 14482−14490.

(153) Zeng, H.; Takahashi, T.; Kanai, M.; Zhang, G.; He, Y.; Nagashima, K.; Yanagida, T. Long-Term Stability of Oxide Nanowire Sensors via Heavily Doped Oxide Contact. *ACS Sens.* **2017**, *2* (12), 1854−1859.

(154) Dubourg, G.; Radovic, M. Multifunctional Screen-Printed TiO2 Nanoparticles Tuned by Laser Irradiation for a Flexible and Scalable UV Detector and Room-Temperature Ethanol Sensor. *ACS Appl. Mater. Interfaces* **2019**, *11* (6), 6257−6266.

(155) Khasim, S.; Pasha, A.; Hatem Al, A.; Badi, N.; Imran, M.; Al-Ghamdi, S. A. Development of high-performance flexible and stretchable sensor based on secondary doped PEDOT−PSS:TiO2 nanocomposite for room-temperature detection of nitric oxide. *J. Mater. Sci.: Mater. Electron.* **2021**, *32* (6), 7491−7508.

(156) Jović, M.; Hidalgo-Acosta, J. C.; Lesch, A.; Costa Bassetto, V.; Smirnov, E.; Cortés-Salazar, F.; Girault, H. H. Large-scale layer-by-layer inkjet printing of flexible iridium-oxide based pH sensors. *J. Electroanal. Chem.* **2018**, *819*, 384−390.

(157) Santos, L.; Neto, J. P.; Crespo, A.; Nunes, D.; Costa, N.; Fonseca, I. M.; Barquinha, P.; Pereira, L.; Silva, J.; Martins, R.; Fortunato, E. WO3 nanoparticle-based conformable pH sensor. *ACS Appl. Mater. Interfaces* **2014**, *6* (15), 12226−34.

(158) Zhou, L.; Cheng, C.; Li, X.; Ding, J.; Liu, Q.; Su, B. Nanochannel Templated Iridium Oxide Nanostructures for Wide-Range pH Sensing from Solutions to Human Skin Surface. *Anal. Chem.* **2020**, *92* (5), 3844−3851.

(159) Palit, S.; Singh, K.; Lou, B.-S.; Her, J.-L.; Pang, S.-T.; Pan, T.-M. Ultrasensitive dopamine detection of indium-zinc oxide on PET flexible based extended-gate field-effect transistor. *Sens. Actuators, B* **2020**, *310*, 127850.

(160) Huang, W.-D.; Cao, H.; Deb, S.; Chiao, M.; Chiao, J. C. A flexible pH sensor based on the iridium oxide sensing film. *Sens. Actuators, A* **2011**, *169* (1), 1−11.

(161) Nguyen, C. M.; Huang, W.-D.; Rao, S.; Cao, H.; Tata, U.; Chiao, M.; Chiao, J.-C. Sol-Gel Iridium Oxide-Based pH Sensor Array on Flexible Polyimide Substrate. *IEEE Sens. J.* **2013**, *13* (10), 3857−3864.

(162) Lue, C.-E.; Wang, I. S.; Huang, C.-H.; Shiao, Y.-T.; Wang, H.-C.; Yang, C.-M.; Hsu, S.-H.; Chang, C.-Y.; Wang, W.; Lai, C.-S. pH sensing reliability of flexible ITO/PET electrodes on EGFETs prepared by a roll-to-roll process. *Microelectron. Reliab.* **2012**, *52* (8), 1651−1654.

(163) Maiolo, L.; Mirabella, S.; Maita, F.; Alberti, A.; Minotti, A.; Strano, V.; Pecora, A.; Shacham-Diamand, Y.; Fortunato, G. Flexible pH sensors based on polysilicon thin film transistors and ZnO nanowalls. *Appl. Phys. Lett.* **2014**, *105* (9), 093501.

(164) Nien, Y.-H.; Su, T.-Y.; Ho, C.-S.; Chou, J.-C.; Lai, C.-H.; Kuo, P.-Y.; Kang, Z.-X.; Dong, Z.-X.; Lai, T.-Y.; Wang, C.-H. The Analysis of Potentiometric Flexible Arrayed Urea Biosensor Modified by Graphene Oxide and γ-Fe2O3 Nanoparticles. *IEEE Trans. Electron Devices* **2020**, *67* (11), 5104−5110.

(165) Sedighi, A.; Montazer, M.; Mazinani, S. Synthesis of wearable and flexible NiP0.1-SnOx/PANI/CuO/cotton towards a non-enzymatic glucose sensor. *Biosens. Bioelectron.* **2019**, *135*, 192−199.

(166) K.P.O., M.; Shown, I.; Chen, L.-C.; Chen, K.-H.; Tai, Y. Flexible sensor for dopamine detection fabricated by the direct growth of α-Fe2O3 nanoparticles on carbon cloth. *Appl. Surf. Sci.* **2018**, *427*, 387−395.

(167) Abdelbasir, S. M.; El-Sheikh, S. M.; Morgan, V. L.; Schmidt, H.; Casso-Hartmann, L. M.; Vanegas, D. C.; Velez-Torres, I.; McLamore, E. S. Graphene-Anchored Cuprous Oxide Nanoparticles from Waste Electric Cables for Electrochemical Sensing. *ACS Sustainable Chem. Eng.* **2018**, *6* (9), 12176−12186.

(168) Madhu, S.; Anthuuvan, A. J.; Ramasamy, S.; Manickam, P.; Bhansali, S.; Nagamony, P.; Chinnuswamy, V. ZnO Nanorod Integrated Flexible Carbon Fibers for Sweat Cortisol Detection. *ACS Appl. Electron. Mater.* **2020**, *2* (2), 499−509.

(169) Leonardi, S. G.; Aloisio, D.; Donato, N.; Russo, P. A.; Ferro, M. C.; Pinna, N.; Neri, G. Amperometric Sensing of H2O2using Pt-TiO2/Reduced Graphene Oxide Nanocomposites. *ChemElectroChem* **2014**, *1* (3), 617−624.

(170) Xiao, F.; Li, Y.; Zan, X.; Liao, K.; Xu, R.; Duan, H. Growth of Metal-Metal Oxide Nanostructures on Freestanding Graphene Paper for Flexible Biosensors. *Adv. Funct. Mater.* **2012**, *22* (12), 2487−2494.

(171) Wu, J.; Yin, C.; Zhou, J.; Li, H.; Liu, Y.; Shen, Y.; Garner, S.; Fu, Y.; Duan, H. Ultrathin Glass-Based Flexible, Transparent, and Ultrasensitive Surface Acoustic Wave Humidity Sensor with ZnO Nanowires and Graphene Quantum Dots. *ACS Appl. Mater. Interfaces* **2020**, *12*, 39817−39825.

(172) Gong, L.; Wang, X.; Zhang, D.; Ma, X.; Yu, S. Flexible wearable humidity sensor based on cerium oxide/graphitic carbon nitride nanocomposite self-powered by motion-driven alternator and its application for human physiological detection. *J. Mater. Chem. A* **2021**, *9*, 5619−5629.

(173) Zhu, D.; Fu, Y.; Zang, W.; Zhao, Y.; Xing, L.; Xue, X. Piezo/active humidity sensing of CeO2/ZnO and SnO2/ZnO nanoarray nanogenerators with high response and large detecting range. *Sens. Actuators, B* **2014**, *205*, 12−19.

(174) Hashim, A.; Al-Khafaji, Y.; Hadi, A. Synthesis and Characterization of Flexible Resistive Humidity Sensors Based on PVA/PEO/CuO Nanocomposites. *Trans. Electr. Electron. Mater.* **2019**, *20* (6), 530−536.

(175) Bai, S.; Wu, W.; Qin, Y.; Cui, N.; Bayerl, D. J.; Wang, X. High-performance integrated ZnO nanowire UV sensors on rigid and flexible substrates. *Adv. Funct. Mater.* **2011**, *21*, 4464−4469.

(176) Hsu, C. L.; Li, H. H.; Hsueh, T. J. Water- and humidity-enhanced UV detector by using p-type La-doped ZnO nanowires on flexible polyimide substrate. *ACS Appl. Mater. Interfaces* **2013**, *5*, 11142−11151.

(177) Rackauskas, S.; Mustonen, K.; Järvinen, T.; Mattila, M.; Klimova, O.; Jiang, H.; Tolochko, O.; Lipsanen, H.; Kauppinen, E. I.; Nasibulin, A. G. Synthesis of ZnO tetrapods for flexible and transparent UV sensors. *Nanotechnology* **2012**, *23*, 095502.

(178) Figueira, J.; Gaspar, C.; Carvalho, J. T.; Loureiro, J.; Fortunato, E.; Martins, R.; Pereira, L. Sustainable fully printed UV sensors on cork using zinc oxide/ethylcellulose inks. *Micromachines* **2019**, *10*, 601.

(179) Liu, J.; Wu, W.; Bai, S.; Qin, Y. Synthesis of high crystallinity ZnO nanowire array on polymer substrate and flexible fiber-based sensor. *ACS Appl. Mater. Interfaces* **2011**, *3* (11), 4197−200.

(180) Liu, X.; Du, H.; Wang, P.; Lim, T.-T.; Sun, X. W. A high-performance UV/visible photodetector of Cu2O/ZnO hybrid nano-films on SWNT-based flexible conducting substrates. *J. Mater. Chem. C* **2014**, *2* (44), 9536−9542.

(181) Zheng, Q.; Huang, J.; Cao, S.; Gao, H. A flexible ultraviolet photodetector based on single crystalline MoO3 nanosheets. *J. Mater. Chem. C* **2015**, *3* (28), 7469−7475.

(182) Wang, Z.; Zhan, X.; Wang, Y.; Muhammad, S.; Huang, Y.; He, J. A flexible UV nanosensor based on reduced graphene oxide decorated ZnO nanostructures. *Nanoscale* **2012**, *4* (8), 2678−84.

(183) Li, L.; Gu, L.; Lou, Z.; Fan, Z.; Shen, G. ZnO Quantum Dot Decorated Zn2SnO4 Nanowire Heterojunction Photodetectors with Drastic Performance Enhancement and Flexible Ultraviolet Image Sensors. *ACS Nano* **2017**, *11* (4), 4067−4076.

(184) Huang, C. C.; Kao, Z. K.; Liao, Y. C. Flexible miniaturized nickel oxide thermistor arrays via inkjet printing technology. *ACS Appl. Mater. Interfaces* **2013**, *5* (24), 12954−9.

(185) Shin, J.; Jeong, B.; Kim, J.; Nam, V. B.; Yoon, Y.; Jung, J.; Hong, S.; Lee, H.; Eom, H.; Yeo, J.; Choi, J.; Lee, D.; Ko, S. H. Sensitive Wearable Temperature Sensor with Seamless Monolithic Integration. *Adv. Mater.* **2020**, *32* (2), 1905527.

(186) Nakajima, T.; Tsuchiya, T. Flexible thermistors: pulsed laser-induced liquid-phase sintering of spinel Mn−Co−Ni oxide films on polyethylene terephthalate sheets. *J. Mater. Chem. C* **2015**, *3* (15), 3809−3816.

(187) Nakajima, T.; Hanawa, S.; Tsuchiya, T. Highly stable flexible thermistor properties of spinel Mn-Co-Ni oxide films on silver/carbon micro-pinecone array composite electrodes. *J. Appl. Phys.* **2017**, *122* (13), 135309.

(188) Lee, T.; Lee, W.; Kim, S.-W.; Kim, J. J.; Kim, B.-S. Flexible Textile Strain Wireless Sensor Functionalized with Hybrid Carbon Nanomaterials Supported ZnO Nanowires with Controlled Aspect Ratio. *Adv. Funct. Mater.* **2016**, *26* (34), 6206−6214.

(189) Sun, S.; Guo, L.; Chang, X.; Liu, Y.; Niu, S.; Lei, Y.; Liu, T.; Hu, X. A wearable strain sensor based on the ZnO/graphene nanoplatelets nanocomposite with large linear working range. *J. Mater. Sci.* **2019**, *54* (9), 7048−7061.

(190) Panth, M.; Cook, B.; Alamri, M.; Ewing, D.; Wilson, A.; Wu, J. Z. Flexible Zinc Oxide Nanowire Array/Graphene Nanohybrid for High-Sensitivity Strain Detection. *ACS Omega* **2020**, *5* (42), 27359−27367.

(191) Dutta, B.; Kar, E.; Bose, N.; Mukherjee, S. NiO@SiO2/PVDF: A Flexible Polymer Nanocomposite for a High Performance Human Body Motion-Based Energy Harvester and Tactile e-Skin Mechanosensor. *ACS Sustainable Chem. Eng.* **2018**, *6*, 10505−10516.

(192) Li, W.; Chen, R.; Qi, W.; Cai, L.; Sun, Y.; Sun, M.; Li, C.; Yang, X.; Xiang, L.; Xie, D.; Ren, T. Reduced Graphene Oxide/Mesoporous ZnO NSs Hybrid Fibers for Flexible, Stretchable, Twisted, and Wearable NO2 E-Textile Gas Sensor. *ACS Sens.* **2019**, *4* (10), 2809−2818.

(193) Sim, K.; Rao, Z.; Zou, Z.; Ershad, F.; Lei, J.; Thukral, A.; Chen, J.; Huang, Q.-A.; Xiao, J.; Yu, C. Metal oxide semiconductor nanomembrane-based soft unnoticeable multifunctional electronics for wearable human-machine interfaces. *Sci. Adv.* **2019**, *5* (8), eaav9653.

(194) Hu, P.; Han, N.; Zhang, D.; Ho, J. C.; Chen, Y. Highly formaldehyde-sensitive, transition-metal doped ZnO nanorods prepared by plasma-enhanced chemical vapor deposition. *Sens. Actuators, B* **2012**, *169*, 74−80.

(195) Namgung, G.; Ta, Q. T. H.; Yang, W.; Noh, J. S. Diffusion-Driven Al-Doping of ZnO Nanorods and Stretchable Gas Sensors Made of Doped ZnO Nanorods/Ag Nanowires Bilayers. *ACS Appl. Mater. Interfaces* **2019**, *11* (1), 1411−1419.

(196) Kumaresan, Y.; Lee, R.; Lim, N.; Pak, Y.; Kim, H.; Kim, W.; Jung, G.-Y. Extremely Flexible Indium-Gallium-Zinc Oxide (IGZO) Based Electronic Devices Placed on an Ultrathin Poly(Methyl Methacrylate) (PMMA) Substrate. *Adv. Electron. Mater.* **2018**, *4* (7), 1800167.

(197) Kang, J.-Y.; Koo, W.-T.; Jang, J.-S.; Kim, D.-H.; Jeong, Y. J.; Kim, R.; Ahn, J.; Choi, S.-J.; Kim, I.-D. 2D layer assembly of Pt-ZnO nanoparticles on reduced graphene oxide for flexible NO₂ sensors. *Sens. Actuators, B* **2021**, *331*, 129371.

(198) Liu, C.; Tai, H.; Zhang, P.; Yuan, Z.; Du, X.; Xie, G.; Jiang, Y. A high-performance flexible gas sensor based on self-assembled PANI-CeO2 nanocomposite thin film for trace-level NH3 detection at room temperature. *Sens. Actuators, B* **2018**, *261*, 587−597.

(199) Lin, Y.; Kan, K.; Song, W.; Zhang, G.; Dang, L.; Xie, Y.; Shen, P.; Li, L.; Shi, K. Controllable synthesis of Co3O4/polyethylenei-

mine-carbon nanotubes nanocomposites for CO and NH3 gas sensing at room temperature. *J. Alloys Compd.* **2015**, *639*, 187−196.

(200) Liu, A.; Wang, C.; Yang, X.; Liu, F.; Li, S.; Wang, J.; You, R.; Yang, Z.; He, J.; Jiang, L.; Yan, X.; Sun, P.; Lu, G. Polyaniline @ porous nanosphere SnO_2/Zn_2SnO_4 nanohybrid for selective room temperature flexible NH_3 sensor. *Sens. Actuators, B* **2020**, *317*, 128218.

(201) Wang, J.; Yang, P.; Wei, X. High-performance, room-temperature, and no-humidity-impact ammonia sensor based on heterogeneous nickel oxide and zinc oxide nanocrystals. *ACS Appl. Mater. Interfaces* **2015**, *7* (6), 3816−24.

(202) Zang, W.; Nie, Y.; Zhu, D.; Deng, P.; Xing, L.; Xue, X. Core−Shell In2O3/ZnO Nanoarray Nanogenerator as a Self-Powered Active Gas Sensor with High H2S Sensitivity and Selectivity at Room Temperature. *J. Phys. Chem. C* **2014**, *118* (17), 9209−9216.

(203) Yang, Z.; Jiang, L.; Wang, J.; Liu, F.; He, J.; Liu, A.; Lv, S.; You, R.; Yan, X.; Sun, P.; Wang, C.; Duan, Y.; Lu, G. Flexible resistive NO_2 gas sensor of three-dimensional crumpled MXene Ti_3C_2Tx/ZnO spheres for room temperature application. *Sens. Actuators, B* **2021**, *326*, 128828.

(204) Tanguy, N. R.; Thompson, M.; Yan, N. A review on advances in application of polyaniline for ammonia detection. *Sens. Actuators, B* **2018**, *257*, 1044−1064.

(205) Bai, S.; Tian, Y.; Cui, M.; Sun, J.; Tian, Y.; Luo, R.; Chen, A.; Li, D. Polyaniline@SnO2 heterojunction loading on flexible PET thin film for detection of NH3 at room temperature. *Sens. Actuators, B* **2016**, *226*, 540−547.

(206) Li, S.; Lin, P.; Zhao, L.; Wang, C.; Liu, D.; Liu, F.; Sun, P.; Liang, X.; Liu, F.; Yan, X.; Gao, Y.; Lu, G. The room temperature gas sensor based on Polyaniline@flower-like WO3 nanocomposites and flexible PET substrate for NH3 detection. *Sens. Actuators, B* **2018**, *259*, 505−513.

(207) Zhang, Y.; Zhang, J.; Jiang, Y.; Duan, Z.; Liu, B.; Zhao, Q.; Wang, S.; Yuan, Z.; Tai, H. Ultrasensitive flexible NH_3 gas sensor based on polyaniline/$SrGe_4O_9$ nanocomposite with ppt-level detection ability at room temperature. *Sens. Actuators, B* **2020**, *319*, 128293.

(208) Saravanakumar, B.; Soyoon, S.; Kim, S. J. Self-powered pH sensor based on a flexible organic-inorganic hybrid composite nanogenerator. *ACS Appl. Mater. Interfaces* **2014**, *6*, 13716−13723.

(209) Wang, B.; Facchetti, A. Mechanically Flexible Conductors for Stretchable and Wearable E-Skin and E-Textile Devices. *Adv. Mater.* **2019**, *31*, 1901408.

(210) Singh, E.; Meyyappan, M.; Nalwa, H. S. Flexible Graphene-Based Wearable Gas and Chemical Sensors. *ACS Appl. Mater. Interfaces* **2017**, *9*, 34544−34586.

(211) Yaqoob, U.; Phan, D.-T.; Uddin, A. S. M. I.; Chung, G.-S. Highly flexible room temperature NO2 sensor based on MWCNTs-WO3 nanoparticles hybrid on a PET substrate. *Sens. Actuators, B* **2015**, *221*, 760−768.

(212) Utari, L.; Septiani, N. L. W.; Suyatman; Nugraha; Nur, L. O.; Wasisto, H. S.; Yuliarto, B. Wearable Carbon Monoxide Sensors Based on Hybrid Graphene/ZnO Nanocomposites. *IEEE Access* **2020**, *8*, 49169−49179.

(213) Choi, S. J.; Choi, H. J.; Koo, W. T.; Huh, D.; Lee, H.; Kim, I. D. Metal-Organic Framework-Templated PdO-Co3O4 Nanocubes Functionalized by SWCNTs: Improved NO2 Reaction Kinetics on Flexible Heating Film. *ACS Appl. Mater. Interfaces* **2017**, *9* (46), 40593−40603.

(214) Rogers, J. A.; Someya, T.; Huang, Y. Materials and mechanics for stretchable electronics. *Science* **2010**, *327* (5973), 1603−1607.